

**HIGH-TEMPERATURE PHYSICO-MECHANICAL
PROPERTIES OF AS-RECEIVED STRUCTURES IN
DUAL-PHASE ADVANCED HIGH-STRENGTH STEELS**

by

MOHAMMADHOSSEIN GHONCHEH, B.Sc., M.Sc.

A Thesis Submitted to the School of Graduate Studies in
Partial Fulfillment of the Requirements for the Degree of

MASTER OF APPLIED SCIENCE

in

The Department of Materials Science and Engineering

McMaster University

September 2019

© Mohammadhossein Ghoncheh, 2019

The following individuals certify that they have read, and recommend to the College of Graduate Studies for acceptance, a thesis/dissertation entitled:

High-Temperature Physico-Mechanical Properties of As-Received Structures in Dual-Phase Advanced High-Strength Steels

submitted by Mohammadhossein Ghoncheh in partial fulfillment of the requirements of the degree of Master of Applied Science

Number of Pages: xvi, 95

Prof. André B. Phillion, Materials Science and Engineering, McMaster University

Supervisor

Prof. Neslihan Dogan, Materials Science and Engineering, McMaster University

Supervisory Committee Member

Prof. Nabil Bassim, Materials Science and Engineering, McMaster University

University Examiner

Abstract

Dual-phase (DP) advanced high-strength steels (AHSSs) are widely used in the automotive industry due to their excellent combination of strength, ductility, and work hardening properties. However, defects occurring during processing make these ferrous alloys expensive. Toward this ends, high-temperature tensile tests using a Gleeble thermomechanical simulator have been conducted to determine the stress/strain behaviour at temperatures between 1250 to 1480°C in order to quantify the tensile strength and ductility. The results of both as-cast and transfer-bar material will be presented as well as three different sample geometries in order to better understand the effects of starting microstructure, thermal gradient, and stress/strain distribution on the reproducibility of high temperature properties. Optical and scanning electron microscopy are then performed to further elucidate the structure/property relationships. The results show that the presence of preexisted porosities in the as-cast structure decreases the high-temperature strength of the material, while the transfer-bar samples show lower ductility at ultra-high temperatures, ($T \geq 1450^\circ\text{C}$), due to their severe susceptibility to melting. In terms of the two mentioned thermo-mechanical characteristics, voids nucleation, growth, and coalescence initiated with porosity clustering are the main mechanisms behind the lower strength of the as-cast samples, whilst tearing apart of the melt plays an important role to drastically drop the ductility of transfer-bars at mentioned temperature interval. Moreover, the long-gauge-length (LGL) geometry proposes better reproducibility of data compared with the other geometries. This is attributed to a suitable combination between low stress localization and high thermal gradient during the Gleeble testing that provides a condition in which the samples experience sharp localized necking right on the hot-spot zone. The obtained data can be used as part of multi-physics process and microstructure continuous casting models.

Acknowledgements

I would like to begin by appreciating the person most directly involved in this project: my supervisor, Prof. André B. Phillion and industrial advisor, Dr. Joydeep Sengupta who kindly supported me during my master's program. I am particularly thankful for all opportunities which allowed me to nurture my experience in experimental processes at McMaster University and ArcelorMittal-Dofasco (AM-D). Also, I would like to acknowledge the R&D manager in AM-D, Mr. Bruce Farrand and everyone there who helped me toward this research. I appreciate the committee members, Prof. Sumanth Shankar and Prof. Neslihan Dogan, as well as Prof. Nabil Bassim who kindly spent their time and meticulously put their useful comments on the current study.

Special thanks to my colleagues in our friendly and competitive research group (SIM3P), Morteza Narvan, Shahryar Asqardoust, Prof. Saeed G. Shabestari, Dr. Hamid Azizi, Dr. Mohsen Mohammadi, and Dr. Zahra Khatami who encouraged me to passionately follow my career. Also, many thanks to my friends who kindly shared their happy moments and leisure time with me during last two years.

Finally, my caring beloved parents for all unforgettable supports, kindness, inspiration, and encouragement in my life.

Preface

With the exception of my supervisory committee members, who provided detailed suggestions on this research, I am the primary contributor of this work. All Gleeble samples (as-cast and transfer-bar) were provided by ArcelorMittal Dofasco (AM-D), Canada. Thermomechanical tensile tests were conducted at AM-D with the help of the R&D group, Dr. Joydeep Sengupta, Mr. Bruce Farrand, and Miss. Na Wu.

In **Chapter 1**, the introduction is allocated to a concise overview on different parts of literature review such as the importance of advanced high-strength steels (AHSSs), considerations during continuous casting process of steels, and the necessity of thermomechanical investigations on fabricating sound DP600 automotive parts.

In **Chapter 2**, the literature review is divided to three main sections contain a review on different generations of advanced high-strength steels (AHSSs), principles of the continuous casting process and its problematic issues, and some of the most reputed constitutive models that describe high-temperature and ultra-high-temperature thermomechanical behaviour.

In **Chapter 3**, the scope and objectives of the research project are given.

In **Chapter 4**, the experimental procedure including material selection, Gleeble thermomechanical experimental methods, and sample geometries used during high-temperature tests are discussed.

In **Chapter 5**, the results of the experimental analyses and a comprehensive discussion are provided to interpret the thermomechanical behaviour of DP600 AHSS.

In **Chapter 6**, to sum up the important points and contributions of this research, a brief conclusion followed by proposed recommendations for future works is given.

Table of Contents

Abstract	ii
Acknowledgements	iii
Preface	iv
List of Tables	viii
List of Figures	ix
Abbreviations and Symbols	xiii
Dedication	xvii
1 Introduction	1
2 Literature Review	3
2.1 Advanced High-strength Steels	3
2.1.1 Dual-phase AHSS	5
2.1.2 Mechanical Properties of DP AHSS	7
2.2 Fabrication Process of AHSS: Principles and Considerations	8
2.2.1 Continuous Casting of AHSS	9
2.2.2 Hot Embrittlement in Continuously-Cast Products	10
2.2.2.1 Effect of Thermal History	11
2.2.2.2 Effect of Chemical Composition	15
2.2.2.3 Effect of Microstructure	17
2.2.2.4 Effect of Cooling rate	18
2.2.3 Importance of Thermomechanical Analysis on Steel Processing	18

2.3	Plastic Flow Modeling	20
2.3.1	Medium-to-High Temperature Constitutive Models	21
2.3.1.1	Johnson-Cook (JC) Model	22
2.3.1.2	Khan-Huang (KH) Model	23
2.3.1.3	Hollomon-Voce (HV) Model	25
2.3.1.4	Rusinek-Klepaczko (RK) Model	27
2.3.1.5	Zerilli-Armstrong (ZA) Model	29
2.3.2	Constitutive Behaviour of DP AHSS	32
2.3.3	Ultra-High Temperature Constitutive Models	37
2.3.3.1	Garofalo Model	37
2.3.3.2	Han Model	38
2.4	Summary	39
3	Scope and Objectives	40
4	Experimental Methodology	42
4.1	Material	42
4.2	High-temperature Tensile Testing	43
4.2.1	Sample Geometry	46
4.2.2	Hot Ductility Measurement	47
4.3	Microstructural Evaluation	48
5	Results and Discussions	49
5.1	Microstructural Characteristics in As-received Materials	49
5.1.1	Structure and Texture	49
5.1.2	Ferrite Grain Size and Volume Fraction	53
5.2	High-temperature Constitutive Properties	54
5.2.1	Effect of Test Temperature and Cooling rate on As-cast Material	55
5.2.2	High-temperature Mechanical Properties of LGL Samples . . .	60
5.2.3	High-temperature Mechanical Properties of NGL Samples . .	62
5.2.4	High-temperature Mechanical Properties of SGL Samples . . .	62
5.2.5	Comparison between LGL, NGL, and SGL Samples' Data . .	63
5.2.6	Temperature Gradient and Fracture Area	67
5.3	SEM Analysis of Fracture Surfaces	70

5.3.1	Effect of Sample Geometry on Fracture Analysis	70
5.3.2	Effect of Test Temperature on Fracture Analysis	72
5.3.3	Effect of As-received Structure on Fracture Analysis	72
5.3.4	Fracture Mode of As-received Structures Tested at Near-peritectic Temperature	74
5.4	Effective Parameters on High-temperature Embrittlement of DP600 AHSS	76
5.5	Summary	80
6	Conclusions and Future Works	82
	Appendix	84
	Bibliography	87

List of Tables

2.1	Chemical composition of Heat TT-893 plain carbon steel [27]	13
2.2	Different functions proposed for strain rate sensitivity ($g(\dot{\epsilon})$) and thermal softening ($h(T)$) [45]	26
2.3	Values of the JC model's terms used in DP600 AHSS [68]	34
2.4	γ values and the HV model's coefficients in various DP AHSSs [45] .	36
4.1	Chemical composition of DP600 steel, wt%	43
5.1	Ferrite grain size and pearlite fraction in as-received materials	54
5.2	Critical temperatures measured by computational technique	54
5.3	Values of K_0 in δ and γ during solidification of binary iron alloys [101]	78

List of Figures

2.1	Regulation on automotive CO_2 emission legislated by different countries [1]	4
2.2	Elongation-tensile strength diagram for each generation of AHSSs [1]	6
2.3	DP AHSS as structural components in a typical vehicle [3]	7
2.4	Schematic diagram of a slab casting machine showing different sequences, (inset taken from [23])	10
2.5	Schematic diagram of the hot embrittlement zone in plain C-Mn and C-Mn-(low)Al steels	12
2.6	Effect of cooling cycles on hot ductility of plain carbon steel (adopted from [27])	14
2.7	Effect of heating cycles on hot ductility of plain carbon steel (adopted from [27])	15
2.8	Effect of carbon and phosphorus contents on hot ductility in 0.4%C plain carbon steel [36]	17
2.9	Hot embrittlement temperature ranges corresponding to microstructural features [43]	19
2.10	Stress-strain curves of Ta obtained by Khan-Liang model at different temperatures and strain rates [54]	24
2.11	Comparison between KHL and JC models to measure both quasi-static and dynamic strain rates and temperatures [44]	25
2.12	Stress-strain curves of DP780 at three temperatures: (a) experimental data, and (b) the normalized stress to reveal difference in strain hardening rates [45]	27

2.13	Effect of temperature and strain rate in quasi- and dynamic conditions on stress-strain curves obtained by the RK and its extended models [64]	30
2.14	Comparison between original and modified ZA models performed to measure the flow stress of IC10 alloy at various temperatures and strain rates [67]	32
2.15	Comparison of the flow stress, ultimate and yield tensile strength at various strain rates [68]	33
2.16	The response of stress-strain curves to variation of the strain rate between quasi- to dynamic values via the JC model in DP600 AHSS [68]	34
2.17	Measured strain rate sensitivity, m , for different grades of DP AHSS plotted by linearized Wagoner rate law [45, 69]	35
2.18	Comparison between the best-fit HV model and isothermal tensile test data for three grades of DP AHSS [45]	36
2.19	Torsion stress-strain curves of 301W stainless steel at different working temperatures [72]	38
4.1	Layout of the thermomechanical testing: (a) Gleeble 3500 apparatus, (b) machine's monitoring system, (c) DP600 Gleeble sample, (d) quartz tube to avoid oxidation of the gauge, (e) loading setup in the chamber contains grips and water-cooled copper blocks, (f) sample heated up to test temperature, and (g) assembly of the Gleeble sample and thermocouples that are attached on the surface	44
4.2	Thermomechanical regimes applied on (a and b) as-cast material, and (c and d) both as-cast and transfer-bar materials (sample codes are referred to the labels defined in subsection 4.3.1)	45
4.3	Sample geometries designed for the Gleeble test	46
4.4	Locations of R-type thermocouples prior to thermomechanical test	47
5.1	Optical micrographs of (a and b) as-cast, and (c and d) transfer-bar structures	51
5.2	BSE analysis of the transfer-bar and as-cast microstructures: The yellow and red arrows identify solute pile-up and depletion, respectively	52

5.3	Pseudobinary Fe-C phase diagram at constant Cr, Mn, Mo, Ti, and S, and the magnified region of the temperature interval tested in this study	55
5.4	Engineering stress versus displacement at various (a) test temperatures ($CR=3\frac{^{\circ}C}{s}$), and (b) cooling rates from holding to test temperature of 1300°C	57
5.5	Effect of test temperature on (a) RA - failure stress, and (b) RA - max engineering stress measured in Figure 5.4(a)	59
5.6	Stress-displacement curves and corresponding characteristics in (left column) as-cast, and (right column) transfer-bar LGL samples	64
5.7	Stress-displacement curves and corresponding characteristics in (left column) as-cast, and (right column) transfer-bar NGL samples	65
5.8	Stress-displacement curves and corresponding characteristics in (left column) as-cast, and (right column) transfer-bar NGL samples	66
5.9	Comparing constitutive data between different geometries of (a) as-cast, and (b) transfer-bar samples	67
5.10	Temperatures recorded by TC1 (thermocouple on the center) and TC2 (on the shoulder) for (a) TB-SGL, and (b) TB-LGL samples tested at 1300°C	68
5.11	The Gleeble test samples and their fracture surface area at 1400°C, (left column) as-cast, and (right column) transfer-bar materials	69
5.12	Fractographs of transfer-bar samples tested at 1300°C (Rows from top to bottom: NGL, SGL, LGL geometries at two magnifications)	71
5.13	Fractographs of as-cast NGL samples at three magnifications (Left column: tested at 1300°C, and Right column: tested at 1400°C)	73
5.14	Different magnifications of fractographs in NGL samples tested at 1300°C (Left column: AC, and Right column: TB initial microstructures)	74
5.15	Different magnifications of fractographs in LGL samples tested at 1450°C (Left column: AC, and Right column: TB initial microstructures)	75
5.16	Partial melted zones in LGL sample tested at 1300°C	77
5.17	Sulfur-rich phase and the EDS profiles of the primary and low-melting phases	78
5.18	Entrapped inclusion and its EDS profile	79

6.1	Correlation between flow stress and strain rate at various temperatures	85
6.2	Correlation between $\ln[\sinh(\alpha_\varepsilon\sigma)]$, $\ln\dot{\varepsilon}$, and $\frac{1}{T}$	85
6.3	Correlation between $\ln[\sinh(\alpha_\varepsilon\sigma)]$ and $\ln Z$	86

Abbreviations and Symbols

Symbol	Meaning
Abbreviations	
DP	Dual-Phase
AC	As-Cast
TB	Transfer-Bar
AHSSs	Advanced High-Strength Steels
AM-D	ArcelorMittal Dofasco
GBs	Grain Boundaries
ULSAB	Ultra-Light Steel Auto Body
HSSs	High-Strength Steels
UHSSs	Ultra-High-Strength Steels
FPR	Carbon-Fiber Reinforced Polymer
FB	Ferrite-Bainite
CP	Complex Phase
HPF	Hot-Press Forming
MART	Martensitic
TRIP	Transformation-Induced Plasticity
TWIP	Twinning-Induced Plasticity
SBIP	Shear-Band-Induced Plasticity
FCC	Face Centered Cubic
Q&P	Quenching and Partitioning
CCT	Continuous Cooling Transformation
GNDs	Geometrically Necessary Dislocations

UTS	Ultimate Tensile Strength
YS	Yield Strength
RF	Reheating Furnace
RA	Reduction of Area
HSLA	High-Strength Low Alloy
DIF	Deformation-Induced Substantial Ferrite
DRV	Dynamic Recovery
DRX	Dynamic Recrystallization
JC	Johnson-Cook
KH	Khan-Huang
HV	Hollomon-Voce
RK	Rusinek-Klepaczko
ZA	Zerilli-Armstrong
CR	Cooling Rate
ANN	Artificial Neural Network
BCC	Body Centered Cubic
KHL	Khan-Huang-Liang
NSRS	Negative Strain Rate Sensitivity
DSA	Dynamic Strain Aging
PSBs	Persistent Slip Bands
HDGI	Hot-Dipped Galvanized Coated
HDGA	Hot-Dipped Galvanneal Coated
DSC	Differential Scanning Calorimetry
DC	Direct Current
NGL	No Gauge Length
SGL	Short Gauge Length
LGL	Long Gauge Length
EDS	Energy-Dispersive X-Ray Spectroscopy
dDRX	Discontinuous Dynamic Recrystallization
SFE	Stacking Fault Energy
cDRX	Continuous Dynamic Recrystallization
BSE	Back-Scattered Electron

SE	Secondary Electron
TC	Thermocouple
α	Alpha-Ferrite
γ	Gamma-Austenite
δ	Delta-Ferrite

Nomenclature

k_0	Partition coefficient
T, T^*, T_r, T_m	Absolute, homologous, reference, melting temperatures
$\dot{\epsilon}$	Absolute strain rate
$\dot{\epsilon}^*$	Reference strain rate
A_{JC}	Yield stress at a reference temperature and strain rate in JC model
B_{JC}, C_{JC}	Strain hardening, strain rate hardening coefficients in JC model
n	Strain rate hardening
m	Thermal softening exponents
m	Strain rate sensitivity
σ_f	Failure stress at room temperature
ϵ_f	Failure strain at room temperature
σ_{ry}	Reference yield stress
r_i, P_i	Fitting coefficients
T_A	Ambient temperature
C_1	Rate sensitivity in the quasi-static strain rate regime at ambient temperature
C_2	Rate sensitivity in the dynamic strain rate regime at ambient temperature
σ	Von Mises equivalent stress
ϵ	Accumulated plastic strain
$\dot{\epsilon}$	Equivalent plastic strain rate

$E_{\infty}, \sigma_0, a, A, B, n_0, n_1, c$	Material constants
$\alpha_1, \alpha_2, H_{HV}, n_{HV}, A_{HV}, B_{HV}$	Material constants
$B_0, D_1, D_2, m^*, \sigma_0^{ns}, D_3, \gamma_1, \gamma_2$	Material constants
D_0^P	Invariant of the plastic deformation rate
σ_{μ}	Internal stress caused by strain hardening
σ^*	Effective stress by thermally-induced activation processes
θ^*	Characteristic homologous temperature
v	Temperature sensitivity
n_0	Strain hardening exponent
$\dot{\epsilon}_{min}$	Lower limit of the RK model
$\dot{\epsilon}_{max}$	Maximum strain rate for a particular material
σ_{ns}	Equivalent Huber-Mises stress
$\sigma_{ath}, \sigma_{th}$	Athermal, thermal flow stresses
$\dot{\epsilon}_{trans}$	Transitional strain rate between positive and negative strain rate sensitivities
M	Taylor factor
b	Magnitude of the Burgers vector
ρ_m, ρ_0	Mobile, initial dislocation density
$\Delta G_0, A$	Gibbs free energy of thermal activation, activation surface area at 0K
β	strain and strain rate parameter
σ_{Pr}, σ_Q	stresses of a random points P, Q on the reference
$\sigma_{\dot{\epsilon}_0}$	stress corresponding to $\dot{\epsilon}_0$
$A_{\epsilon}, \alpha_{\epsilon}, n_{\epsilon}$	Strain-dependent parameters
Q_{ϵ}, m	Apparent activation energy, strain-rate sensitivity
$\dot{\epsilon}_P, \sigma_{0,P}$	Plastic strain, yield strength of porous material
σ_0	Yields strength of sound material
A_0, A_f	Initial and ultimate cross-sectional area of the test sample
r	Radius of curvature

*To my beloved Parents
who generously support me in my life and career
& my Brother
for all encouragement*

Chapter 1

Introduction

There is currently an increasing worldwide demand for advanced high-strength steels (AHSSs), where the main usage is found in the automotive and construction industries. Over the last decades, the automotive industry has continuously improved vehicle performance and safety reliability, however, green-house gas emissions have become a problematic issue. AHSS grades are suitable candidate to simultaneously provide high strength to weight products with good ductility, bake hardenability and corrosion resistance. These alloys allow industry men to produce lighter vehicles, whilst the safety reliability is still being satisfied. Among AHSSs, dual-phase (DP) first generation steel is widely used in load-bearing parts of body-in-white, *i.e.* the vehicle frame regardless its moving parts, thanks to its high toughness and formability. The variety of costly alloying elements in DP AHSS necessitates meticulous steel processing and quality to decrease the risk of product rejection.

Continuous casting, as the main industrial process to fabricate AHSSs, is always accompanied with process difficulties that bring extra costs to the fabrication cycle. In this category, hot embrittlement is one of the most well-known phenomenon. It represents the lack of ductility within 700-1200°C, when the steel product mostly contains austenite grains surrounded by a thin layer of ferrite along grain boundaries (GBs). In this temperature range, thermomechanical processing leads to precipitates embedded into the thin α layer causing embrittlement. There are different factors like thermal history, chemical composition, grain size, strain and cooling rates that play roles on the severity of this defect. There have been many efforts to comprehend factors affecting the hot embrittlement by means of Gleeble apparatus, *i.e.* a ther-

thermomechanical simulator that is able to apply tensile and compressive loads at high temperatures associated with various thermal regimes and strain rates.

Despite the majority of efforts allocated to the temperature range of 700 to 1200°C, conducting thermomechanical tests between 1200°C and solidus temperature has usually been neglected. Once the structure is subjected into this temperature interval, softening mechanisms which were already activated at lower temperatures will be no longer stable. For instance, dynamic recovery and recrystallization will be replaced by grain growth of the γ phase. Moreover, short-length diffusion paths through the γ grains at 700-1200°C will evolve to long-range diffusion which spreads beyond neighboring grains and drags the boundaries, also called grain boundary sliding. Hardening mechanisms, on the other hand, ascribed at medium-to-high temperatures to factors such as triple junctions and GBs as dislocation barriers, changes in stacking fault energy during γ to δ phase transformation, and strengthening by secondary phases, are modified at ultra-high temperatures to localized hardening due to strain fields around high-temperature carbides and inclusions. Performing thermomechanical analysis on as-cast and transfer-bar DP600 samples within the mentioned temperature range will allow for interpretation of austenite grain growth, inclusions, low-melting temperature phases, and porosity on high-temperature mechanical properties.

Besides all thermal and microstructural considerations, the geometry of tensile sample plays another important role in ensuring that the data collected from tensile simulation matches the real situation happened during the high-temperature tensile test. Parameters such as length of the gauge and radius of the shoulder directly affect thermal gradient through the gauge and strain localization during uniaxial tensile test. Designing a suitable sample geometry in which less strain localization associated with necking right on the hot-spot zone, *i.e.* the hottest dot on the surface of the gauge, will help to attain a reliable reproducibility between data recorded by the Gleeble test for different experiments. Based on the industrial need for improving the processing of AHSSs, there is necessity for improved knowledge of high-temperature constitutive properties especially yield strength and ductility. The next chapter outlines past literature on these topics and identifies further area for research.

Chapter 2

Literature Review

First, a concise literature review on the different generations of advanced high-strength steels (AHSSs), especially dual-phase (DP) series and their applications and mechanical properties is presented. Second, the continuous casting process is introduced as the main industrial fabrication process of AHSSs and some notable principles during this process such as top-down sequences of solidification and hot rolling of the steel slabs as well as hot embrittlement phenomenon which has deleterious effect on the ductility of post-processed steel product are discussed. Third, the most well-known constitutive models to evaluate high-temperature mechanical behaviour of the material subjected to a combination of strain, strain rate, and temperature are presented. Finally, applications of two constitutive models on prediction of constitutive behaviour of DP AHSSs is explained.

2.1 Advanced High-strength Steels

Enhancement in petroleum consumption and greenhouse gases as a result of yearly growth in world-wide population has necessitated green automobiles with lower CO_2 emission and higher fuel efficiency. Regulation on the average fuel economy of cars and light trucks, which began in the United States in 1975 motivated other countries to legislate CO_2 emission levels. Figure 2.1 shows current laws of CO_2 emission for major countries [1]. For this purpose, technology improvements in different ways *e.g.* materials selection, structural design, and functional efficiency of electrical systems in automobile are necessary. In 1994, an international consortium of sheet steel pro-

ducers comprising 35 companies from 18 countries was launched to develop new steel grades that overcome the lightweight challenges [1]. The ultra-light steel auto body (ULSAB) was initially propounded in that consortium to explore how to save weight via automotive components made of higher strength steels [1]. These efforts led to the first car body “body-in-white” made from 90% high-strength steels (HSSs). That car body was 25% lower in mass and 14% less in cost, while the torsion and bending stiffness were enhanced by 80% and 52%, respectively [1].

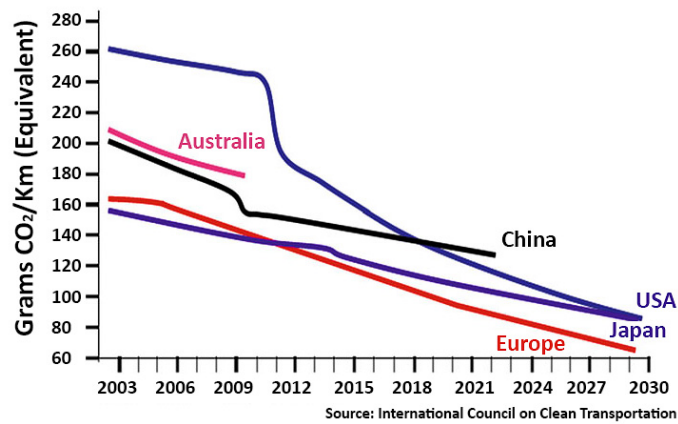


Figure 2.1: Regulation on automotive CO_2 emission legislated by different countries [1]

In terms of materials selection, steels as a low-cost material as compared with other commercial products including aluminum, magnesium, and carbon-fiber reinforced polymer (FPR) composites are widely used in the automotive industry [2]. Its multiple characteristics such as high toughness, suitable weldability and formability, and good corrosion resistance make this material the best candidate to fabricate the majority of automobile structural components. During the last two decades, to achieve light weighting, many efforts have been put on microstructural changes in steels. Toward this end, HSSs, ultra-high-strength steels (UHSSs), and finally, AHSSs have been invented based on their chemical composition and phase combination at room temperature [1, 2]. The AHSSs were developed specifically to ameliorate the impact resistance and resilience modulus of car body material while maintaining excellent strength to weight. The AHSS designation is attributed to any kind of steel with at least 500MPa tensile strength, and contains different phases *e.g.* bainite, martensite, and retained austenite [3, 4]. Four various strengthening mechanisms of solid solu-

tion, precipitation, grain refinement, and phase transformation, are used to strengthen AHSSs. As schematic of the strength/ductility relationship for AHSSs is given in Figure 2.2, there are three generations of AHSS, categorized based upon microstructural features, their tensile strength and ductility,

(1) First generation AHSS: This group mostly contains ferrite phase as a matrix reinforced by the other phases like martensite or bainite. The DP, ferrite-bainite (FB), complex phase (CP), hot-press forming (HPF), transformation-induced plasticity (TRIP), and martensitic (MART) steels are categorized in this generation which commonly have 500-1600MPa UTS, 300MPa YS, and 5-30% ductility [3, 5]. The main drawback of the first generation AHSSs is low ductility and hence relatively low toughness [3].

(2) Second generation AHSS: The microstructure of this group is commonly austenitic due to the addition of austenite-stabilizer elements *e.g.* Mn, Cr, and Mo. This category can be mostly divided to high manganese TRIP assisted, twinning-induced plasticity (TWIP), and shear-band-induced plasticity (SBIP) steels that show suitable combination of high strength and ductility [3, 5]. Better ductility is mainly ascribed to shear banding effects in face-centered cubic (FCC) structure of austenite matrix. Although the second generation AHSSs show high toughness as compared to the first generation AHSSs, high production cost due to the high amounts of alloying contents (up to 17-22wt% Mn), casting and welding difficulties make them less commercial and applicable in industry [1, 6].

(3) Third generation: This group has been developed to tradeoff material cost and mechanical properties of 1000MPa UTS and 30% total elongation with supposedly consisting of martensite and austenite structure [3]. The main steels of this category includes duplex medium-Mn TRIP, carbide-free bainitic steels, and quenching and partitioning (Q&P) steels [1, 7].

2.1.1 Dual-phase AHSS

DP steels are the most famous first-generation AHSSs. They usually contain pockets of martensite as a hard phase dispersed into 60-90% volume fraction of ferrite matrix phase [6]. Traditionally, martensite is the only non-ferritic phase in DP steels, however, other phases like bainite and retained austenite may also be observed in

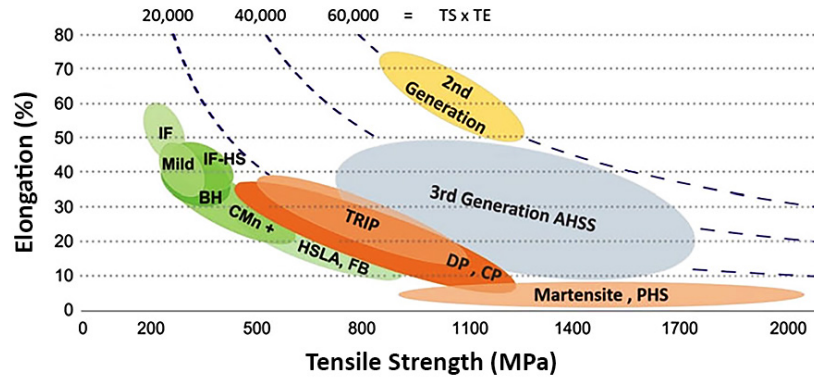


Figure 2.2: Elongation-tensile strength diagram for each generation of AHSSs [1]

microstructure of steels based on processing history or the addition of a γ stabilizing element. The chemical composition of DP AHSS usually contains 0.06-0.15wt% C, 1.5-3wt% Mn, 0.05-0.2wt% Si as well as small amounts of microalloying elements like Nb, V, Cr, and Mo [5, 6]. Carbon element is added to stabilize austenite, strengthen the martensite and control the phase distribution, while Mn acts as both austenite stabilizer and ferrite matrix strengthener. The addition of Mn also leads to an increase in hardenability due to a shift in the continuous cooling transformation (CCT) diagram to the right side. Ferrite strengthening can be also achieved by Si addition which promotes the ferritic transformation, or V and Nb by impinging the GBs, and consequently, grain refinement strengthening [8]. The role of Cr and Mo addition up to 0.4wt% has been also reported as a barrier against perlitic and bainitic transformation during heat treatment of DP AHSSs [6].

Microstructure of DP AHSS can be obtained by cooling of low-carbon microalloyed steel to the intercritical region between the A_1 and A_3 temperatures, soaking into this interval to form ferrite, and after that rapid quenching below the martensite start temperature to transform austenite into martensite. This kind of treatment, called intercritical annealing, leads to coarse ferrite/martensite microstructure. In contrast, in industrial thermomechanical treatment involving hot rolling followed by water quenching, fine grain structure with well-distributed martensite pockets can be achieved [6]. As illustrated in Figure 2.3, the combination of a low yield ratio of about 0.5 and high strength values ranged between 500 and 1200MPa in DP AHSSs will offer a wide range of applications from crumple zone to body structure in the automotive industry [6, 9].

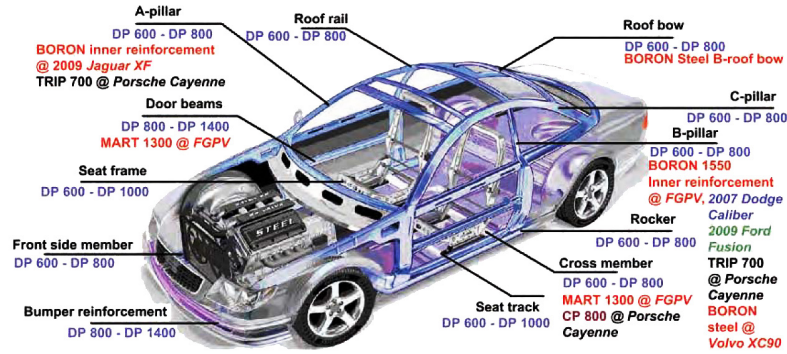


Figure 2.3: DP AHSS as structural components in a typical vehicle [3]

2.1.2 Mechanical Properties of DP AHSS

The tensile behavior of DP AHSSs attracts much interest in the metal forming industry due to continuous yielding, high initial work hardening, and a low yield-to-tensile strength ratio. These properties can be mainly attributed to two phenomena:

(1) Austenite to martensite transformation will be accompanied by nearly 3-4% volume expansion constrained by primary ferrite phase. Hence, residual tensile stress will be stored in ferrite matrix, whereas martensite phase will be subjected to compressive stress. Further, mobile dislocations commonly pile up near the ferrite/martensite interfaces to relieve and neutralize these elastic residual stresses [10]. Plastic flow generally begins simultaneously at many potential sites, and subsequently, continuous yielding associated with suppression in Luders-band formation is observed in DP AHSSs.

(2) Plasticity mismatch between constitutive phases, *i.e.* hard-deformable martensite embedded into soft ferrite matrix makes inhomogeneous strain induced microstructure during plastic deformation [11]. This incompatibility tends to evolve back-stresses and generate the geometrically necessary dislocations (GNDs) in ferrite to activate work hardening [11-13].

The DP classification is basically named based upon value of ultimate tensile strength (UTS). For instance, an AHSS classified as DP600 is expected to have 600MPa UTS. At lower volume fraction of martensite, linear trend in increase of both yield strength (YS) and UTS has been reported [14]. In spite of macrohomogeneity during DP deformation, the plastic deformation will be heterogeneous at the micro-scale due to

different response of ductile ferrite and brittle martensite phases to the applied loads [15]. Ductility and formability of DP AHSSs non-linearly decrease with an increase in volume fraction of martensite and slightly enhanced at lower carbon content. Uneven work hardening of DP AHSSs can be categorized to three stages:

(1) Strain interval of 0.1-0.5%: Residual stresses generated by martensitic transformation will be consumed and both ferrite and martensite will experience homogenous deformation associated by elastic-to-plastic transition in ferrite [10].

(2) Strain interval of 0.5-4.0%: Homogenous to inhomogeneous deformation of ferrite matrix results in contribution of back stresses and GNDs to the overall work hardening [16, 17]. This stage becomes more dominant when the ferrite phase is subjected to larger inhomogeneous deformation and will continue until saturation of back stress contribution and GND hardening effect.

(3) The last stage is just prior to fracture and ascribed to dynamic recovery effects caused by nucleation of dislocation cell substructures in ferrite grains, and consequently, more homogeneous deformation in both phases [18].

2.2 Fabrication Process of AHSS: Principles and Considerations

Since the 1970s, steel research has been conducted to understand various industrial processes that could be applied to fabricate duplex DP microstructures within the Fe-C-Mn and Fe-C-Si alloying systems [19-21]. Ultimately, two separate thermal treatment were accepted by industry men,

(1) Hot rolling followed by cooling from single austenite-phase region into intercritical zone ($\alpha + \gamma$) and quenching to ambient temperature.

(2) Hot rolling continued by cooling to room temperature, heating up into intercritical zone ($\alpha + \gamma$) and quenching to ambient temperature.

Although the post-treatment parameters *e.g.* holding time, temperature, quench bath and size of bulk material are very important to determine ultimate physical and mechanical properties of DP AHSS, less attentions has been paid to thermal and solidification history of material prior to intercritical heat treatment. The microstructural history during casting also plays an important role in the industrial

solidification process of AHSS and will critically affect segregation, hot tearing, and solid-state hot embrittlement susceptibility. Thus, to guarantee soundness of ultimate structures, understanding both solid-, and mushy-state constitutive behaviors during solidification and cooling paths are crucial.

2.2.1 Continuous Casting of AHSS

The continuous casting process of steels has been basically founded on teeming liquid steel vertically into a water-cooled copper mold as shown in Figure 2.4. Heat transfer through the wall of the mold is responsible for the formation of a solid skin which becomes thicker down the length of the copper mold.

After achieving the suitable thickness in the solidified skin to support the liquid steel, the strand moves downward, and further cooling is accomplished by water sprays. The efficiency of heat transfer is decreased toward the length of the copper mold due to an air gap forming between the copper wall and the outer side of the solidified skin caused by the skin cooling and contracting. Therefore, the copper mold cooling is followed by water spraying. After complete solidification of the strand, rollers straighten the strand and push that into power-driven pinch rolls. Product is cut via a torch and accelerated down a roller table for further processing. Terminology of different as-cast sections in steel production is determined based upon the dimension of cross section and categorized as Billets (square section with area up to 150mm^2), Blooms (square or rectangular cross-section greater than 150mm^2 to as large as $800 \times 400\text{mm}^2$), and Slabs (more than 2 as an aspect ratio with dimension of $2725 \times 254\text{mm}^2$) [22].

In Figure 2.4, the continuous casting process is accompanied by heating the as-cast slab in reheating furnace (RF) and rough rolling to provide transfer bars from as-cast steel products [23, 24]. Since the temperature of the steel slab drastically decreases after delivery from the slab yard, the product should be heated up to $1200\text{-}1250^\circ\text{C}$ in the RF before starting rough rolling process. Furthermore, not only does heating in the RF remove dendritic structure of as-cast slab, but it also homogenizes most of alloying elements that became segregated during continuous casting [25]. After that, rolling of the slab within the roughing stands leads to a reduction in the thickness of the transfer bar from almost $200\text{-}300\text{mm}$ to approximately 50mm through four or five passes. Meanwhile, the temperature during rough rolling is high enough in which the

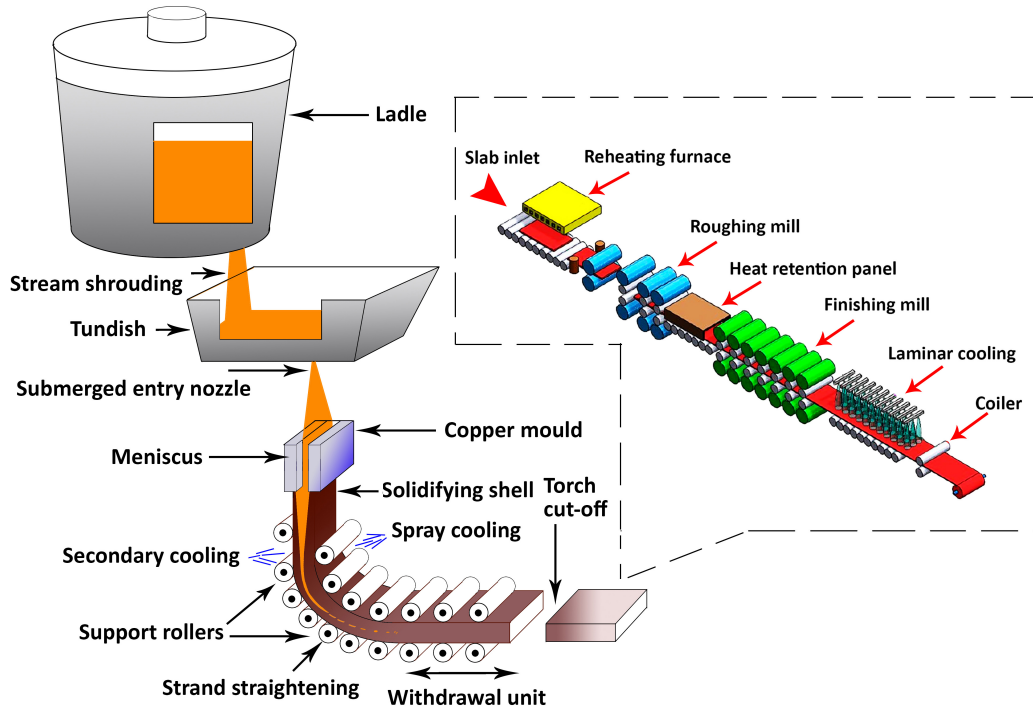


Figure 2.4: Schematic diagram of a slab casting machine showing different sequences, (inset taken from [23])

transfer bar is fully recrystallized, containing strain free, equiaxed grains.

Ultimately, the transfer-bar product commonly shows temperature difference between its head and tail due to radiation heat dissipation, heat conduction of roll mills beneath the conveyors, and convective heat dissipation of air, and consequently, different physical and mechanical properties [23]. Therefore, post processing followed by transporting transfer bars into heat retention panel via conveyors is employed to minimize thermal gradient and ease finishing rolling. The finish rolling is traditionally composed of five to seven tandem stands supported by large diameter back-up rolls and smaller diameter work rolls. The strip exits from finish rolling is usually 1-4mm thick and coiled for further processing *e.g.* cold rolling and deep drawing in other industrial units [25].

2.2.2 Hot Embrittlement in Continuously-Cast Products

Transverse cracking during continuous casting is a very common defect taking place when rollers straighten the strand. Based upon the chemical composition of steel products, the temperature range in which the slab will be prone to this defect varies

between 700 to 1200°C and the microstructure usually contains austenite grains surrounded by primary-ferrite thin layer elongated through the γ GBs [26]. The continuously-cast product exposed to this temperature interval shows low ductility, usually quantified as a reduction of area (RA), and brings extra costs and problematic secondary processing such as repairing the slab via scarfing before rolling (particularly in expensive grades of Nb-contained and High-strength Low Alloy (HSLA) steels), and direct charging of sound warm or hot slabs into the RF. As seen in Figure 2.5, the curve of hot ductility, *i.e.* the amount of hot deformation which a specific material can accommodate with no severe cracking or fracture in plain carbon steels, usually consists of three regions:

(1) Zone I: Good ductility due to the presence of higher volume fraction of deformation-induced substantial ferrite ($DIF \geq 45\%$) in the structure which can tolerate most of the strain caused by both phase transformation and thermal expansion within the process rather than the austenite phase.

(2) Zone II: Severe embrittlement as a result of segregation of sulfur during solidification and precipitation of alloying elements *e.g.* Mn, N, Al, and Nb via solid-state diffusion along the austenite GBs. These compounds entrapped in the DIF encourage void formation and coalescence which ultimately cause ductile intergranular failure. Also, creep-assisted grain boundary sliding in austenite phase followed by cracking is considered as the other embrittlement mechanism.

(3) Zone III: Improvement in ductility at high temperature because of thermal softening phenomena like dynamic recovery (DRV) and recrystallization (DRX). In addition, the grain boundary sliding annihilates the strain localized along the initial GBs and prevents intergranular failure. Although the DIF withstands the DRX occurrence, this phase no longer stands at temperatures above the Ae_3 .

2.2.2.1 Effect of Thermal History

In 1973, Wilber *et al.* [27] conducted various high-temperature tensile cycles using a Gleeble machine on plain carbon steels to show how important thermal history was in governing hot ductility. For these tests, the composition with high Mn to S ratio was chosen, as given in Table 2.1. In all as-cast samples, a fine cellular-dendritic microstructure was achieved similar to that found within the chill zone of

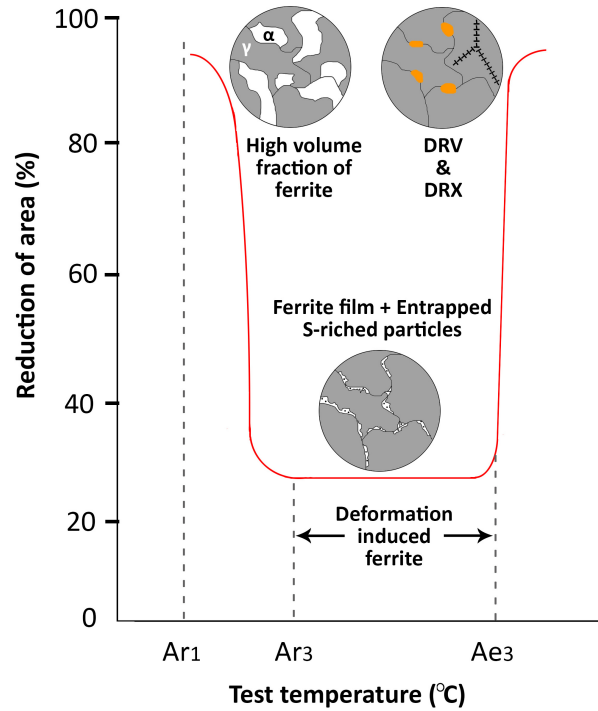


Figure 2.5: Schematic diagram of the hot embrittlement zone in plain C-Mn and C-Mn-(low)Al steels

a continuously-cast slab. As shown in Figure 2.6(a), thermal cycles of C_1 (cast and free-cooled from above liquidus temperature, 1532°C , to indicated test temperature) and C_2 (same as C_1 with 10min holding at each test temperature) elucidated totally different manner through the trend of fracture diameter values (inversely proportional to RA). Relied on the measured temperature of γ to α transformation, 871°C , the C_1 cycle surprisingly shows abrupt decrease in ductility within the single phase γ below 1204°C , *i.e.* austenite ductility transition. The C_2 cycle obviously reveals the detrimental effect of holding time at higher temperature on the hot ductility of the steel material.

In Figure 2.6(b), the authors meticulously selected two intercritical temperatures of 1371°C (C_3) and 1204°C (C_4) corresponding to upper and lower temperature bounds where the hot ductility shows abrupt changes in its own value (C_1). For both cycles, samples were subjected to mentioned intercritical temperatures for 10min before further cooling to indicated test temperatures. As can be seen, although the material subjected to 1371°C and 1204°C , respectively showed high and low hot ductility in the reference cycle (C_1), the deleterious effect of higher holding temperature for C_3

Table 2.1: Chemical composition of Heat TT-893 plain carbon steel [27]

<i>Chemical Composition (wt%)</i>								
<i>C</i>	<i>Mn</i>	<i>P</i>	<i>S</i>	<i>Si</i>	<i>Al</i>	<i>N</i>	<i>O</i>	<i>Mn/S</i>
0.05	0.40	0.007	0.012	0.65	0.006	NA	NA	33

plays a much more dominant role in deteriorating the hot ductility properties of the material as compared with the C_4 cycle. Figure 2.6(c) shows the other fact that increasing the holding time from 1 to 10min at each test temperature will reduce the slope of the drastic drop in hot ductility, where C_5 was directly cooled to indicated temperatures with no halt through the intercritical temperature. Finally, cycle C_6 is assigned to a situation in which samples are reheated directly to test temperatures after cooling through the γ to α transformation. As seen in Figure 2.6(c), there is no ductility transition on reheating thermal schedule, but instead, the maximum level of hot ductility at all test temperatures are exhibited for all specimens. As a conclusion, the austenite ductility transition is strongly dependent on the thermal history during cooling prior to testing.

On the other side, Figure 2.7 demonstrates the influence of heating cycle regardless of preliminary melting and casting procedures on the hot ductility behaviour of wrought (hot worked) Heat TT-893 steel. Thermal cycle W_1 which is referred to heating specimens directly to each test temperature, holding for 2min and doing a Gleeble tensile test leads to achieving the maximum hot ductility at all temperatures, Figure 2.7(a). Wilber *et al.* [27] also showed that at constant test temperature of 1093°C, an increase in either the intercritical temperature - which is higher than the test temperature - or the holding time at corresponding temperature suppresses the hot ductility of the steel followed W_2 cycle, however, the effect of intercritical temperature is greater, Figure 2.7(b).

Heating samples up to the intercritical temperatures of 1482 (W_3) and 1317°C (W_4), holding for 1 and 2min, respectively, and subsequently free-cooling to each test temperature emerge the austenite ductility transition which was no longer stable for W_1 heating regime, Figure 2.7(c). In this situation, there is an approximate coherency between W_3 and C_1 trends which can allow us to predict the hot ductility in different

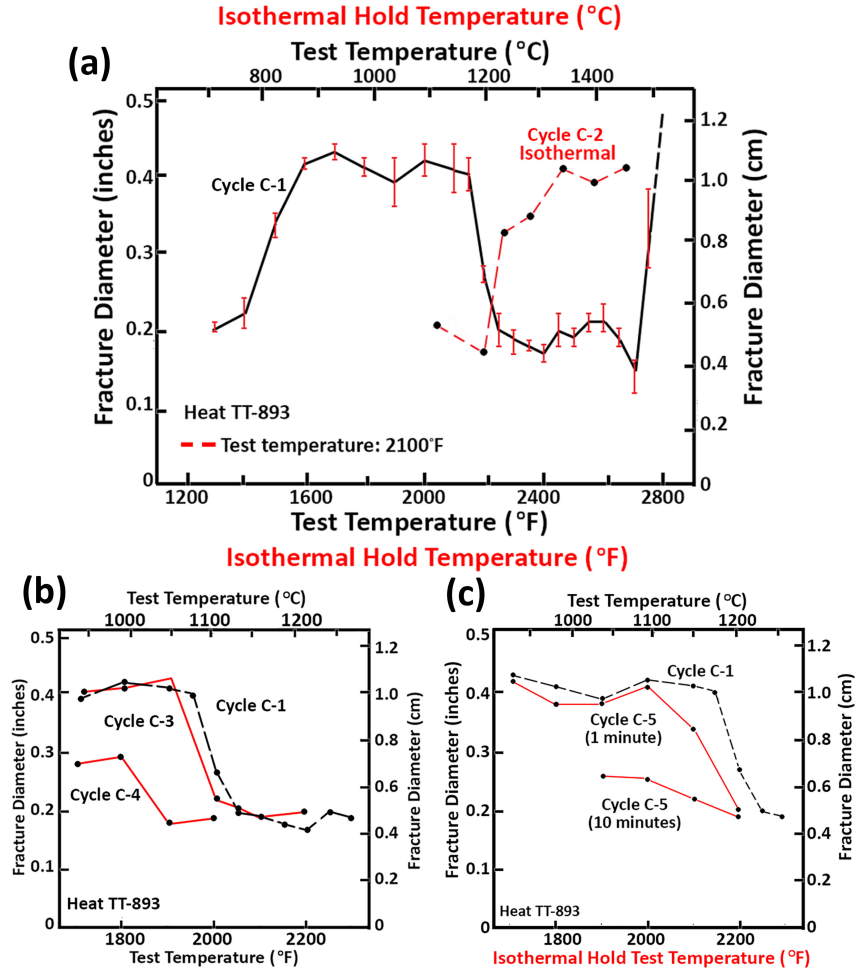


Figure 2.6: Effect of cooling cycles on hot ductility of plain carbon steel (adopted from [27])

sections of continuously-cast slabs during cooling by means of conducting the heating regime following the W_3 cycle, even within higher holding time to reduce the gap between two diagrams. Lower hot ductility in W_3 as compared with W_4 is attributed to the higher intercritical temperature coincided with δ -ferrite region, remelting the low melting-point phases, and subsequently, synergy between re-segregation of S element and precipitation of (Mn, Fe)S particles alongside the boundaries of regrown γ grains. Sulfur segregation would tend to lower the bonding energy and cohesion of GBs, resulting in strain localization to initiate the grain boundary sliding. As a result, void nucleation and coalescence around the intergranular (Mn, Fe)S precipitates cause further strain concentration and propagation of grain boundary microcracks associated with an increase in system entropy.

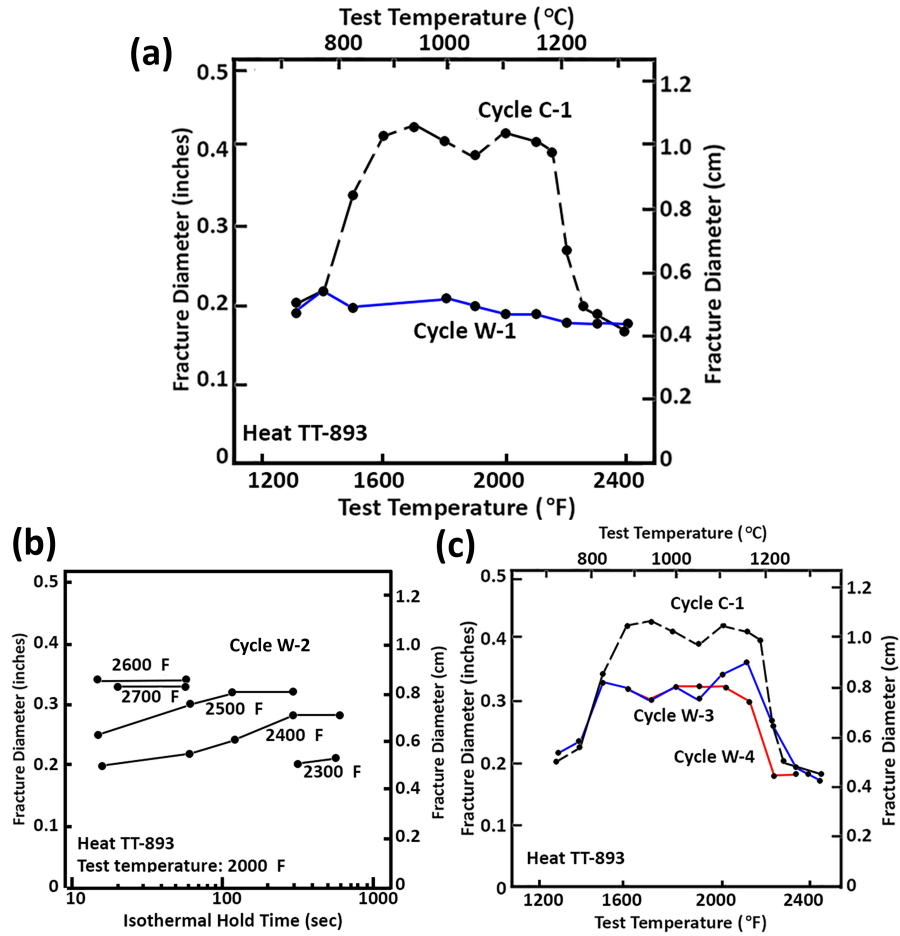


Figure 2.7: Effect of heating cycles on hot ductility of plain carbon steel (adopted from [27])

2.2.2.2 Effect of Chemical Composition

The effect of microalloying elements on the depth, position and width of the ductility trough could be regarded as relying on the role of elemental contents on strain to fracture, the kinetic of transformation, and the DRV in terms of variation in stacking fault energy due to the Suzuki hardening effect, *i.e.* segregation of solute atoms to stacking faults which makes dislocations slip harder. **Carbon** changes the hot ductility of medium-level carbon steels by affecting the kinetic of γ grain growth. Since the proposed mechanism for hot embrittlement is intergranular failure, which is closely dependent on the onset point of the γ to α transformation, raising the carbon level lowers the transformation temperature, and consequently, shifts the trough to lower temperatures. Such a movement in the trough temperature as well as an increase in the depth of ductility drop are more obvious in steel grades containing 0.05 to

0.3% carbon content [28]. On the other hand, an increase in **Silicon** as an α -ferrite stabilizer from 0.3 up to 1.22% in high-silicon TRIP steels slightly diminishes the hot ductility by moving the trough to higher temperatures [29]. Since the intergranular failure is aggravated with formation of DIF along the GBs of γ , enhancement in Si addition will expose the structure to the vulnerable zone at higher temperatures. **Manganese** as a key element in steel processing, particularly in TWIP steels, should be considered from two aspects of view: the role of Mn itself on the depth of trough, and the ratio of $\frac{Mn}{S}$ to prevent occurrence of classic hot shortness due to liquid film formation of low melting-point S-rich compound, FeS, at austenite GBs. Mn as a γ stabilizer makes the trough shallower and moves that to lower temperatures. Wide stabilized austenitic region provides a good opportunity in which grain coarsening of γ will be lingered and increase in grain size retards creep-assisted straining within the vulnerable zone. In terms of $\frac{Mn}{S}$ ratio, even though Wilber *et al.* [27] reported the continuous improvement in hot ductility with an increase in $\frac{Mn}{S}$ even up to 75, Cardoso *et al.* [30] declared that manganese sulphide plays a key role on hot ductility by accumulating the localized strain within the DIF narrow film. Therefore, more the manganese sulphide phase, the easier microvoids coalescence and cracks nucleation, to cause hot embrittlement. **Aluminum** addition to steels can lead to transverse and edge cracking of the continuously-cast slab as a result of the formation of AlN preferentially precipitated at the γ GBs [31, 32]. The detrimental mechanism of AlN precipitates is encouraging the γ grain boundary sliding and developing the intergranular cracking by pinning the austenite GBs. Crowther *et al.* [33] reported that AlN does not precipitate dynamically, and that precipitation kinetics will be ceased unless the term $[Al \times N]$ exceeds 3×10^{-4} . **Phosphorus** and **Sulfur** impair the hot ductility properties of steels because of the high partition coefficient (k_0) in both δ -ferrite and γ -austenite, which results in severe segregation towards GBs, and intergranular failure. Harada *et al.* [34] suggested that longitudinal and transverse cracking occurring during the continuous casting will be originated by intense microsegregation of P to regions underneath the roots of oscillation markings, where the solidified shell is deformed and highly-segregated liquid becomes entrapped into intercolumnar channels. In other research, Mintz [35] reported the beneficial effect of P up to 0.02% in Nb-contained steels due to the fact that P segregates to boundaries and vacant

sites to prevent precipitation of more detrimental Nb(C, N) fine particles. In spite of the harmful effect of P element on hot ductility of steels, grades with carbon content lower than 0.25% shows infinitesimal sensitivity to P content, as shown in Figure 2.8 [36].

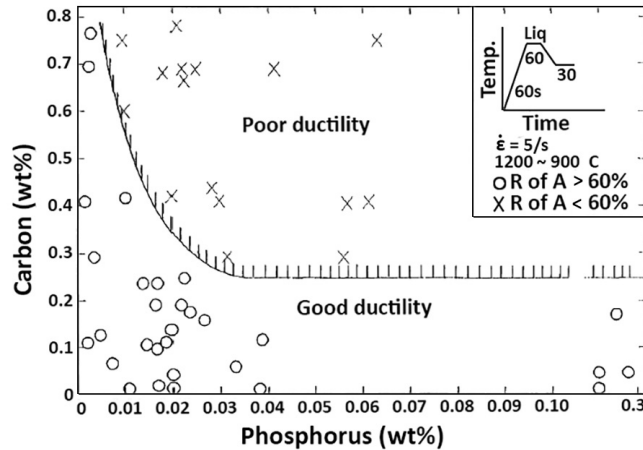


Figure 2.8: Effect of carbon and phosphorus contents on hot ductility in 0.4%C plain carbon steel [36]

2.2.2.3 Effect of Microstructure

The effect of microstructure can be seen through the grain size, precipitates, and inclusions. As the first important microstructural feature on hot ductility, the grain size of the solidified slab should be taken into account as strong influences on the ease of creep. Although there have been some contradictory evidence on how the grain size can affect the hot ductility, most research expressed that grain refining improved the hot ductility [37-40]. Under the situation of intergranular failure, refining the grain size controls crack propagation by:

- (1) Decreasing the crack aspect ratio which brings less stress concentration at the tip of crack.
- (2) Generating more triple junctions as a strong barrier against the propagation of smaller cracks nucleated by sliding.
- (3) Increasing the specific area of γ GBs led to lowers the number of accumulated precipitates.
- (4) Activating numerous nucleation sites of the GBs followed by reduce in the critical strain for the DRX.

As the second important microstructural factor on hot ductility, the presence of precipitates and inclusions highly affect the hot ductility based upon their size, distribution, and physical properties. Fine precipitates allow the crack to join up by pinning the GBs. Both precipitates and inclusions also facilitate formation of microvoids coalesced to accelerate failure. The size of each precipitate category is a good indication of how the formation of the corresponding precipitate was being proceeded, for instance, AlN, Nb(C, N), and V(C, N) are strain induced precipitates dynamically formed as fine compounds, while statically formed particles usually show coarser morphology. As a conclusion, the precipitates statically present before deformation have much deleterious influence on the hot ductility rather than those dynamically formed during deformation.

2.2.2.4 Effect of Cooling rate

The average cooling rate measured on the slab surface, *i.e.* from the copper mould downward into the strengthening rollers, shows 50-100 $\frac{^{\circ}\text{C}}{\text{min}}$ in conventional continuous casting (220 to 250mm thick slab) and 200-300 $\frac{^{\circ}\text{C}}{\text{min}}$ for thin slab casting (60 to 80mm thick slab). For solution-treatable steel grades, increasing the cooling rate to the test temperature results in deeper ductility trough which is ascribed to reprecipitation of fine sulphide along the GBs of γ phase. As discussed before, a decrease in spacing between fine particles (at constant volume fraction) makes them more prone to localize strain causing cracks linkage and growth [41]. The effect of this parameter on the hot ductility dramatically shows its significance when the solidifying surface of the strand is subjected to very high cooling rates during cooling above the meniscus. In this case, precipitates entrapped within the DIF diminish the hot ductility because of their fine morphology caused by short-path solid-state diffusion of constitutive elements [42].

2.2.3 Importance of Thermomechanical Analysis on Steel Processing

As discussed earlier, the hot ductility is an important parameter in steel technology, since it allows the operator to determine the quality of the final products. In terms of the mechanism of failure during the hot ductility test, zones vulnerable to brittle fracture at high temperature corresponded to either crack nucleation and propaga-

tion within liquid pockets along the GBs and triple junctions, called hot tearing, or intergranular high-temperature brittle fracture in the solid state. Hot ductility data under conditions which more closely simulate those during continuous casting provides good information about high-temperature mechanical behaviour of steels affected by temperature, strain, and strain rate, simultaneously. Regardless of the hot tearing mechanism during solidification, the solid-state hot embrittlement is accompanied by many thermal-, physical-, and mechanical-assisted phenomena which make its interpretation complicated, Figure 2.9 [43].

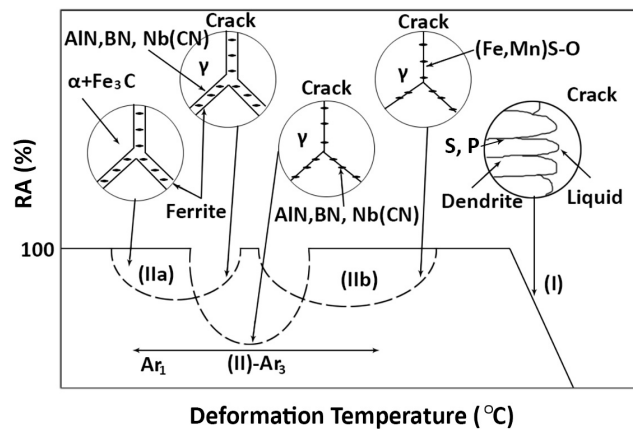


Figure 2.9: Hot embrittlement temperature ranges corresponding to microstructural features [43]

Since providing a simulated condition governing over the real continuous casting process is nearly impossible, *in-situ* analysis of thermomechanical properties during solidification and cooling has been usually declined. So that, researchers try to present suitable heating cycle via thermomechanical simulations, like the Gleeble machine, in which the test conditions can further go towards the real one in continuous casting. Interplay among three terms of temperature, strain, and strain rate during high-temperature thermomechanical processes brings an unpredictable mechanical behaviour which is directly accompanied by both structural hardening and softening mechanisms, *i.e.* increase in strain rate leads to harden the structure by raising up the number of dislocations, accumulating residual stress and strain, and activating dislocation sources and barriers *e.g.* Frank-Read source and Lomer-Cottrell junctions. However, higher temperatures facilitate thermally-activated softening phenomena such as DRV, DRX, and grain boundary sliding which make dislocations

mobile and rearrange them in more stabilized pattern. The strain value, on the other hand, has a reciprocal effect on mechanical behaviour of AHSSs relied on the competition between strain hardening and reduction in surface area during thermomechanical experiments.

To extrapolate data achieved by thermomechanical simulator apparatuses to a wide range of test temperatures and strain rates, researchers derived some numerical and mathematical equations, also called constitutive models, which are able to prognosticate the high-temperature mechanical behaviour (for both tension and compression) of metallic materials with different crystalline structures. Meanwhile, constitutive models let foundrymen to monitor any abrupt changes in thermomechanical trend of the material and the influence of alloying elements on hot deformation mechanism of steel products. Regarding the operating temperature, constitutive models have been categorized to medium-to-high (700-1200°C) and ultra-high (1200-1500°C) temperature intervals given in next sections.

2.3 Plastic Flow Modeling

Constitutive laws serve to comprehend the mechanisms which control plastic deformation of materials in extreme conditions when forming temperature, strain, and strain rate collaborate to generate both softening and hardening phenomena during deformation [44]. A combination of thermomechanical parameters yields microstructural evolution and subsequent changes in microstructure features at high temperature and strain rate, which affect the mechanical properties of the material *i.e.* the flow stress and ductility [45]. A comprehensive plasticity model for metals and alloys should be able to describe the dependency of the material behaviour on the various factors such as strain rate, forming temperature, strain history, and work hardening in both isotropic and anisotropic textures. Since the development of a model that can simultaneously interpret the interplay among different parameters is extremely difficult, some simplification are needed.

2.3.1 Medium-to-High Temperature Constitutive Models

Based on the origin of governing equations and the variables involved, constitutive flow models within the temperature range of 700-1200°C, can be categorized in one of the following groups [44]:

(1) Phenomenological models. The flow stress is defined based upon empirical observations later embedded within some mathematical functions. A reduction in the number of material constants makes these models easy to calibrate, however due to their empirical principles and lack of physical aspects of material, the applications are confined to those experimental conditions where the data was measured. Meanwhile, due to their limited flexibility which brings detailed formulation for determined materials, the data achieved by one specific metal or alloy cannot be generalizable to other metallic materials. Some of the most well-known models in this category are presented as Johnson-Cook (JC) [46], Khan-Huang (KH) [47], and Arrhenius equation [48, 49].

(2) Physically-based models. This category is founded on theories which explain a material's physical properties. In terms of the nature of the model, these theories include different aspects of thermodynamics, microstructural evolution, thermally-activated phenomena and slip kinetics [44]. Unlike the phenomenological model, these models can elucidate the constitutive behaviour of materials over a broad interval of loading conditions by means of physical assumptions, however, their large number of material constants is difficult being counted simultaneously.

(3) Artificial neural network (ANN) models. This method postulates neither regression analysis nor mathematical model to determine the response of the deformation behaviour at high temperatures which commonly shows non-linear trend [44]. ANN models are mostly hired to solve problems which are difficult to be solved via traditional computational methods. Due to their independency on physical insight or mathematical equations, ANN models are highly relied on reproducible experimental data. However, the performance of the ANN models strongly depends on the proper input parameters. Further, this category cannot be able to present definite expression for the hot deformation behaviour [50].

In one sense, all models can be categorized in the first group since they are ultimately evolved based on fitting on the empirical data achieved by experimental measurements. In the next part, the most common phenomenological and physically-based constitutive models have been reviewed.

2.3.1.1 Johnson-Cook (JC) Model

In 1983, Johnson and Cook [46] developed a phenomenological constitutive model for metals under the conditions in which a material is being subjected to high temperature, large strain and high strain rate. The principles of this reputed model have been founded on the integration of three various terms that illustrate the multiplication effects of strain hardening, strain rate hardening, and thermal softening caused by strain-annihilation phenomena such as DRV and DRX during high-temperature deformation. This model relies on the idea that the constitutive behaviour of an isotropic alloy at low temperature and strain rates can elucidate the flow stress at elevated temperatures associated with high strain rates. The JC model is favorable for engineering applications because of its simplicity and availability of parameters for different materials. In its original fashion, Equation 2.1, the JC model contains three terms; the work-hardening effect ($A + B\varepsilon^n$), the strain rate effect ($1 + C \ln \dot{\varepsilon}^*$), and the temperature effect ($1 - T^{*m}$) as,

$$\sigma = (A + B\varepsilon^n)(1 + C \ln \dot{\varepsilon}^*)(1 - T^{*m}); \quad \text{where} \quad T^* = \frac{T - T_r}{T_m - T_r} \quad , \quad (2.1)$$

in which, T , T^* , T_r , and T_m are the absolute, homologous, reference, and melting temperatures, $\dot{\varepsilon}$, and $\dot{\varepsilon}^*$ are absolute and reference strain rates, and A_{JC} , B_{JC} , and C_{JC} express the yield stress at a reference temperature and strain rate, the coefficient of strain hardening, and the coefficient of strain rate hardening, respectively. Also, n and m represent the strain rate hardening and thermal softening exponents. In the JC model, it has been assumed that thermal softening, strain hardening and strain rate hardening terms are independent. Zhang *et al.* [51] modified the original JC model regarding to the mutual dependency of forming temperature and strain hardening behaviour as,

$$\sigma = [A(1 - T^{*m}) + B(T^*)(\varepsilon^n)](1 + C \ln \dot{\varepsilon}^*) \quad , \quad (2.2)$$

where all the parameters are the same as those in Equation 2.1, except,

$$B(T^*) = \frac{\sigma_{br}(1 - T^{*m_1}) - \sigma_{0.2r}(1 - T^{*m})}{\left(\varepsilon_{br}[(1 + P_1)(T^* - P_2)(T^{*P_3})]\right)^n} . \quad (2.3)$$

In Equation 2.3, σ_f and ε_f represent the failure stress and strain at room temperature, σ_{ry} is the reference yield stress, and $(r_i, P_i, i = 1, 2, 3)$ are fitting coefficients.

Based on experimental evidence by Vural and Caro [52], further modification on the JC model showed that the B term in the JC model will drop faster than that predicted in the original JC model. In other words, the effect of thermal softening on strain hardening is stronger than yield stress. The dependency of the strain rate on the temperature at higher values, on the other hand, is unrealistically low in the original JC model due to uncoupled correlation between strain rate sensitivity and thermal softening effect. Therefore, they proposed the following JC terms relied on the transition between quasi-static to dynamic strain rate regime at high temperatures,

$$B = B_0[1 - (T^*)^P] \quad \text{and} \quad C = C_1(T^*_A)^P + C_2H(\dot{\varepsilon}, \dot{\varepsilon}_t, k) \quad , \quad (2.4)$$

$$T^*_A = \frac{T - T_0}{T_A - T_0} \quad \text{and} \quad H(\dot{\varepsilon}, \dot{\varepsilon}_t, k) = \frac{1}{(1 + e^{-2k \ln \dot{\varepsilon}/\dot{\varepsilon}_t})} . \quad (2.5)$$

Here, T_A is an ambient temperature, C_1 and C_2 are the rate sensitivity in the quasi-static strain rate regime at ambient temperature ($\dot{\varepsilon} < \dot{\varepsilon}_t$) and in the dynamic strain rate regime ($\dot{\varepsilon} > \dot{\varepsilon}_t$), $H(\dot{\varepsilon}, \dot{\varepsilon}_t, k)$ is the Heaviside step function continuously varied between 10^2 and 10^3 s^{-1} which is ascribed to the transitional strain rate and separates quasi-static from dynamic mode.

2.3.1.2 Khan-Huang (KH) Model

In 1992 [47], the KH empirical model was developed as a constitutive viscoplastic equation to simulate the stress behaviour of coarse-grain aluminum alloys. As seen in Equation 2.6, the uniaxial mean stress, or one-dimensional flow stress, basically contains two terms of $g_1(\varepsilon)$ and $g_2(\dot{\varepsilon})$, which represent the correlation of the stress versus the plastic strain, and strain rate dependent behaviour,

$$\sigma = g_1(\varepsilon)g_2(\dot{\varepsilon}) \quad , \quad (2.6)$$

$$\text{where } \begin{cases} g_1(\varepsilon) = \sigma_0 + E_\infty \varepsilon - ae^{-\alpha\varepsilon} \\ g_2(\dot{\varepsilon}) = \frac{1}{\left[1 - \frac{\ln(\dot{\varepsilon})}{\ln(D_0^P)}\right]^{n-1}} \end{cases},$$

in which, σ , ε , and $\dot{\varepsilon}$ stand for von Mises equivalent stress, the accumulated plastic strain, and equivalent plastic strain rate, respectively. Also, n , E_∞ , σ_0 , a , and α are material constants, while D_0^P , is invariant of the plastic deformation rate, and given a value of 10^6 s^{-1} in Khan and Huang's research [47, 53]. Although the first studies to verify this model were carried out on Face Centered Cubic (FCC) crystallographic structure, Khan and Liang also utilized the model to predict σ - ε behaviour for Body Centered Cubic (BCC) Tantalum, as shown in Figure 2.10 [54]. This new approach led to a modified constitutive model that predict the flow stress of both FCC and BCC structures at elevated temperatures. This model has been lately used in steels which show a wide range of these crystallographic structures at high temperatures [44, 45].

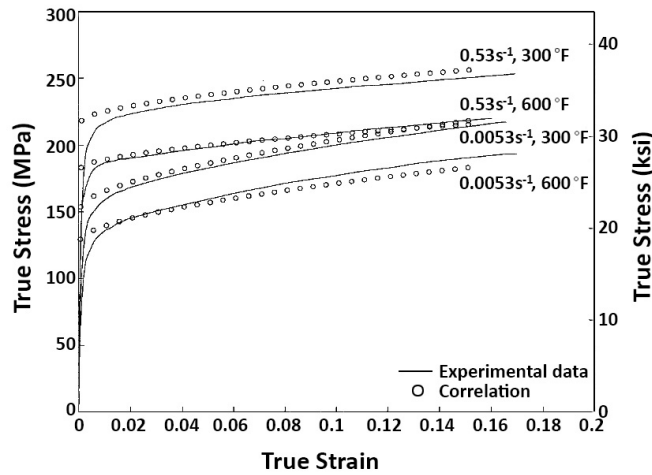


Figure 2.10: Stress-strain curves of Ta obtained by Khan-Liang model at different temperatures and strain rates [54]

There is a distinct difference between FCC and BCC structures in terms of hardening, strain rate and temperature dependency. The yield stress in the BCC structures shows strong dependency on the strain rate as well as temperature due to high Peierls-Nabarro friction stress, while the plastic strain hardening is almost an independent property which represents an athermal stress. The FCC structure, on the other hand, shows a strong dependence on the plastic strain because of the domination of

thermally activated mechanisms attributed to dislocations mobility. The shortcoming of the original KH model which was neglecting the temperature effect brought a new constitutive equation, Khan-Huang-Liang (KHL) model,

$$\sigma = [A + B(1 - \frac{\ln(\dot{\epsilon})}{\ln(D_0^P)})^{n_1}](1 - T^{*m})e^{c \ln \dot{\epsilon}}; \quad \text{where} \quad T^* = \frac{(T - T_r)}{(T_m - T_r)} \quad , \quad (2.7)$$

where, A , B , n_0 , n_1 , c , and m are material constants, while T , T_m , and T_r stand for the absolute, melting, and reference temperatures. In Figure 2.11, data by the KHL model demonstrate an excellent adaptation with experimental results, because coupling effect between strain and strain rate as well as the influence of temperature on thermal softening have been considered in the new KHL model [55].

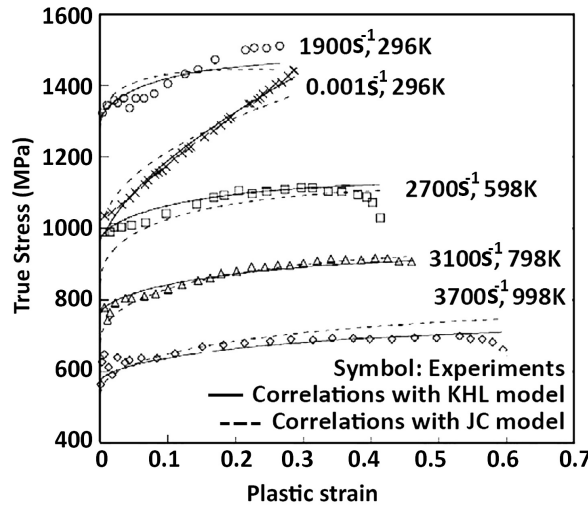


Figure 2.11: Comparison between KHL and JC models to measure both quasi-static and dynamic strain rates and temperatures [44]

2.3.1.3 Hollomon-Voce (HV) Model

The HV equation as the other famous phenomenological work hardening constitutive model includes three different functions of strain (f), strain rate (g), and temperature (h) as follows [45],

$$\sigma = \sigma(\epsilon, \dot{\epsilon}, T) = f(\epsilon, T)g(\dot{\epsilon})h(T) \quad , \quad (2.8)$$

in which, g and h can be chosen from any of several standard forms given in Table 2.2, while an incorporation between the temperature sensitivity of strain hardening

Table 2.2: Different functions proposed for strain rate sensitivity ($g(\dot{\varepsilon})$) and thermal softening ($h(T)$) [45]

<i>Strain Rate Sensitivity / $g(\dot{\varepsilon})$</i>	
Name	Equation
Power law model	$\sigma = \sigma_{\dot{\varepsilon}_0} \left(\frac{\dot{\varepsilon}}{\dot{\varepsilon}_0}\right)^m$
Johnson-Cook model	$\sigma = \sigma_{\dot{\varepsilon}_0} \left[1 + m \ln\left(\frac{\dot{\varepsilon}}{\dot{\varepsilon}_0}\right)\right]$
Wagoner model	$\sigma = \sigma_{\dot{\varepsilon}_0} \left(\frac{\dot{\varepsilon}}{\dot{\varepsilon}_0}\right)^{m_0} (\dot{\varepsilon} \cdot \dot{\varepsilon}_0)^{\frac{m_1}{2}}$
<i>Thermal Softening / $h(T)$</i>	
Name	Equation
Linear model	$h(T) = \sigma_{iso} (1 - \beta(T - T_r))$
Power law model I	$h(T) = \sigma_{iso} \left(\frac{T}{T_0}\right)^\beta$
Power law model II	$h(T) = \sigma_{iso} (a)^{\frac{T}{T_m}}$
Johnson-Cook model	$h(T) = \sigma_{iso} \left[1 - \left(\frac{T - T_0}{T_m - T_0}\right)^\beta\right]$
Khan model	$h(T) = \sigma_{iso} \left(\frac{T_m - T}{T_m - T_0}\right)^\beta$
Exponential model I	$h(T) = \sigma_{iso} \text{Exp}\left(\frac{A}{BT}\right)$
Exponential model II	$h(T) = \sigma_{iso} \text{Exp}\left(C \left(\frac{T - T_0}{T_m - T_0}\right)^m\right)$

rate that is calculated via a linear combination of Voce (stress saturation) [56, 57] and Hollomon (power-law) [58] strain hardening forms defines the f value. In spite of power-law models being typically used for the BCC metals at low homologous temperatures, the saturation-type model is commonly suitable for materials at higher homologous temperatures and the FCC metals at room temperature.

To derive the strain hardening function, $f(\varepsilon, T)$, studies on the effect of temperature on strain hardening curves in DP780 AHSS have been reported as the first motivation for the development of $f(\varepsilon, T)$ in its new style presented in Equation 2.9. As shown in Figure 2.12, the stress should be normalized by dividing to the yield stress at each temperature to illustrate better comparison between the trends of strain hardening curves [45]. As a result, the strain hardening function is represented based on the following form,

$$f(\varepsilon, T) = \alpha(T)f_H + (1 - \alpha(T))f_V \quad , \quad (2.9)$$

$$\text{where } \begin{cases} \alpha(T) = \alpha_1 - \alpha_2(T - T_0) \\ f_H = H_{HV} \cdot \varepsilon^{n_{HV}} \\ f_V = V_{HV}(1 - A_{HV} \cdot e^{-B_{HV} \cdot \varepsilon}) \end{cases},$$

where, T_0 is a reference temperature (usually 298K), and $\alpha_1, \alpha_2, H_{HV}, n_{HV}, A_{HV}$, and B_{HV} are material constants. In terms of the sign of α_1 , the HV model can be more Voce-like curve (stress saturation) at higher temperatures, and more Hollomon-like (power-law) at lower temperatures or vice versa. $\alpha(T) = 1$ leads the curve to be a pure Hollomon model, nevertheless, $\alpha(T) = 0$ brings a situation of pure Voce model.

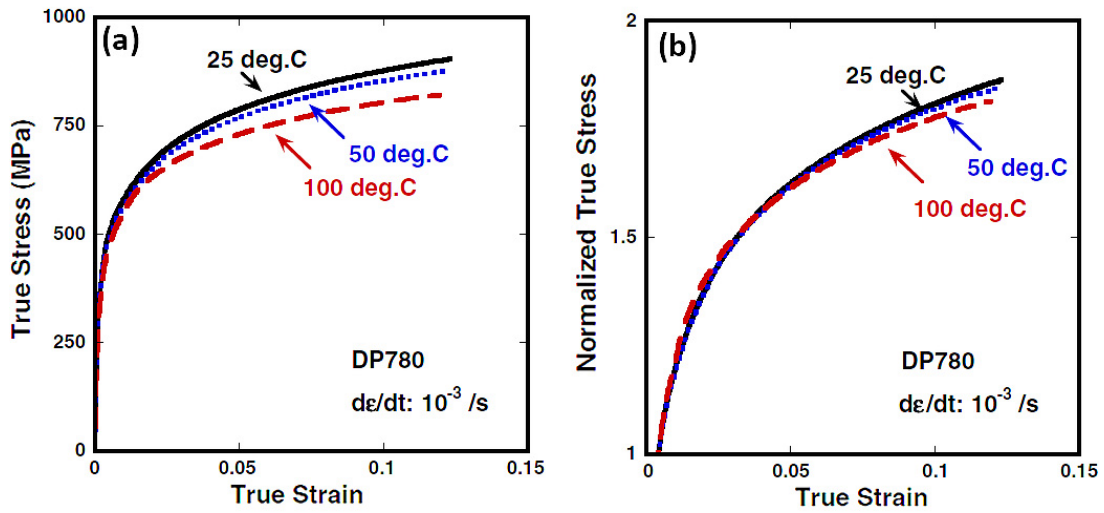


Figure 2.12: Stress-strain curves of DP780 at three temperatures: (a) experimental data, and (b) the normalized stress to reveal difference in strain hardening rates [45]

2.3.1.4 Rusinek-Klepaczko (RK) Model

In 2001, the RK model was developed based upon a physical viscoplastic constitutive model for sheet metals tested with a wide range of strain rates [59]. In the original RK model, three terms, the strain hardening, the strain-rate sensitivity, and temperature effects, are taken into account to define a model based on the theory of additive decomposition in the total stress [60, 61]. In this case, the stress has been considered as an addition of two terms σ_μ and σ^* , respectively referred to the internal stress caused by strain hardening and the effective stress brought by thermally-induced

activation processes. In Equation 2.10, the term $\frac{E(T)}{E_0}$ as multiplicative factor of the stress addition defines the elastic modulus evolution with temperature [62],

$$\bar{\sigma}(\bar{\varepsilon}^P, \dot{\varepsilon}^P, T) = \left(\frac{E(T)}{E_0}\right) [\sigma_\mu(\bar{\varepsilon}^P, \dot{\varepsilon}^P, T) + \sigma^*(\dot{\varepsilon}^P, T)] \quad , \quad (2.10)$$

$$E(T) = E_0 \left(1 - \frac{T}{T_m} \text{Exp}[\theta^* (1 - \frac{T_m}{T})]\right) \quad , \quad (2.11)$$

here, E_0 , T_m , and θ^* denote the elastic modulus at $T=0\text{K}$, melting temperature, and characteristic homologous temperature, respectively. Two terms of internal and effective stresses are obtained using following equations,

$$\bar{\sigma}_\mu(\bar{\varepsilon}^P, \dot{\varepsilon}^P, T) = B(\dot{\varepsilon}^P, T) (\varepsilon_0 + \bar{\varepsilon}^P)^{n(\dot{\varepsilon}^P, T)} \quad , \quad (2.12)$$

$$\text{where} \quad \begin{cases} B(\dot{\varepsilon}^P, T) = B_0 \left(\left(\frac{T}{T_m}\right) \log\left(\frac{\dot{\varepsilon}_{max}}{\dot{\varepsilon}^P}\right)\right)^{-\nu} \\ n(\dot{\varepsilon}^P, T) = n_0 \left(1 - D_2 \left(\frac{T}{T_m}\right) \log\left(\frac{\dot{\varepsilon}^P}{\dot{\varepsilon}_{min}}\right)\right) \end{cases} \quad ,$$

$$\sigma^*(\dot{\varepsilon}^P, T) = \sigma_0^* \left(1 - D_1 \left(\frac{T}{T_m}\right) \log\left(\frac{\dot{\varepsilon}_{max}}{\dot{\varepsilon}^P}\right)\right)^{m^*} \quad , \quad (2.13)$$

where, B_0 , D_1 , and D_2 are material constant, ν the temperature sensitivity, n_0 the strain hardening exponent at $T=0\text{K}$, and $\dot{\varepsilon}_{min}$ is the lower limit of the model, while $\dot{\varepsilon}_{max}$ and m^* are the maximum strain rate accepted for a particular material, and material constant shows temperature dependency of the strain rate [63]. It has been shown that the original RK model has some problematic aspects on thermo-viscoplastic behaviour of the FCC structures like aluminum alloys.

In other study, Rusinek and Rodriguez-Martinez [64], represented two extensions to the RK model describing the macroscopic negative strain rate sensitivity (NSRS) shown by the equivalent Huber-Mises stress, σ_{ns} , and the viscous drag taking place in some FCC metals when subjected to higher deformation rate, σ_{ath} , as shown below,

$$\bar{\sigma}(\bar{\varepsilon}^P, \dot{\varepsilon}^P, T) = \left(\frac{E(T)}{E_0}\right) [\sigma_\mu(\bar{\varepsilon}^P, \dot{\varepsilon}^P, T) + \sigma^*(\dot{\varepsilon}^P, T) + \sigma_{ns}(\dot{\varepsilon}^P, T)] \quad , \quad (2.14)$$

$$\bar{\sigma}(\bar{\varepsilon}^P, \dot{\varepsilon}^P, T) = \left(\frac{E(T)}{E_0}\right) [\sigma_\mu(\bar{\varepsilon}^P, \dot{\varepsilon}^P, T) + \sigma^*(\dot{\varepsilon}^P, T)] + \sigma_{ath}(\dot{\varepsilon}^P) \quad , \quad (2.15)$$

$$\text{in which } \begin{cases} \sigma_{ns}(\dot{\epsilon}^P, T) = \sigma_0^{ns} \cdot \log\left(\frac{\dot{\epsilon}_{trans}}{\dot{\epsilon}^P}\right) \cdot \left(1 - D_3\left(\frac{T_m}{T}\right) \cdot \log\left(\frac{\dot{\epsilon}^P}{\dot{\epsilon}_{max}}\right)\right) \\ \sigma_{ath}(\dot{\epsilon}^P) = \chi[1 - \text{Exp}(-\alpha \cdot \dot{\epsilon}^P)]; \quad \text{where } \alpha = \left(\frac{M^2 B}{\rho_m b^2 \tau_y}\right) \end{cases},$$

in which, σ_0^{ns} , and D_3 are material constants expressing the stress reduction during dynamic strain aging (DSA) as well as the reciprocity between strain rate and temperature variation. Also, $\dot{\epsilon}_{trans}$ obtained by experiments shows the transition between positive and NSRS. M , B , b , and ρ_m are the Taylor factor, the drag coefficient, the magnitude of the Burgers vector, and the mobile dislocation density, while χ , α , and τ_y stand for a material constant, an effective damping coefficient bringing the dislocation mobility, and high-temperature yield stress.

Figure 2.13 reveals the comparison between the analytical predictions of the original RK model and those corresponding to extended forms [64]. As shown, the viscous-drag component in the extended RK model provides better convergence to experimental data particularly at high deformation rates. Also, for the AA7075 alloy, an increase in dynamic strain rate causes higher stress values in experimental data which can be better shown in extended RK model rather than the original one. The AA5083 alloy, on the other hand, does not show a remarkable difference in stress-strain behaviour at higher quasi-static strain rates. The reason maybe comes from the fact that 5xxx series of aluminum alloys are not heat-treatable, and the only hardening mechanism will be work hardening during deformation which is not significantly changed by increase in quasi-static strain rate. However, precipitation strengthening, which is dramatically affected by strain rate, will have synergistic effect on work hardening in the AA7075 alloy.

2.3.1.5 Zerilli-Armstrong (ZA) Model

In 1987, the ZA physical model was suggested. This model relies on a dislocation mechanism concept which is closely related to thermal activation analysis and considering the strain rate and temperature dependency in a coupled manner [65]. The model was developed for both BCC and FCC structures, however, the difference in dislocation characteristics for each structure led to different governing constitutive equations for each case. The strain-hardening dependency of the yield stress is intrinsically high in FCC metals, while main factors affecting the yield stress in BCC metals

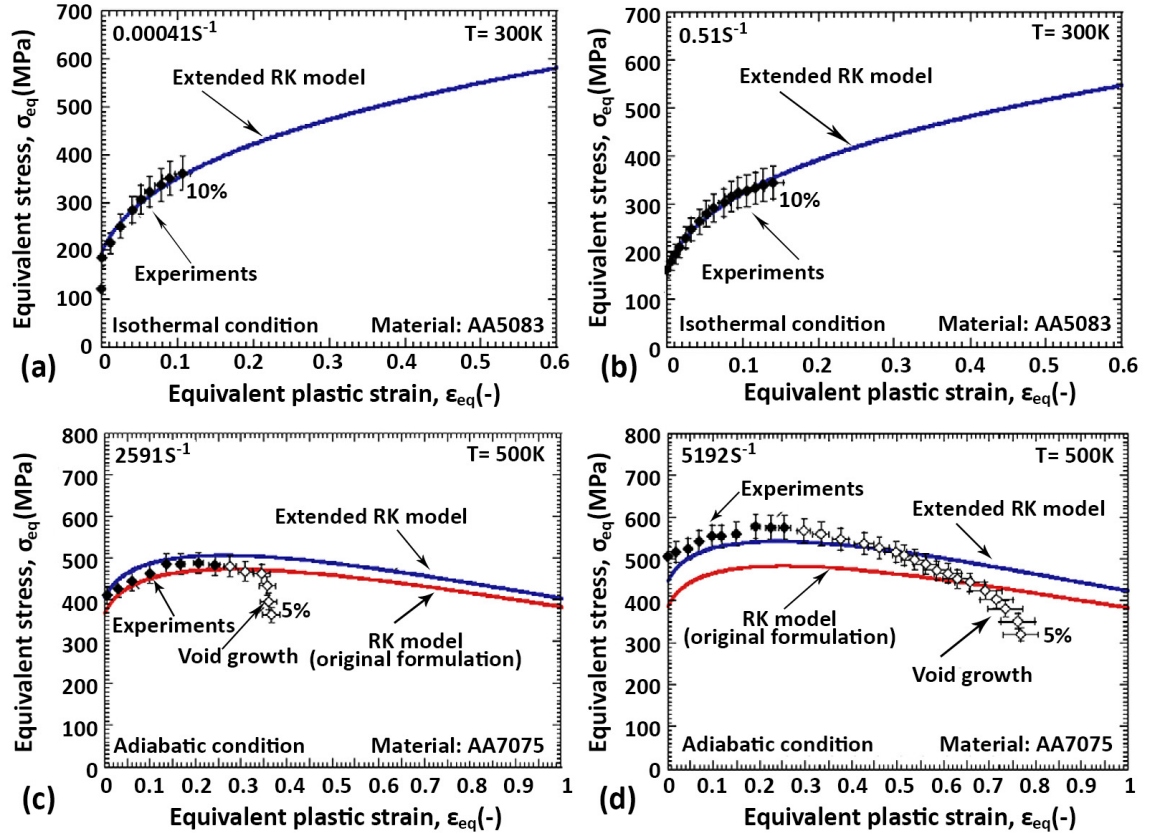


Figure 2.13: Effect of temperature and strain rate in quasi- and dynamic conditions on stress-strain curves obtained by the RK and its extended models [64]

are temperature and strain rate due to sharp variation in the Peierls-Nabarro stress associated by changes in temperature or strain rate. The ZA model considers the main mechanism of hardening in FCC metals, which is cutting the dislocation forests as well as that happening in BCC metals assigned to overcoming the Peierls-Nabarro stress. This model, founded based on experimental results, is given as [44, 66]:

$$\sigma = \sigma_{ath} + \sigma_{th} \quad , \quad \text{and} \quad (2.16)$$

$$\sigma_{th} = \frac{M\Delta G_0 e^{-\beta T}}{Ab}; \quad \text{where} \quad \beta = -C_3 + C_4 \ln \dot{\epsilon} \quad . \quad (2.17)$$

In equations 2.16 and 2.17,

$$\begin{cases} \text{For BCC materials: } \sigma_{th} = C_1 \text{Exp}(-C_3 T + C_4 T \ln \dot{\epsilon}) \\ \text{For FCC materials: } \sigma_{th} = C_2 \epsilon^{0.5} \text{Exp}(-C_3 T + C_4 T \ln \dot{\epsilon}) \end{cases} \quad , \quad (2.18)$$

σ_{ath} and σ_{th} are referred to the athermal and thermal flow stresses, and $C_i, i = 1, \dots, 4$ are material constants. Also, $M, \Delta G_0, A, b,$ and β are the direction factor, Gibbs free energy of thermal activation at 0K, activation surface area at 0K, the Burgers vector, and a parameter associates with strain and strain rate. The fact that parameters which have been considered constant in the ZA model actually change at various conditions during the actual process, necessitates further development in the original ZA equations.

To this, Zhang *et al.*, [67] developed a modified ZA model regarding the integrated effects of temperature, strain rate, and deformation process over a wide interval of temperatures and strain rates on the flow stress of IC10 alloy, as expressed by,

$$\begin{cases} \text{For BCC materials: } \sigma = C_0 + C_1 \text{Exp} \left[\left(-C''_3 T + C'_4 T \ln \left(\frac{\dot{\varepsilon}}{r(\varepsilon)r(\dot{\varepsilon})} \right) \right) f(T) \right] + C_5 \varepsilon^n \\ \text{For FCC materials: } \sigma = C_0 + C_2 \varepsilon^{0.5} \text{Exp} \left[\left(-C''_3 T + C'_4 T \ln \left(\frac{\dot{\varepsilon}}{r(\varepsilon)r(\dot{\varepsilon})} \right) \right) f(T) \right] \end{cases}$$

$$\text{where, } r(\varepsilon) = \rho_0 + M\varepsilon \quad ,$$

where, ρ_0 is the initial dislocation density, and M is a material constant varying with increase in dislocation density. Parameters $C_0, C_1, C_2, C_5, C''_3, C'_4,$ and n in both BCC and FCC materials can be identified via the least square method applied on a reference stress-strain curve. Also, $r(\dot{\varepsilon})$ and $f(T)$ functions at different situations and crystallographic structures can be derived as,

(1) $T = T_r, \varepsilon \neq \dot{\varepsilon}_r,$ then $f(T) = 1$:

$$\begin{cases} \text{For BCC materials: } r(\dot{\varepsilon}) = \frac{\dot{\varepsilon}}{\dot{\varepsilon}_r} \times \text{Exp} \left[\frac{\ln \left[\frac{(\sigma_{Pr} - C_0 - C_5(\varepsilon_P)^n)}{(\sigma_Q - C_0 - C_5(\varepsilon_Q)^n)} \right]}{C'_4 T} \right] \\ \text{For FCC materials: } r(\dot{\varepsilon}) = \frac{\dot{\varepsilon}}{\dot{\varepsilon}_r} \times \text{Exp} \left[\frac{\ln \left[\frac{(\sigma_{Pr} - C_0)}{(\sigma_Q - C_0)} \right]}{C'_4 T} \right] \end{cases} ,$$

(2) $T \neq T_r, \varepsilon = \dot{\varepsilon}_r,$ then $r(\dot{\varepsilon}) = 1$:

$$\begin{cases} \text{For BCC materials: } f(T) = \frac{T_r}{T} \times \text{Exp} \left[\frac{\ln \left[\frac{(\sigma_Q - C_0 - C_5(\varepsilon_Q)^n)}{C_1} \right]}{\ln \left[\frac{(\sigma_{Pr} - C_0 - C_5(\varepsilon_P)^n)}{C_1} \right]} \right] \\ \text{For FCC materials: } f(T) = \frac{T_r}{T} \times \text{Exp} \left[\frac{\ln \left[\frac{(\sigma_Q - C_0)}{C_2 \varepsilon^{0.5}} \right]}{\ln \left[\frac{(\sigma_{Pr} - C_0)}{C_2 \varepsilon^{0.5}} \right]} \right] \end{cases} .$$

$$\text{so, } \begin{cases} \sigma_{Pr} = C_0 + C_2 \varepsilon_{Pr}^{0.5} \text{Exp} \left[\left(-C''_3 T_r + C'_4 T_r \ln \left(\frac{\dot{\varepsilon}_r}{r(\varepsilon_{Pr})r(\dot{\varepsilon}_r)} \right) \right) f(T)_r \right] \\ \sigma_Q = C_0 + C_2 \varepsilon_Q^{0.5} \text{Exp} \left[\left(-C''_3 T_r + C'_4 T \ln \left(\frac{\dot{\varepsilon}}{r(\varepsilon_Q)r(\dot{\varepsilon})} \right) \right) f(T) \right] \end{cases} \quad (2.19)$$

in which, σ_{Pr} and σ_Q are respectively referred to the stresses of a random points P and Q on the reference, and different stress-strain curves. As seen in Figure 2.14, the modified ZA model shows a better fit to experimental data rather than the original one [48, 67].

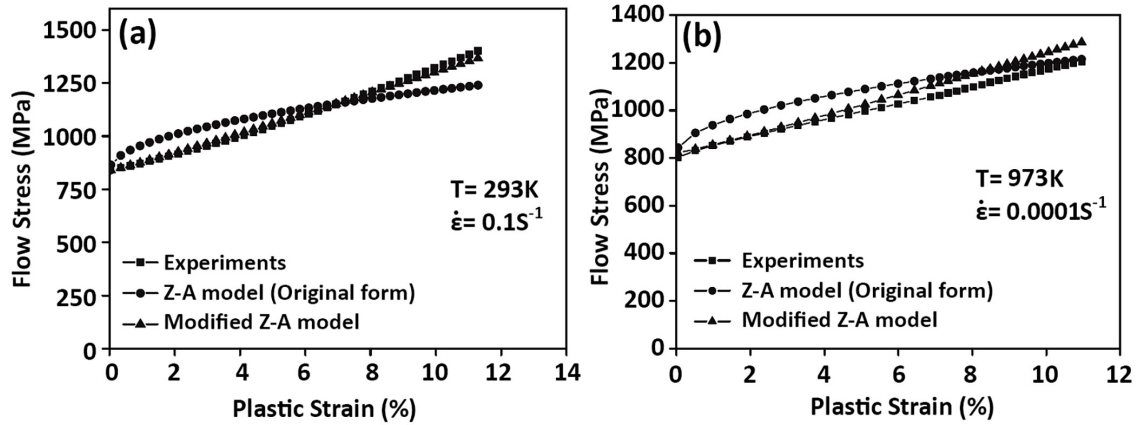


Figure 2.14: Comparison between original and modified ZA models performed to measure the flow stress of IC10 alloy at various temperatures and strain rates [67]

2.3.2 Constitutive Behaviour of DP AHSS

Within the most recent efforts being done on evaluation of constitutive behaviour of AHSSs, two modified JC and HV models have been successfully conducted on various grades of DP AHSS. Yu *et al.* [68], employed both quasi-static and dynamic tensile tests at ambient temperature and strain rates between 10^{-4} to 1600s^{-1} on sheet of DP600 alloy to observe the strain-rate-dependent plastic flow behaviour via the JC model modified by the KH equation. As seen in Figure 2.15, it has been shown that by increasing the strain rate, the stress value at the same strain becomes greater, and meanwhile two-fold increase in the initial yield stress is obvious in samples subjected to 500 to 1600s^{-1} strain rates.

Furthermore, despite the unnoticeable yield stress at low strain rates, samples tested at higher values show an obvious upper-lower yield phenomenon. Stress versus di-

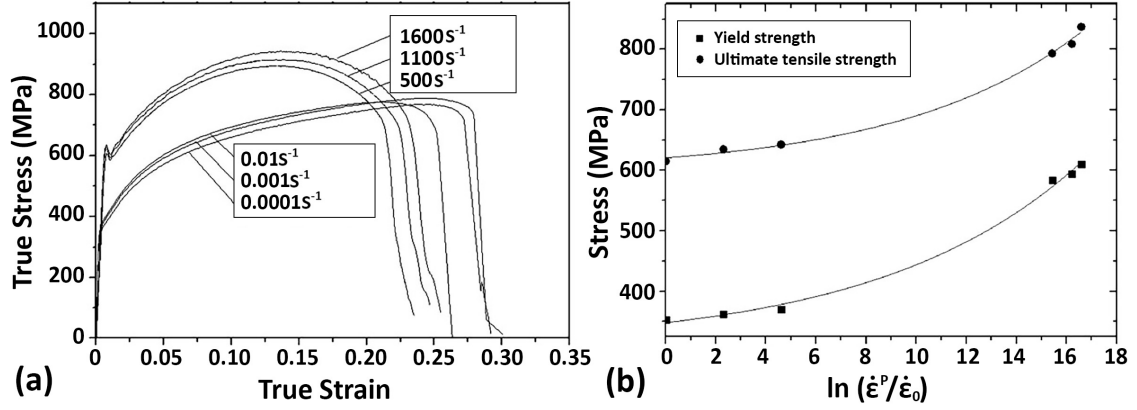


Figure 2.15: Comparison of the flow stress, ultimate and yield tensile strength at various strain rates [68]

mensionless equivalent plastic strain rate (obtained by the equivalent plastic rate over a reference plastic strain rate $10^{-4} s^{-1}$) for both yield and ultimate tensile stresses elucidates non-linear trend formulated as,

$$f(\dot{\epsilon}^P) = A + B e^{n \ln(\frac{\dot{\epsilon}^P}{\dot{\epsilon}_0})} \quad , \quad (2.20)$$

in which, A , B , and n are material constants.

As an assumption, if the temperature dependency of the flow stress can be considered negligible, adding the exponential term proposed by Khan and Huang [47], as well as strain-rate-dependent function, $f(\dot{\epsilon}^P)$, modified the JC model as the following style,

$$\sigma = A \left(1 + D \left(\ln \frac{\dot{\epsilon}^P}{\dot{\epsilon}_0} \right)^m \right) + B (\epsilon^P)^n - a e^{-\alpha \epsilon^P} \quad , \quad (2.21)$$

$$f_1(\dot{\epsilon}^P) = 1 + D \left(\ln \frac{\dot{\epsilon}^P}{\dot{\epsilon}_0} \right)^m \quad . \quad (2.22)$$

where, the quantity of variations in DP600 AHSS is given in Table 2.3. As seen in Figure 2.16, the curve achieved by the developed model is in good accordance with the experimental data at each strain rate.

Table 2.3: Values of the JC model's terms used in DP600 AHSS [68]

<i>JC Model's Values</i>						
A (MPa)	B (MPa)	n	a	α	D	m
352.72	635.5	0.2868	122.6	20.17	0.01448	1.396

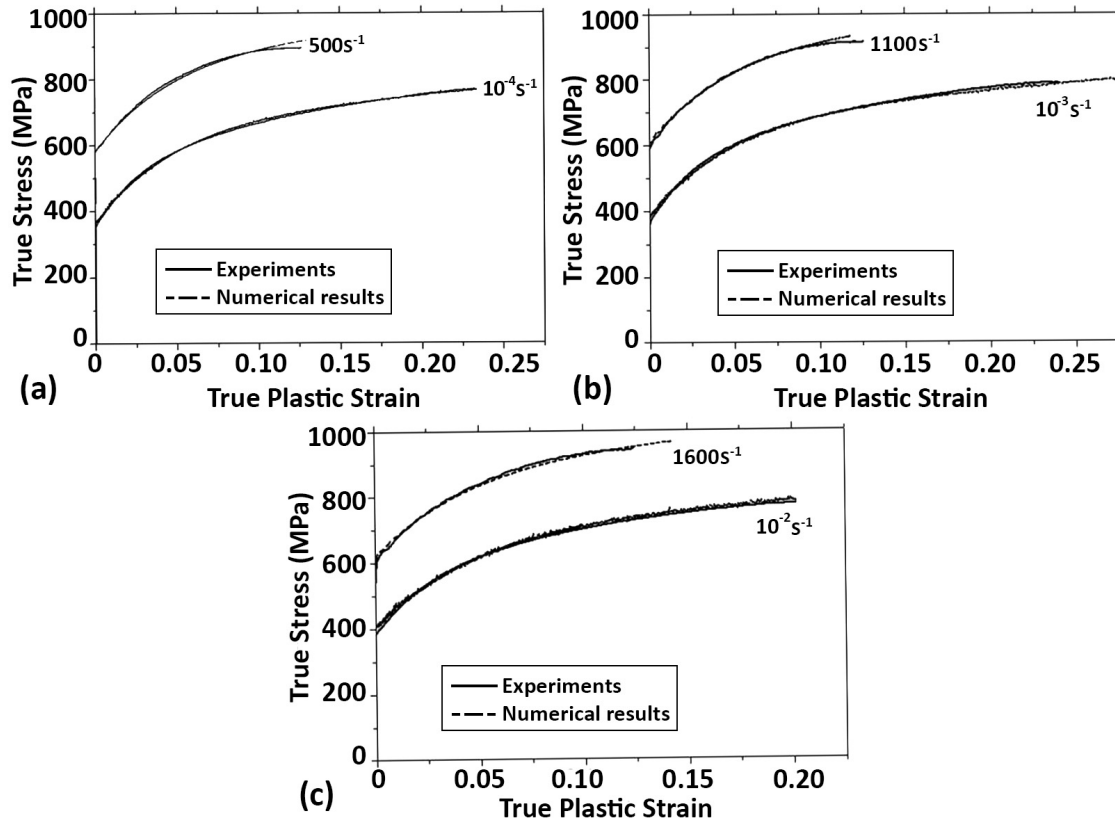


Figure 2.16: The response of stress-strain curves to variation of the strain rate between quasi- to dynamic values via the JC model in DP600 AHSS [68]

In another study, Sung *et al.* [45], investigated the constitutive mechanical behaviour of DP590 (as-received), DP780 (hot-dipped galvanized coated – HDGI), and DP980 (hot-dipped galvanneal coated – HDGA) alloys at three isothermal temperatures via the HV model. For all steels, the strain rate sensitivity index, m , has a strong dependency on the strain rate, so the power-law and JC rate law models cannot be used in their unmodified styles. The linearized Wagoner rate law in the Equation 2.23 [69] presents a good consistency between numerical and experimental data, as shown in Figure 2.17.

$$\sigma = \sigma_{\dot{\epsilon}_0} \left(\frac{\dot{\epsilon}}{\dot{\epsilon}_0} \right)^{\gamma_2 + (0.5\gamma_1) \log(\dot{\epsilon} \times \dot{\epsilon}_0)}, \quad (2.23)$$

in which, $\sigma_{\dot{\epsilon}_0}$ is a stress corresponding to $\dot{\epsilon}_0$, and γ_1 and γ_2 are material constants. According to Equation 2.24, the HV optimal coefficient includes α_1 , α_2 , H_{HV} , n_{HV} , V_{HV} , A_{HV} , B_{HV} , and β can be determined based on the linear model for the thermal softening function, $h(T)$, and the results obtained by the tensile test at various temperatures. The HV model's best-fit coefficients and the standard deviation from experimental data plotted in Figure 2.18, are given in Table 2.4.

$$f(\epsilon, T)h(T) = [\alpha(T)(H_{HV}\epsilon^{n_{HV}}) + (1 - \alpha(T))V_{HV}(1 - A_{HV}e^{-B_{HV}\epsilon})][1 - \beta(T - T_0)] \quad (2.24)$$

$$\text{where } \begin{cases} h(T) = \sigma_{iso}(1 - \beta(T - T_r)) \\ \alpha(T) = \alpha_1 - \alpha_2(T - T_0) \end{cases}$$

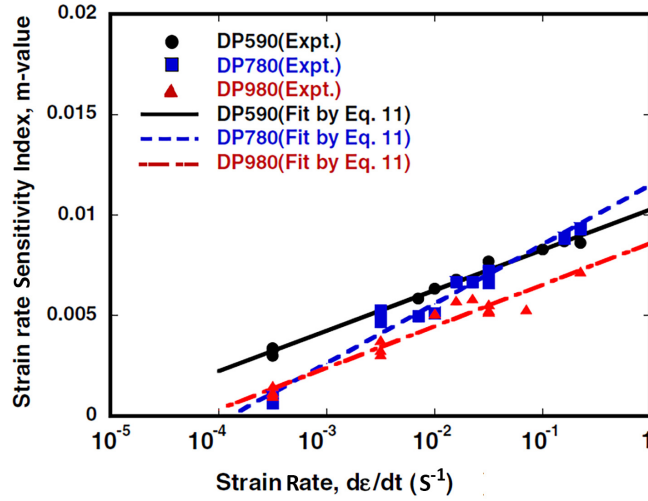


Figure 2.17: Measured strain rate sensitivity, m , for different grades of DP AHSS plotted by linearized Wagoner rate law [45, 69]

Table 2.4: γ values and the HV model's coefficients in various DP AHSSs [45]

	<i>Target Alloy</i>		
	DP590	DP780	DP980
γ_1	0.0020	0.0030	0.0021
γ_2	0.0103	0.0115	0.0086
H_{HV}	1051	1655	1722
n_{HV}	0.179	0.213	0.154
V_{HV}	643.9	752.1	908.1
A_{HV}	0.576	0.265	0.376
B_{HV}	22.44	30.31	39.64
α_1	0.818	0.507	0.586
α_2	0.00193	0.00187	0.00149
β	2.7×10^{-4}	5.8×10^{-4}	3.9×10^{-4}
R^2	0.999	0.998	0.999
S.D	0.5	2.5	0.6

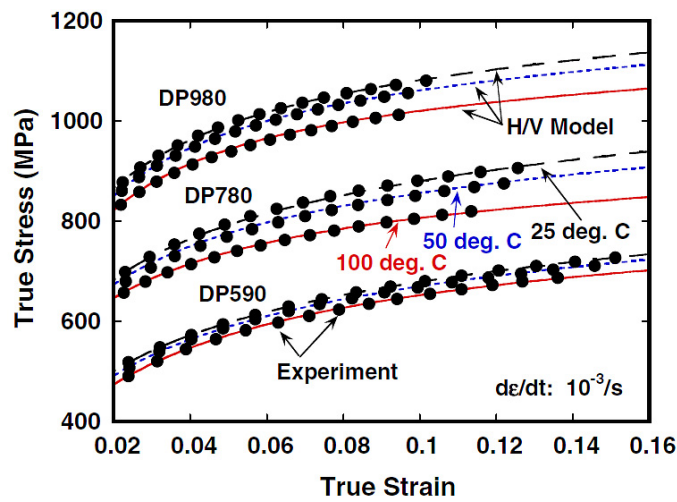


Figure 2.18: Comparison between the best-fit HV model and isothermal tensile test data for three grades of DP AHSS [45]

2.3.3 Ultra-High Temperature Constitutive Models

The story behind dominant mechanisms which interpret the ultra-high-temperature (1200-1500°C) thermomechanical behaviour of steels is totally different from those already explained at lower test temperatures. Notwithstanding the short-range diffusion of atoms during softening phenomena at medium-to-high temperatures, long-range diffusion paths activated at ultra-high temperatures are mainly responsible for mass diffusion of atoms, and subsequently, the grain boundary sliding and abnormal grain growth. From hardening aspect of view, most crystalline barriers against dislocations mobility which cause strain hardening will be no longer active at ultra-high temperatures due to mass diffusion and annihilation mechanism of structural imperfections. However, the strain can be intermittently localized adjacent to those rare dislocation barriers, like high-temperature carbides, and make the flow stress curve in wavy or hyperbolic mode. Apart from that, grain growth of γ phase or phase transformation of γ to δ phase for those steel grades with low peritectic reaction put the other problematic issue into mathematical models developed to predict the thermomechanical behaviour of the material at 1000-1300°C. In terms of complicated interaction between softening and hardening mechanisms within the mentioned temperature interval, there have been less reports on how to conduct constitutive models which can be valid at various temperatures and strain rates. Among those efforts, two most acceptable models by Garofalo [70] and Han *et al.* [71] have been further discussed in the following sections.

2.3.3.1 Garofalo Model

Regarding limitations of power-law equations at low stresses/strain rates and exponential relationship at high stresses/strain rates, Garofalo [70] developed a sine-hyperbolic equation with Arrhenius term to successfully correlate stress dependence for the entire stress regime. As shown in Equation 2.25, this model is basically developed for creep-assisted deformation relying on strain dependency of plastic flow under transient and steady-state conditions.

$$\dot{\epsilon} = A_{\epsilon} \cdot [\sinh(\alpha_{\epsilon} \sigma)]^{n_{\epsilon}} \cdot \text{Exp}\left(\frac{-Q_{\epsilon}}{RT}\right); \quad \text{where } n_{\epsilon} = \frac{1}{m}, \quad (2.25)$$

A_ε , α_ε , and n_ε are strain-dependent parameters, while Q_ε and m are apparent activation energy and strain-rate sensitivity, respectively. The Garofalo model is valid for the entire strain rates/stress regime at those temperatures in which creep phenomenon will be dominant.

McQueen and Ryan [72] showed the correlation between all terms in Equation 2.25 for three grades of austenitic stainless steels. As revealed in Figure 2.19, once the flow stress and the strain rate increase at high temperature, higher rate of strain hardening, θ , accompanied by nucleation and growth of subgrains is expected. As a result, rise in critical stress for DRX and saturation stress, *i.e.* plastic deformation accommodated by nucleation of maximum number of persistent slip bands (PSBs) [73], shift the stress-strain curve to higher stress values. At ultra-high temperatures in steel processing ($> 1200^\circ\text{C}$), the DRX softening mechanism no longer exists, however, the structure experiences strain hardening before stress saturation.

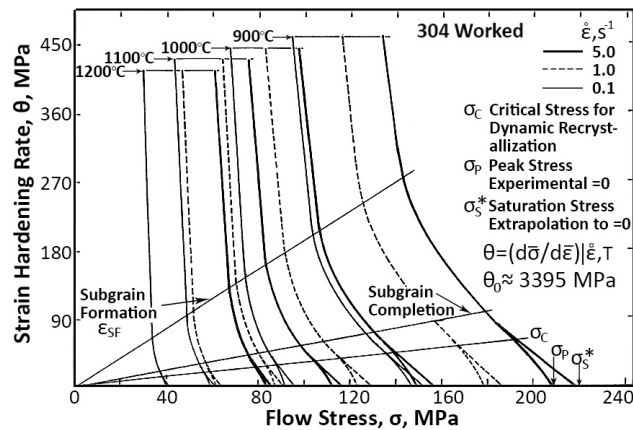


Figure 2.19: Torsion stress-strain curves of 301W stainless steel at different working temperatures [72]

2.3.3.2 Han Model

In 1996, Han *et al.* [71] developed a modified version of Garofalo model which was also able to predict constitutive thermomechanical behaviour of porous materials. As shown in Equation 2.26, the effective plastic strain rate has been directly correlated with those terms in Garofalo model as well as the strength coefficient, K . This equation also confirms the fact shows that the material will be subjected to strain hardening phenomenon even at ultra-high temperatures.

$$\dot{\varepsilon} = A_{\varepsilon} [\sinh(\beta K)]^{n_{\varepsilon}} \cdot \text{Exp}\left(\frac{-Q_{\varepsilon}}{RT}\right); \quad \text{where} \quad K = \frac{\sigma}{(\varepsilon_0 + \varepsilon)^n} \quad , \quad (2.26)$$

In this equation, n and β stand for the strain-hardening exponent and material constant. Also, ε_0 and ε in K equation are referred to the initial strain by prior cold working and sum of elastic and homogeneous plastic strains stored right before stress saturation. For porous materials, there has been a modification in $\dot{\varepsilon}$ value as follows:

$$\dot{\varepsilon} = \left(\frac{\eta^{0.5}}{R}\right) \dot{\varepsilon}_P; \quad \text{where} \quad \eta = \frac{(\sigma_{0,P})^2}{\sigma_0^2} \quad , \quad (2.27)$$

where, $\dot{\varepsilon}_P$, $\sigma_{0,P}$, and σ_0 are plastic strain and yield strength of porous material, and yields strength of sound material, respectively.

2.4 Summary

To sum up, the continuous casting process of the AHSSs is considered as an important sector of the steel processing which imposes a great deal of cost to the automotive and construction industries. Nowadays, the cost issue becomes more problematic because the AHSSs containing a bunch of costly constitutive elements are being utilized in most parts of vehicles due to their suitable mechanical properties. Therefore, a well-evaluated setup which satisfies both product quality and process reliability is prerequisite before further operations. In spite of all efforts focusing on how to ameliorate the steel products quality, AHSSs show an undeniable drop in high-temperature mechanical properties which brings many problems during hot working.

To rectify the hot embrittlement in steels, most research are carried out in the temperature range of 700-1200°C by performing high-temperature experimental observations and analytical interpretation of data via constitutive mathematical models. The lack of experimental investigations at temperatures which are higher than those formerly conducted should be taken into account to assess the effect of the other parameters *e.g.* grain size of primary austenite, volume change during the peritectic reaction, volume fraction of porosities, and presence of low-melting temperature phases affecting wettability of austenite GBs and shear strength of material within 1200-1500°C.

Chapter 3

Scope and Objectives

As shown in the literature review, considerable hot ductility measurements have been made over the temperature range of 700-1200°C, while there is a lack of data at higher temperatures, 1200-1500°C. The importance of the ultra-high temperature range should be considered due to a complicated interplay between thermally-activated characteristics that will be no longer activate at lower temperatures. For instance, grain boundary sliding, dislocations annihilation, creep-assisted straining, the peritectic reaction followed by volume change in structure, and the presence of low-melting temperature phases are among those parameters that directly affect the deformation of AHSSs at ultra-high temperatures. Microstructural defects like gas and shrinkage porosities, on the other hand, are always well understood as the other detrimental features cause the structure vulnerable to failure by stress localization during deformation. To minimize the effect of porosity on constitutive behaviour of AHSSs, choosing the transfer-bar material that is less prone to presence of the voids and porosities is favorable. The goal of this research is to acquire thermomechanical data at ultra-high temperatures, and in order to better understand high temperature embrittlement. In consultation with the industrial sponsor, ArcelorMittal-Dofasco, the first generation AHSS of DP600 will be studied.

The objectives of this study are thus:

- To quantify the thermomechanical behaviour of DP600 alloy.
- Comparing and contrast in ultra-high temperature mechanical properties between transfer-bar and as-cast microstructures.

- Determining the suitable geometry for thermomechanical tensile test.

For this purpose, the Gleeble thermomechanical simulator is utilized to conduct tensile test on samples prepared with three different geometries. The Gleeble input thermomechanical schedule is designed in such a way that the effect of test temperature on the stress-strain curve can be analyzed. To assess the role of porosity on high-temperature mechanical properties, transfer-bar samples are put through the Gleeble tensile test, as well. As experimental results, maximum tensile stress and RA percentage are measured as two important values determining the toughness of each sample at high temperature. Moreover, microscopy and fractography analysis on as-received microstructures and fracture surface of tensile tests allow to understand the effect of microstructural features on strength and hot ductility of DP600 AHSS as well as the mode of failure. It is worth mentioning that all samples have been collected from the surface of DP600 continuously-cast slab, where the maximum cooling rate during the process results in the highest susceptibility to microstructural defects like segregation, porosity formation, and crack nucleation and propagation.

Chapter 4

Experimental Methodology

To investigate the high-temperature constitutive behaviour of DP600 AHSS, two sets of transfer-bar and as-cast samples were subjected to high-temperature thermomechanical tensile test using the Gleeble apparatus. Differential scanning calorimetry (DSC) was successfully conducted on samples to design the suitable thermomechanical cycles based upon thermal properties of the target alloy. In the following, details of the experiments that were conducted in this study are explained.

4.1 Material

The as-received product of DP600 AHSS, with a chemical composition given in Table 4.1, was provided by ArcelorMittal, Dofasco. The material was collected from the surface of continuously-cast slab in both as-cast and transfer-bar conditions, in other words, right before and after the rough rolling process. The reason behind choosing the surface of slab refers back to the fact that most of continuous casting solid-state defects *e.g.* oscillation marks and surface deflections nucleate and propagate beneath the surface due to maximum thermal shock by high cooling rate, and severe tension applied by the slab's central regions which will be later exposed to solidification and phase transformation phenomena. Besides from that, although the number and size of α -ferrite grains do not influence the ultra high-temperature thermomechanical behaviour of steels, the transfer-bar microstructure was deliberately chosen as well to assess the effect of porosity fraction and distribution of low-melting phases on high-temperature mechanical behaviour of the studying material.

Table 4.1: Chemical composition of DP600 steel, wt%

<i>C</i>	<i>Mn</i>	<i>Si</i>	<i>Cr</i>	<i>Mo</i>	<i>Ti</i>	<i>S</i>	<i>P</i>	<i>Al</i>	<i>B</i>	<i>Ca</i>
0.1	1.54	0.18	0.19	0.22	0.02	0.002	0.01	0.05	0.0002	0.0034

As will be discussed in next chapter, the microstructure of the transfer-bar samples will show an anisotropic texture elongated towards the rolling direction. Since the low-melting intermetallic compounds are formed alongside the GBs, rough-rolled steel product provides an even distribution of these phases as well as inclusions which were randomly dispersed in the as-cast morphology. Meanwhile, compression loading during rough rolling will close a large portion of porosities already generated by entrapped gas bubbles or shrinkage during the solidification.

4.2 High-temperature Tensile Testing

A Gleeble₃₅₀₀ thermomechanical simulator was utilized to perform all hot tensile tests. The Gleeble₃₅₀₀ as a popular apparatus to investigate high-temperature mechanical properties is fully integrated, digital closed loop controlled, physical and thermomechanical simulator. As depicted in Figure 4.1, the control board monitors stroke, force, stress, strain rate, temperature and time. The mechanical system uses a hydraulic servo setup, which allows the operator exert tensile or compressive loads up to 10 tons at high strain rates. The direct current (DC) of an electrical charge passing through the test sample and electrical resistance of the material causes heat generation. Direct resistance heating allows ultra-high heating rates ($10^3 \frac{^\circ\text{C}}{\text{s}}$) which can be useful to avoid time-dependent phenomenon like grain growth at high temperature. Cooling regime, on the other side, can be achieved via several methods such as simple cooling by anvil/copper grips, or agitated one by means of air/inert gas/water quenching.

In the current study, a quartz tube was placed around the sample gauge to prevent severe oxidation of the hot-spot zone at high temperature. Moreover, to further protect the fracture surfaces, ultra high-purity argon gas (99.999%) was used as a backfill atmosphere in chamber. Also, R-type thermocouple (Platinum/Platinum-

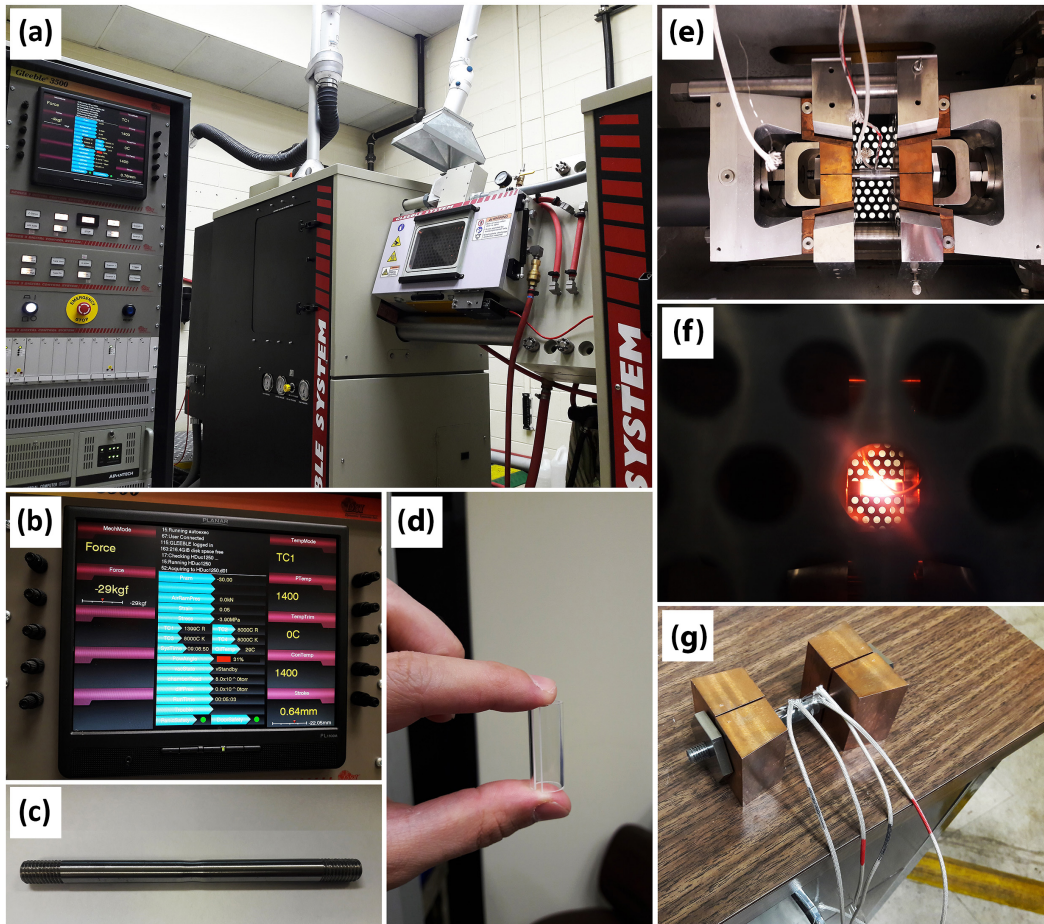


Figure 4.1: Layout of the thermomechanical testing: (a) Gleeble 3500 apparatus, (b) machine's monitoring system, (c) DP600 Gleeble sample, (d) quartz tube to avoid oxidation of the gauge, (e) loading setup in the chamber contains grips and water-cooled copper blocks, (f) sample heated up to test temperature, and (g) assembly of the Gleeble sample and thermocouples that are attached on the surface

13%Rhodium) was attached to the gauge surface to detect the temperature for each corresponding time. Flow of the DC electrical charge into the test sample was automatically controlled based on the temperature recorded by data acquisition system.

As can be seen in Figure 4.2, the Gleeble heating schedule was designed in slightly different fashions to cover all thermomechanical tests within a broad temperature interval. Reheating temperature of 1400°C and its corresponding soaking time were allocated as an important section of the schedule to ensure the microstructure and temperature at hot-spot zone are almost the same in all test batches prior to further thermomechanical processes. Furthermore, an equalizing time before tensile testing was considered to homogenize the temperature through each cross section of the

gauge. The maximum test temperature, 1480°C, was deliberately chosen to measure the maximum tensile strength over high temperatures where the microstructure is almost fully ferritic (δ -ferrite). It is worth mentioning that due to high susceptibility of the studying material to partial melting at mentioned temperature, and subsequently, detachment of thermocouples during the test, soaking time at 1400°C was decreased from 120 to 45s to prevent further softening of the material before the tensile test. All mentioned considerations were applied to minimize the process limitations which could affect results reproducibility.

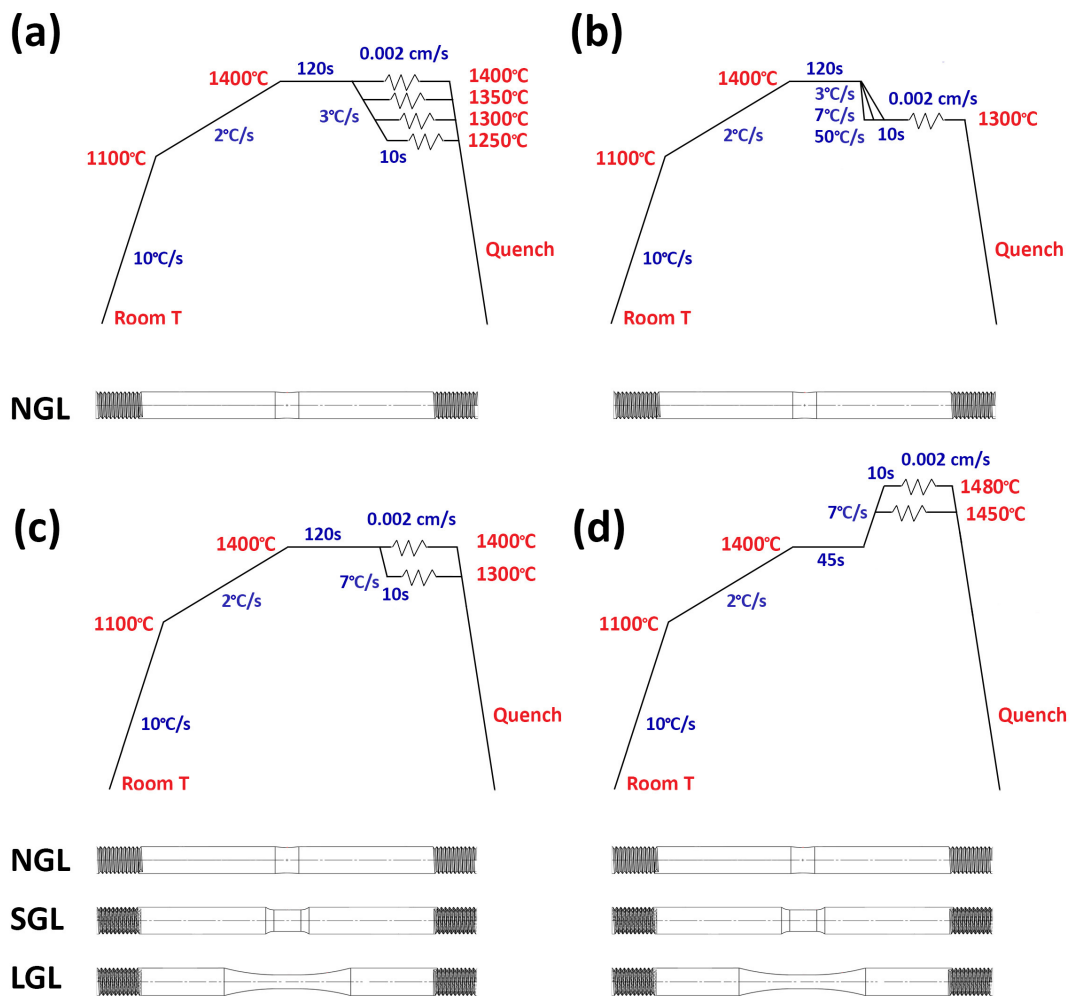
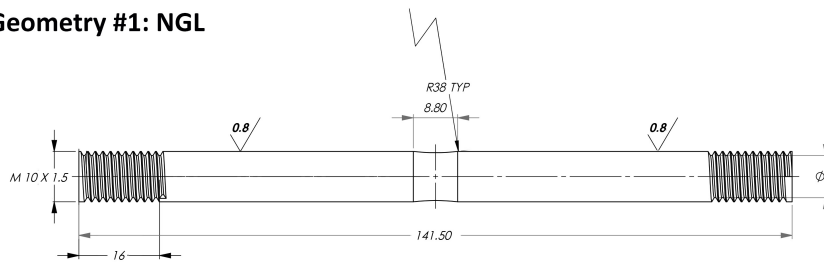


Figure 4.2: Thermomechanical regimes applied on (a and b) as-cast material, and (c and d) both as-cast and transfer-bar materials (sample codes are referred to the labels defined in subsection 4.3.1)

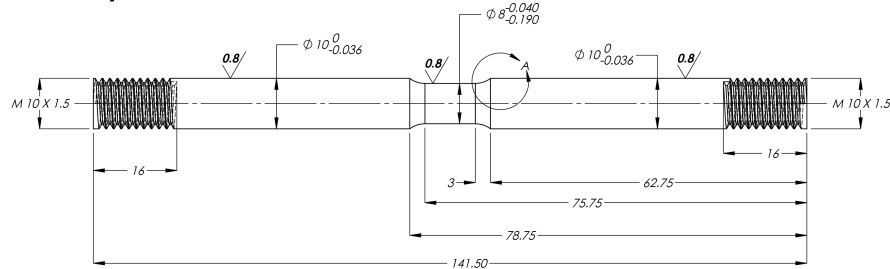
4.2.1 Sample Geometry

Choosing a suitable sample geometry was the most challenging part of the thermo-mechanical testing directly influencing the reproducibility of stress-strain data. As plotted in Figure 4.3, three various geometries, named **No Gauge Length (NGL)**, **Short Gauge Length (SGL)**, and **Long Gauge Length (LGL)** were employed. The reason behind this designation of these geometries referred back to the fact that thermal gradient and stress localization along the gauge length have significant effect on high-temperature mechanical properties *e.g.* maximum tensile strength and RA value. Theoretically, design of the NGL geometry was relied on minimizing the longitudinal thermal gradient within the central narrowed zone, and vice versa, for the LGL design. The SGL geometry, on the other hand, brought sharp stress localization on the shoulder due to smaller curvature radius compared with the others.

Geometry #1: NGL



Geometry #2: SGL



Geometry #3: LGL

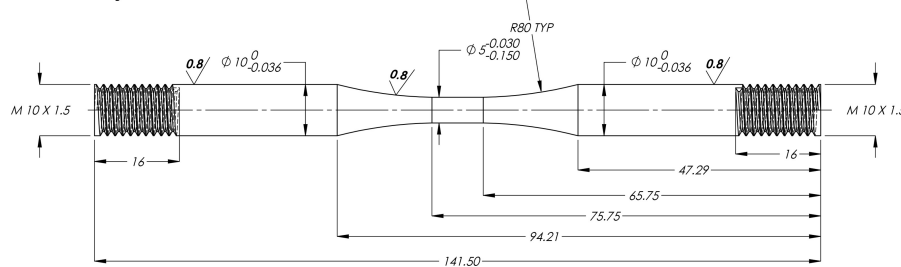


Figure 4.3: Sample geometries designed for the Gleeble test

As schematically shown in Figure 4.4, an R-type thermocouple was attached right at the middle of the gauge via spark-welding machine, and in SGL and LGL samples, the second one was placed on the location adjacent to the onset of increase in sample diameter taken place through the shoulder. Finally, the thermocouples were meticulously passed through the groove of the quartz tube, and attached to the thermocouple port in the Gleeble chamber. The thermomechanical program already discussed was coupled with the thermocouple #1 which was attached at the middle of the narrow zone.

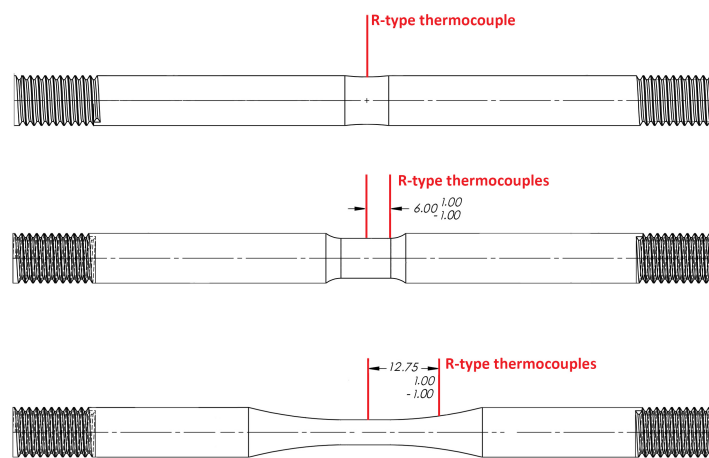


Figure 4.4: Locations of R-type thermocouples prior to thermomechanical test

4.2.2 Hot Ductility Measurement

Once the Gleeble test was done, the flow of the DC charge was automatically stopped and there was no control on the quenching rate of the fractured sample from test to room temperature, but continuous purging the ultra-high pure Ar gas into the chamber preserved the fracture surface from oxidation or contamination. For those which successfully pulled up, the vernier calipers was utilized to measure the RA as follows:

$$RA(\%) = \frac{(A_0 - A_f)}{A_0} \times 100 \quad (4.1)$$

where, A_0 and A_f are referred to the initial and ultimate cross-sectional area of the test sample. To accommodate samples fractured asymmetrically, an average of

five measurements was taken from each half. The results were also confirmed by random measurement via KEYENCE_{VHX6000} stereo microscope equipped with an image processing tool.

4.3 Microstructural Evaluation

To observe the as-received structures of DP600 AHSS, the as-cast and transfer-bar samples were mounted into a hot cured resin, automated ground and subsequently polished using STRUERS_{TEGRAMIN25} machine, and chemically etched in 4% Nital (96 ethanol-4 nitric acid). Sample preparation included five-step grinding by 320, 400, 600, 1200, and 2400 grit silicon carbide papers, and four-step polishing via clothes of 9 μm , 3 μm , 1 μm , and 0.05 μm lubricated by colloidal silica suspension (last step: OPS).

To conduct fractography, samples were cut cross-sectionally parallel to the fracture surface by means of STRUERS_{ACCOTUM5} precision cutter. Fracture surfaces of those Gleeble samples which did not experience partial melting were analyzed via JEOL_{6610LV} scanning electron microscope. Moreover, energy-dispersive X-ray spectroscopy (EDS) was carried out to analyze inclusions distributed on the fracture surfaces.

Measuring the grain size, area fraction of the ferrite and pearlite phases, and the total area of inclusions entrapped into the materials during casting process was carried out using the image processing toolbox in the KEYENCE_{VHX6000} microscope.

Chapter 5

Results and Discussions

5.1 Microstructural Characteristics in As-received Materials

In this section, the microstructural characteristics of the as-received materials such as, texture and morphology, phase identification, and grain size are presented. Also, a comprehensive discussion on phenomena, which are responsible for changes in microstructural features is discussed.

5.1.1 Structure and Texture

Depending on the content of alloying elements, and cooling rate from γ single-phase region to the ambient temperature, the as-received structure of the DP600 AHSSs usually contains ferrite, pearlite, and somewhat retained austenite. As seen in Figure 5.1, the microstructure of **as-cast material** contains:

α -ferrite, which is shown in white colour and includes a big fraction of the microstructure. The decomposition of γ -austenite to proeutectoid α leads to formation of allotrimorphic ferrite with polygonal morphology. Allotrimorphic ferrite is α -ferrite that grows faster in its internal structure rather than the neighboring grains [74], does not display symmetry in its own morphology due to irregularity in growth rate against constraining interfaces. The nucleation site for this type of ferrite is usually the primary γ GBs because there is no other 2D heterogeneous nucleation site interior of the γ grains, and the growth preferential direction is along the γ GBs.

Pearlite with monochromic black colour is transformed from the γ as a result of eutectoid phase transformation. There has been the other type of pearlite, called degenerated pearlite [75-77], that contains thicker lamellas of ferrite closely neighbored to fine cementite particles. In Figure 5.1, this type of pearlite can be observed as Zebra-pattern structure, which is formed under highly diffusion-controlled transformation. The occurrence of these two morphologies has been previously reported in C-Mn steels continuously cast at cooling rates of $30\text{-}300\frac{\text{°C}}{\text{s}}$ [75]. Since the chemical composition of the studying material has almost 0.1wt% C, the volume fraction of pearlite is obviously lower than the α regions.

Retained Austenite at low volume fraction is distinguishable with its brown colour. An increase in Mn and Si contents in some regions caused by high temperature solutal diffusion brings higher probability of retaining the γ due to reduction in carbon concentration [78, 79]. In this case, the effect of Mn is more significant than Si.

The **transfer-bar microstructure**, on the other hand, includes neither fine lamellar pearlite (black zones in as-cast structure), nor retained austenite. In Figure 5.1(c and d), the microstructures mostly show small pockets of degenerated pearlite banded between α grains. As mentioned earlier, the rough rolling process after heating the strand at $1000\text{-}1200\text{°C}$ in the reheating furnace (RF) causes a gentle deformation in the transfer-bar slab before further rolling process in which the grains are elongated along the rolling direction. Since the heating temperature is higher than $0.5T_m$ of the steel and the strain generated in the slab is higher than the critical value for the recovery ($\geq 7 - 10\%$), the elongated γ grains will be exposed to the DRX, and metadynamic recrystallization, *i.e.* the recrystallization process does not involve an incubation time of new grain nuclei [80], because recrystallized nuclei are already present along the γ GBs upon reheating in the RF [80, 81]. Therefore, α grains and pearlite pockets are finer than those in the as-cast material. Also, the slow cooling rate during reheating and rough rolling compared with the continuous casting process (almost $50\frac{\text{°C}}{\text{s}}$ on the slab surface) provides sufficient time to long-range diffusion of the solute-solutionized carbon into the matrix. As a result, higher tendency of the microstructure to form the degenerated pearlite rather than fine lamellar type as well as transformation of the retained austenite is expected.

Besides those advantages of the reheating and rough rolling processes given in the literature, decomposition of the retained austenite already present in the as-cast material to the allotrimorphic ferrite or degenerated pearlite in the transfer-bar structure prevents formation of deleterious epitaxial ferrite, which can form from the retained austenite by epitaxial growth on primary α during cooling from intercritical annealing temperature [82]. The intercritical annealing is the heat treating process in which the as-received material will be changed to the DP microstructure that contains α and martensite.

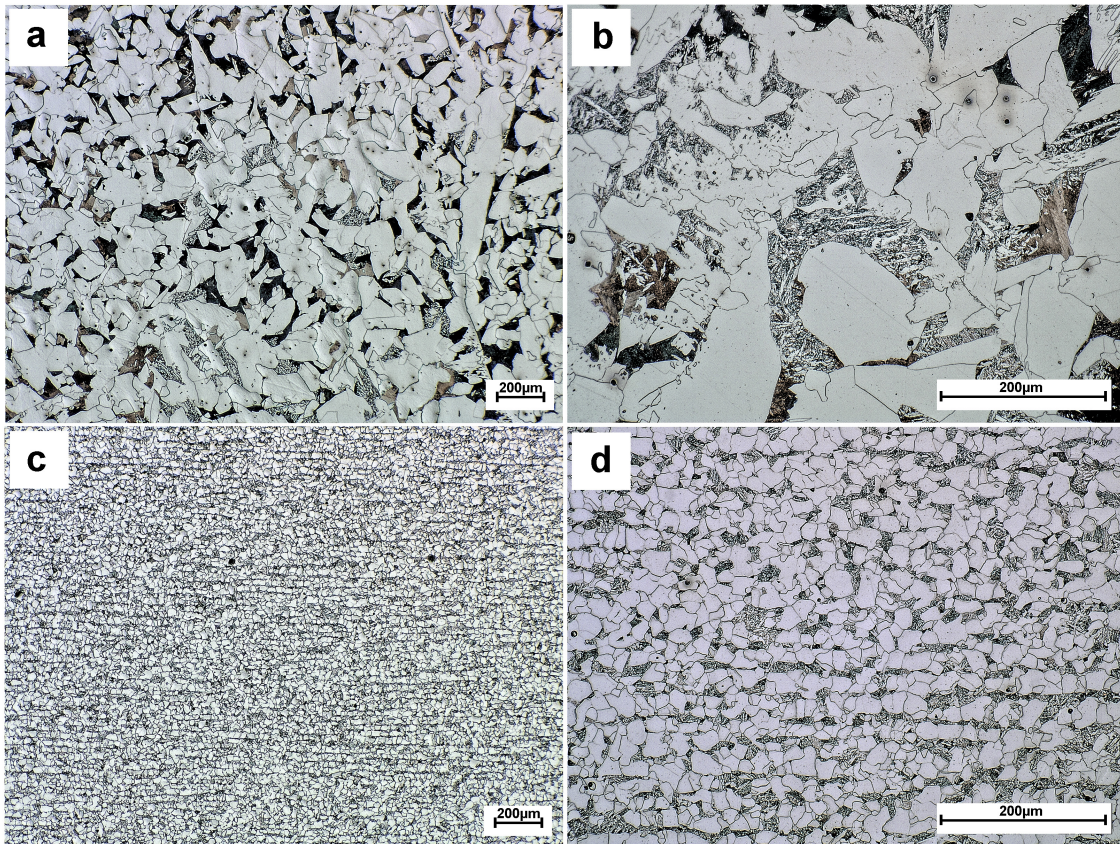


Figure 5.1: Optical micrographs of (*a and b*) as-cast, and (*c and d*) transfer-bar structures

In Figure 5.2, the back-scattered electron (BSE) analysis of different structures are illustrated for both as-cast and transfer-bar materials. While the as-cast material shows four different zones (ferrite, fine lamellar pearlite, degenerated pearlite, and retained austenite, respectively, 1-4), the transfer-bar material mainly shows two regions: ferrite and degenerated coarse pearlite. The difference between colour of ferrite and fine pearlite in as-cast sample is based on the fact that the contents of C, and

Mo in pearlite (point 2 in the EDS profile) are higher than those in ferrite (point 1 in the EDS profile) and these heavy elements makes pearlite brighter in appearance. The degenerated pearlite is easily recognizable in both materials based on their specific morphology. However, the retained austenite (point 4) is different from pearlite based on its irregular shape of boundaries, which is asymmetrically constrained by the other structures. Comparing points 1 and 4 also shows a difference in the colour that results from higher carbon solubility of γ -FCC structure versus α -BCC ferrite.

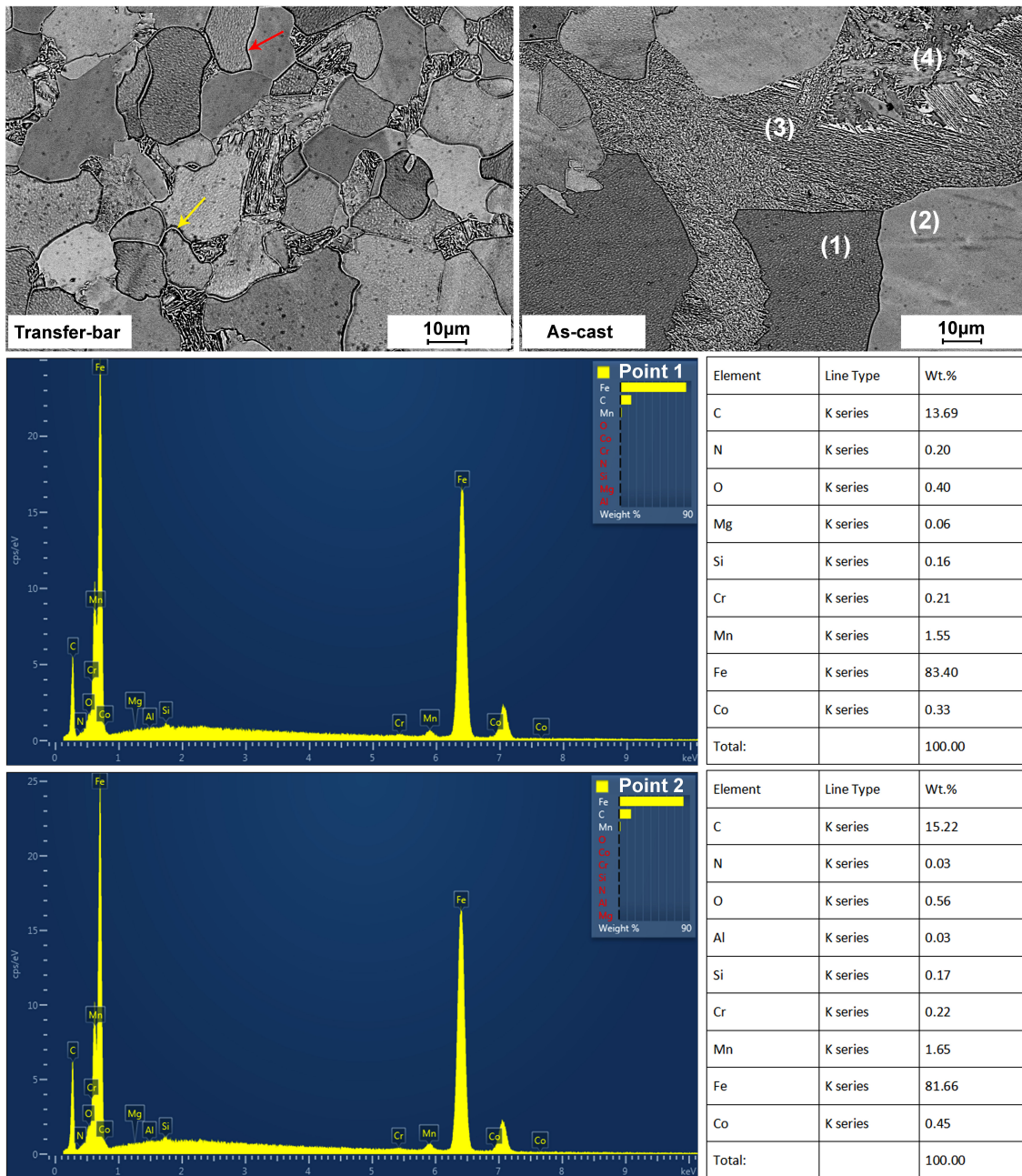


Figure 5.2: BSE analysis of the transfer-bar and as-cast microstructures: The yellow and red arrows identify solute pile-up and depletion, respectively

The transfer-bar sample also shows a gradient in the colour of the ferrite grains, which is more gentle as compared with the colour changes in the as-cast material. The reason likely comes from the variation in elemental distribution between those ferrite grains initially nucleated (darker zones) and new grains formed and grown near the eutectoid temperature (brighter zones). In other words, based on the partition reaction of elements in α/γ and $\alpha/\textit{pearlite}$ interfaces, *i.e.* retarding the eutectoid reaction by partitioning of substantial alloying elements between the parent (γ) and product phases (α or pearlite) due to slow diffusion of partitioning elements [83], solid-state segregation of atoms will create composition gradient between grains. In this case, the role of Cr and Mn should be more taken into account due to their positive segregation [83]. Moreover, the obvious contrast along the GBs in the transfer-bar sample (both bright and dark intergranular zones) can be referred to pile-up of Cr and Mn (yellow arrow in Figure 5.2) or depletion of Si solute atoms (red arrow in Figure 5.2) due to respectively positive and negative segregation in front of interfaces during the grain growth stage after the DRX [83, 84].

5.1.2 Ferrite Grain Size and Volume Fraction

Based on the micrographs shown in Figure 5.1, an average value of 20 random ferrite grains is presented as the grain size of ferrite. As given in Table 5.1, the size of ferrite grains is significantly decreased in the transfer-bar structure, while the pearlite fraction has been increased. As mentioned before, both features are a result of the recrystallization and grain growth during reheating and rough rolling. These two subsequent phenomena facilitate growing of numerous strain-free grains nucleated on the primary γ -phase GBs. Fine austenitic microstructure obtained by reheating in the RF has a higher tendency to form pearlite as compared with the coarse as-cast material rapidly cooled during the continuous casting. Since the suitable substrate where the pearlite pockets will start to form is γ GBs, fine austenite grains provides higher surface area of the GBs, which proliferates volume fraction of pearlite. Krauss also showed these preferential zones where the onset of eutectoid reaction takes place [85].

Table 5.1: Ferrite grain size and pearlite fraction in as-received materials

<i>Material</i>	<i>Ferrite grain size (μm^2)</i>	<i>Pearlite fraction (%)</i>
As-cast	5727	19
Transfer-bar	679	30

5.2 High-temperature Constitutive Properties

As mentioned earlier, high-, and ultra-high temperature mechanical behaviours are widely used to interpret the hot embrittlement phenomena happening within the temperature intervals in which softening mechanisms *e.g.* DRV, DRX, and void coalescence are severe or no more existed due to the peritectic reaction or partial melting. In the following section, the effect of thermal and geometrical parameters on the constitutive behaviour of as-cast and transfer-bar DP600 AHSS are shown. For this purpose, the test temperatures have been meticulously chosen based upon a proprietary mathematical model at ArcelorMittal, France, that calculates the evaluation in solid fraction with temperature, as listed in Table 5.2. The reported quantities are in a good accordance with the data achieved from pseudobinary phase Fe-C diagram, as shown in Figure 5.3. The maximum test temperature (1480°C) is deliberately selected very close to the peritectic reaction, where γ and δ phases can both exist, and partial melting is inevitable.

Table 5.2: Critical temperatures measured by computational technique

	<i>Liquidus</i>	<i>Peritectic</i>	<i>Solidus</i>
Temperature (°C)	1519	1483	1476

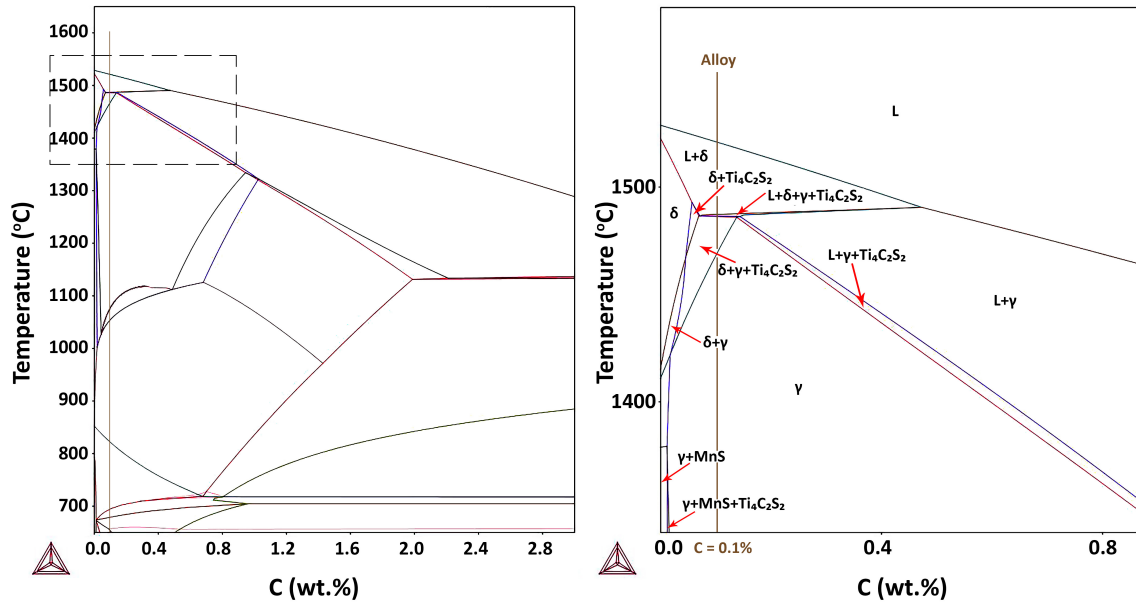


Figure 5.3: Pseudobinary Fe-C phase diagram at constant Cr, Mn, Mo, Ti, and S, and the magnified region of the temperature interval tested in this study

5.2.1 Effect of Test Temperature and Cooling rate on As-cast Material

As demonstrated in Figure 5.4, the first set of Gleeble experiment is implemented on the as-cast (AC) samples with NGL geometry. According to the subfigure (a), the engineering stress versus displacement is plotted within a range of temperature, where two tests are performed at each temperature. Before starting a discussion on the effect of temperature on the σ -displacement curve trend, there has been a specific characteristic at high temperatures that makes these curves recognizable from those at ambient temperature and described as:

Wavy σ -displacement curve, which is associated with discontinuous dynamic recrystallization (dDRX) in austenite, will take place at high temperatures and low values of the strain rate [86]. This manner is due to repetitive sequences of strain hardening and softening caused by nucleation of new recrystallized grains during deformation. Afterwards, the flow stress continuously decreases with increasing displacement until a dynamic balance between strain hardening and strain softening, also called steady state deformation, can be established. For materials with low to medium stacking fault energy (SFE) like austenitic Fe, the dDRX phenomenon is common, while fer-

ritic Fe shows continuous dynamic recrystallization (cDRX) and high intensity of the DRV instead of dDRX due to high SFE [86]. High temperature ($T \geq 0.5T_m$) and low strain rate (mostly $10^{-3} - 10^{-4} \text{ s}^{-1}$ in steels) brings a situation in which the nucleation frequency of the recrystallized grains would be adequate to generate multiple peaks in the σ -displacement curve. It has been reported that the DRV starts at maximum stress peak and almost 98% of recrystallization will take place prior to the first peak after the maximum stress peak [87, 88]. This means that the multiple peaks observing after the maximum stress peak are concurring with the grain growth phenomenon of those grains prerecrystallized in the structure. The remaining recrystallization ($\sim 2\%$) will simultaneously happen at the growing boundaries, called necklace mechanism, and cause to the dDRX. However, nucleation can be also happened at twins, inclusions within the grains, and deformation bands, particularly in as-cast material with coarse microstructure [87].

In Figure 5.4(a), by increasing the temperature, the fluctuation amplitude is being decreased due to increase in size of the subgrains formed during the DRV. As their size increases, the number of dislocations in subgrains will be reduced, so there have been less dislocations arranged in more orderly arrays during the DRV. Less dislocations that lower the Gibbs free energy will diminish the tendency for the DRX as well as dDRX. In other words, an increase in test temperature will intensify the recovery rate, while the structure becomes less prone to the dDRX. A decrease in the dDRX causes less localized strain hardening and consequently damped oscillation in the σ -displacement curve. Sakai and Jonas also reported some findings on 0.06%C-1.43%Mn steel tested over a range of 900-1260°C at $1.4 \times 10^{-3} \text{ s}^{-1}$ strain rate [87].

Also, an increase in the test temperature shows lower values in engineering stress at each displacement. The reason is relied on some factors *e.g.* intensifying the rate of dislocations annihilation, increase in the number of vacancies and their diffusion rate that enhance vacancies clustering and void formation, the grain growth, and dissolution of high-temperature precipitates and carbides associated with substantial atom diffusion to the SFE in γ phase [88-90]. The last item, also called stacking fault shrinkage, is accompanied by separation of partial dislocations make climb and cross slip [88, 90]. Irregular trend in displacement values between test temperatures necessitates further experiments, which are discussed in next sections.

In subfigure (b), the effect of cooling rate, from an intercritical temperature (1400°C) to the test temperature (1300°C), on the σ -displacement curve has been revealed. It is expected that increase in cooling rate leads raising in both maximum stress and amplitude of fluctuation. Since the holding time at intercritical temperature was 120s, assuming a similar initial thermo-physical features before cooling to the test temperature *e.g.* grain size, dislocation density, kinetic of static recovery and recrystallization during isothermal holding, and subgrain size seems reasonable. Therefore, the reason of changes in curves comes back to the lattice shear strength of the mother phase, γ , varies by the content of carbon element interstitially embedded into the octahedral spaces of the austenite.

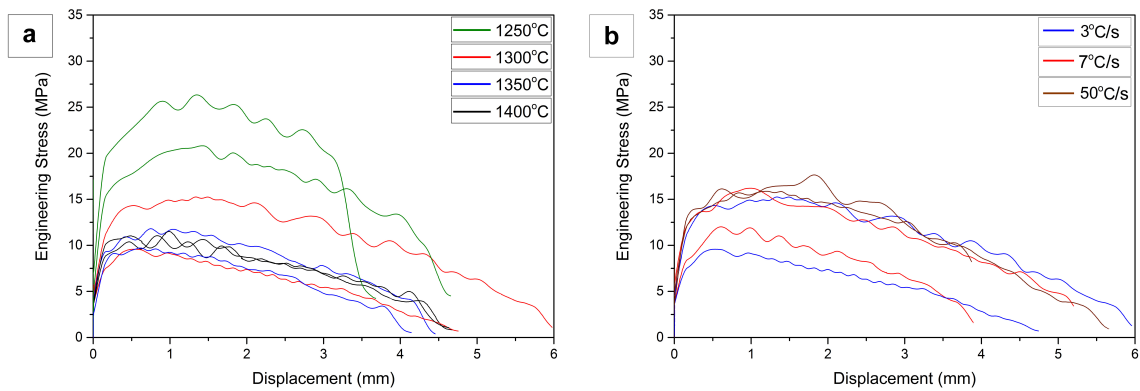


Figure 5.4: Engineering stress versus displacement at various (a) test temperatures ($CR=3\frac{^{\circ}C}{s}$), and (b) cooling rates from holding to test temperature of 1300°C

Based on literature, there is a precipitate, titanium carbide in this case, which can be formed and stabilized from cooling austenite even at ultra-high temperatures (1300-1400°C) [91, 92]. This fact has been also confirmed in the pseudo-binary phase diagram given in Figure 5.3. The precipitate $Ti_4C_2S_2$ forms during the peritectic reaction. As the structure slowly cools to the test temperature, an adequate time for diffusion of C from interstitial regions to Ti-rich zones enables $Ti_4C_2S_2$ to precipitate into the matrix. Since the temperature is very high, the volume fraction of $Ti_4C_2S_2$ will not be significant. High cooling rates, on the other hand, retard the diffusion kinetic of C and consequently carbon atoms will be trapped into γ lattice structure. The last scenario brings the γ structure more shear strength. Higher shear strength increases the friction force against dislocations mobility and subsequently

strain hardening. Finally, an increase in strain hardening brings higher dislocation density that motivates the DRX and dDRX by intensifying the necklace mechanism. The effect of lattice shear strength on the DRX intensity in alloys with high or low stacking fault energy was extensively discussed by McQueen and Sakai [88, 89]. On the other side, slow cooling rates facilitates the DRV, which causes lower amplitude of the curve fluctuation.

Inconsistency in data at different cooling rates and its dependence on various factors *e.g.* diffusion kinetic, presence of high-temperature carbides, less importance of metadynamic recrystallization during cooling compared with the static one within the intercritical temperature and the DRX during the Gleeble test provides motivation to focus on the role of test temperature on constitutive behaviour in next sections.

In Figure 5.5, the effect of test temperature on the RA, failure stress, and maximum engineering stress is illustrated. The sample at 1300°C shows maximum ductility or RA, while the other one tested at 1350°C shows a kind of embrittlement compared with other test temperatures. Higher ductility and lower failure stress at 1300°C compared with 1250°C and 1400°C can be referred to higher strain rate sensitivity (m) that brings more plasticity during the test. In spite of all temperatures at which the final stage of deformation before failure has been associated with void nucleation, growth and coalescence, the sample at 1300°C does not show this manner in its σ -displacement curve. According to Klepaczko [64] and Benzerga *et al.* [93, 94], the void-coalesced mode of fracture is identified by a drastic drop in σ value within a narrow range of displacement at the near-final stage of tensile test. Less susceptibility of the sample tested at 1300°C to void growth and coalescence is ascribed to lower volume fraction of initial porosity in its as-cast structure, or a thermomechanical phenomenon called *diffuse necking*.

There have been critical test temperature and strain rate in which the material will experience diffuse necking after maximum peak stress, *i.e.* the stress in the tensile test decreases slowly with displacement due to occurrence of a balance between strain hardening and thermal softening mechanisms in several regions [95], that is why the necking is diffused from one place to another before ultimate localized necking, or sharp necking, that led to failure. At very high temperatures (1400°C), void growth and coalescence as well as high DRV rate are responsible for weakening the material

and localizing the necking, while at lower temperature (1250°C), higher intensity of strain hardening rate provides more strain localization along the necking zone, and again facilitates localized necking.

A decrease in maximum peak stress by increasing the temperature is also attributed to thermal softening mechanisms such as subgrain coarsening, dislocation annihilation, ease of flow at triple junctions to relieve stress concentrations, and diminishing the GB sliding due to scalloping of the GBs, *i.e.* irregular GBs, caused by intensifying the DRV [88]. For the material tested at 1350°C, further analyses are necessitated to discover the story behind its embrittlement, as presented in next sections.

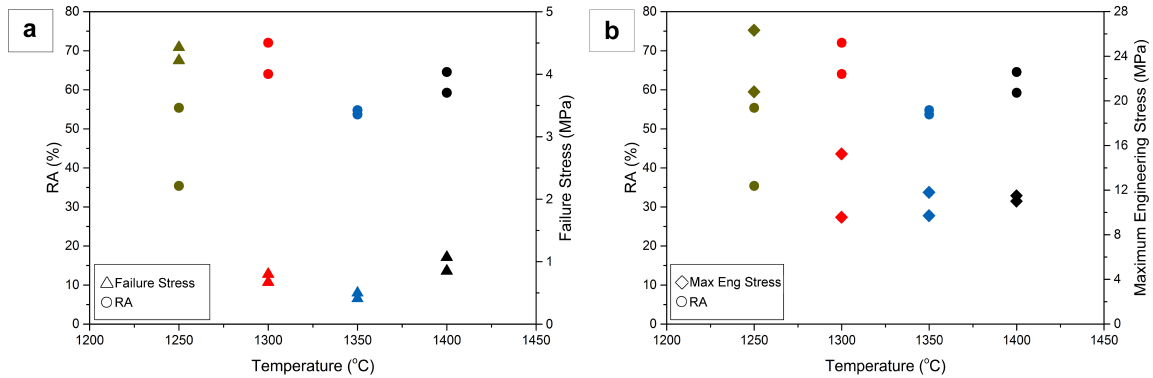


Figure 5.5: Effect of test temperature on (a) RA - failure stress, and (b) RA - max engineering stress measured in Figure 5.4(a)

As discussed in this subsection, there are various parameters affecting the constitutive manner of the as-received DP600 such as temperature, strain rate, stress localization, porosities, and presence and distribution of high-temperature precipitates. All mentioned factors can be optimized via selecting the suitable microstructure and processing parameters. Designing different sample geometries allows to comprehend the effect of stress localization, both thermal and tensile, on the high-temperature mechanical properties of the studying material. Meanwhile, the transfer-bar (TB) samples with recrystallized grains show less volume fraction of porosities and better distribution of high-temperature carbides and inclusions compared with the as-cast (AC) microstructure.

5.2.2 High-temperature Mechanical Properties of LGL Samples

The σ -displacement curve of LGL samples are plotted in Figure 5.6. To have a better discussion on the following subsections, examining the Figures 5.12, 5.13, 5.14, and 5.15 is also recommended.

Effect of sample geometry: Comparing the data achieved for both AC and TB samples confirms that the LGL geometry provides a very good consistency between the results for each pair of test samples at various temperatures. This geometry with a very gentle slope along its shoulder (high r value of the shoulder) experiences almost homogeneous stress distribution along the gauge length during subjecting to the thermomechanical Gleeble test. Moreover, the thermal gradient between two thermocouples is steep (shown in subsection 5.2.6), which guarantees that the hot-spot zone during testing will take place on the middle of the gauge. Both characteristics govern a situation in which samples tend to show the localized necking rather than diffuse necking. The localized necking mostly happens right on the middle of the gauge due to the highest temperature as well as severe stress localization happened on the minimum cross-sectional area. The localized heat on the central part of this geometry with small gauge diameter makes samples vulnerable to the partial melting even at temperatures that are much below the solidus temperature, 1476°C, (see Figure 5.12/TB-LGL sample).

Effect of initial microstructure: Except those samples tested at 1400°C, the others show almost equal or higher maximum engineering and failure stresses in TB samples compared with the AC samples. The RA in TB samples, on the other hand, reveals a lower value at 1450°C as compared with the AC samples. In terms of the RA, the AC samples show less susceptibility to localized melting rather than TB samples (see Figures 5.12 and 5.15), which can be resulted from heat sinking by preexisted porosities in AC samples that entrapped gas with lower thermal conductivity compared with solid structure [96]. Thus, the TB-LGL sample shows severe melting at 1450°C associated with high super-heat through the inter-columnar (and -dendritic) zones, while the AC-LGL at the same temperature is subjected to partial melting mostly happened on triple junctions (or the last zones solidified during continuous

casting). The synergy among high volume fraction of the melt, more fluidity of the molten material due to higher super-heat, and low tolerability of the melt against the tensile load in TB samples at 1450°C causes a drastic drop in its ductility. The small fraction liquid that is present in the AC samples can fill those porosities and microvoids preexisted in the structure, called self-healing effect [97], as shown in the interconnected AC-LGL fractograph in Figure 5.15. Thus, the AC samples show good RA values at 1450°C.

Effect of temperature on the AC samples: First, three mechanisms that are playing important roles at each temperature interval are necessary to recall: intensified DRX and grain boundary sliding at ($T \leq 1350^\circ\text{C}$), intensified DRV and diminishing boundary sliding at ($1350^\circ\text{C} < T < 1450^\circ\text{C}$), partial or localized melting at ($T \geq 1450^\circ\text{C}$), and phase transformation at (1480°C). In this category, each mechanism can overlap the others, but will be controlling mechanism in its own interval. Based upon that, the RA improves with temperature due to an increase in both DRV and melt fraction. As already mentioned, stress relief in triple junctions as a result of severe DRV postpones stress localization during the test, but the dependency of void growth and coalescence on temperature neutralizes the effect of DRV at 1400°C, so the RA at 1300 and 1400°C is almost same. By increasing the temperature, the AC samples tend to fracture at higher stresses associated with more fraction of melted zones tore apart during tensile testing. Maximum engineering stress shows improvement at both 1400 and 1480°C compared with 1450°C. Its increase at 1400°C is referred to intensified void deformation before failure, while the scenario at 1480°C is related to γ to δ reverse transformation that is accompanied by an increase in lattice volume, shrinkage in voids, thermally-grooved boundaries, and generation of dislocations due to transformation stresses. Dippenaar and Phelan also reported the occurrence of some microstructural changes in 3Cr12 steel by means of high-temperature laser-scanning confocal microscopy [98]. Although the rate of DRV in δ is much higher than γ [88], the reasons mentioned above lead to an increase in the stress peak at 1480°C.

Effect of temperature on the TB samples: In TB samples, melting is observed at each temperature and its intensity can be categorized as partial melting at (1300°C) to severe melting at (1450 and 1480°C) (Figures 5.12 and 5.15). The reasons presented for the trends of failure and maximum stresses in AC samples can be valid for TB

samples, as well. On the effect of temperature on the RA, minimum values at 1300 and 1450°C can be assigned to the augmented DRX coupled with partial melting, and severe localized melting, respectively.

5.2.3 High-temperature Mechanical Properties of NGL Samples

Regarding the terms and figures mentioned in previous subsection, the data of σ -displacement curve of NGL samples can be interpreted according to Figure 5.7.

Effect of sample geometry: It can be seen that the dominant mechanism of failure in AC samples is void formation, growth, and coalescence while the TB samples show more susceptibility to diffuse necking. The reason comes back to the geometry of NGL samples that do not have a gauge. This means that at each test temperature, the whole part of the middle zone - with a very gentle decrease in diameter - is exposed to nearly the same temperature. In TB samples, there is no preferential weak zone in which the sharp necking can be initialized. AC samples, on the other hand, are prone to sharp localized necking due to preexisted porosities.

Effect of initial microstructure and temperature: As it can be seen in Figure 5.7, both AC and TB samples show a very similar trend in their failure stress values. Also, the failure stress does not significantly vary between 1300 and 1450°C. In terms of the RA, both structures present the maximum value at 1400°C. According to the Figures 5.13 and 5.14, high DRV rate and subsequently subgrain-, and grain growth provides better ductility at the expense of diminishing the maximum stress, while samples at 1300°C present lower RA because of the presence of inclusions in grain boundaries and triple junctions (see Figure 5.14). Decreasing the RA and maximum stress values at 1450°C can be also referred to tearing apart of high fraction of melted material.

5.2.4 High-temperature Mechanical Properties of SGL Samples

The results of the Gleeble test on the last geometry used in this study are shown in Figure 5.8. Comparing the analyzed data of the SGL samples with two previous geometries reveals that the number of data as well as their reproducibility are insuf-

ficient due to higher percentage of failed test during the Gleeble testing. The reason is caused by the sample geometry as there has been a vulnerable zone to stress localization right near the shoulder. The steep slope of increased diameter in SGL sample (low value of r on the shoulder) not only generates higher localized stress, but it also has an effect on the rate of void growth and coalescence due to difference in stress triaxiality. The term stress triaxiality ratio, *i.e.* the ratio of the hydrostatic stress on von Mises stress [99], is a factor that shows the tendency of an under-load material to the brittle fracture.

As the temperature increases, the failure stress does not show a big difference between its values, while the RA and stress peak data follow a very diverged trend that are strongly affected by the stress triaxiality. From the Figure 5.8, it can be also concluded that the mode of necking is varied even at constant temperature, as seen at 1400°C. To sum up, there cannot be an acceptable thermomechanical mechanism to be employed as a discussion of this subsection.

5.2.5 Comparison between LGL, NGL, and SGL Samples' Data

As a comparison between the data achieved for three different geometries, Figure 5.9 presents all high-temperature mechanical results extracted from the current study. Regardless of the discussions given in previous subsections, the LGL geometry shows better reproducibility. Also, samples with this geometry are successfully tested within a wide range of temperature between 1300 and 1480°C. The SGL geometry, on the other hand, is neither able to provide consistent data at each temperature, nor tested successfully to cover all test temperatures. The NGL design provides better repeatability than the SGL one, while it shows a considerable difference with the LGL design based on the mode of necking due to a substantial difference in thermal gradient along the axial direction.

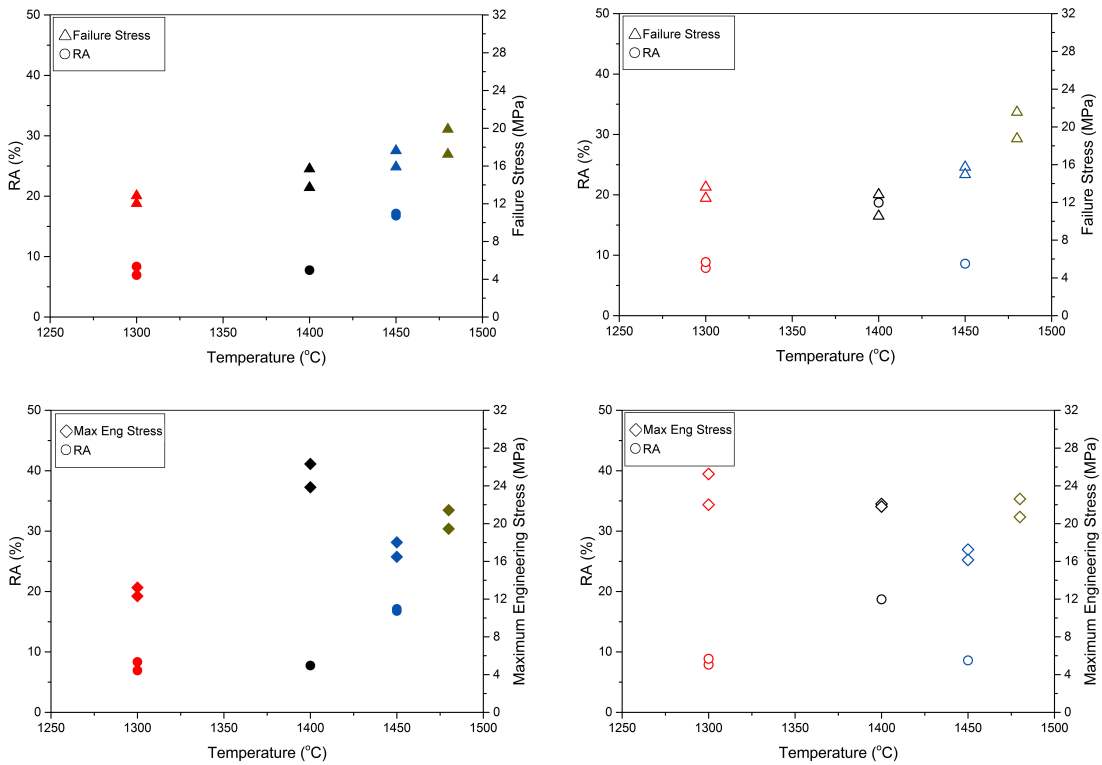
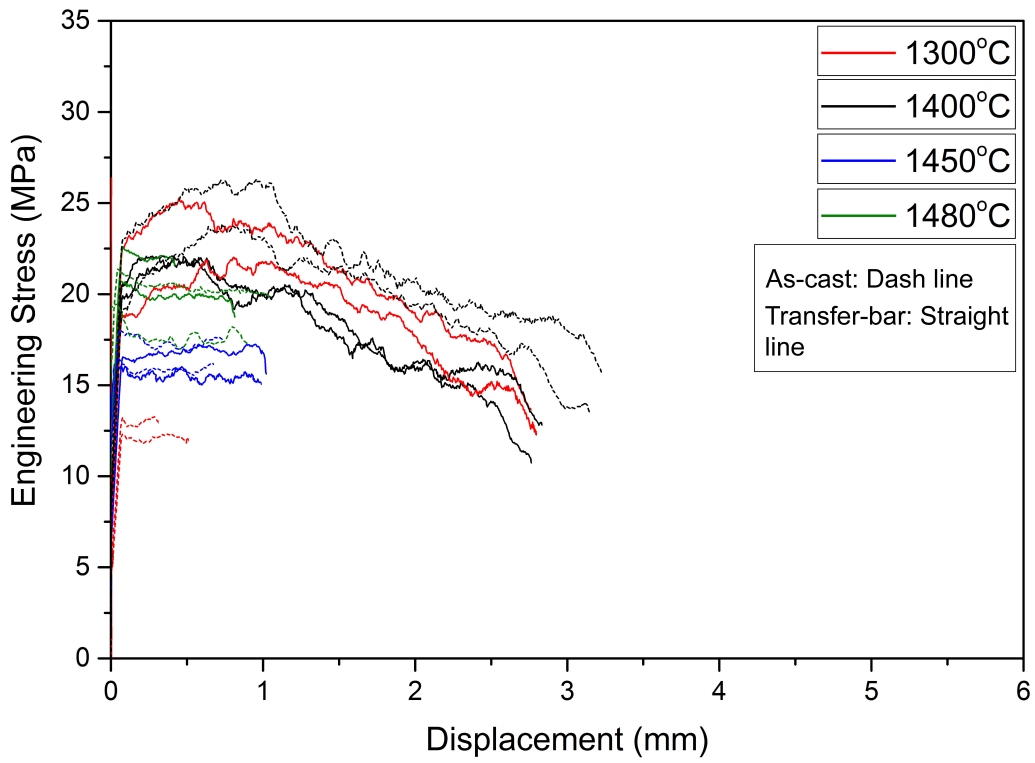


Figure 5.6: Stress-displacement curves and corresponding characteristics in (*left column*) as-cast , and (*right column*) transfer-bar LGL samples

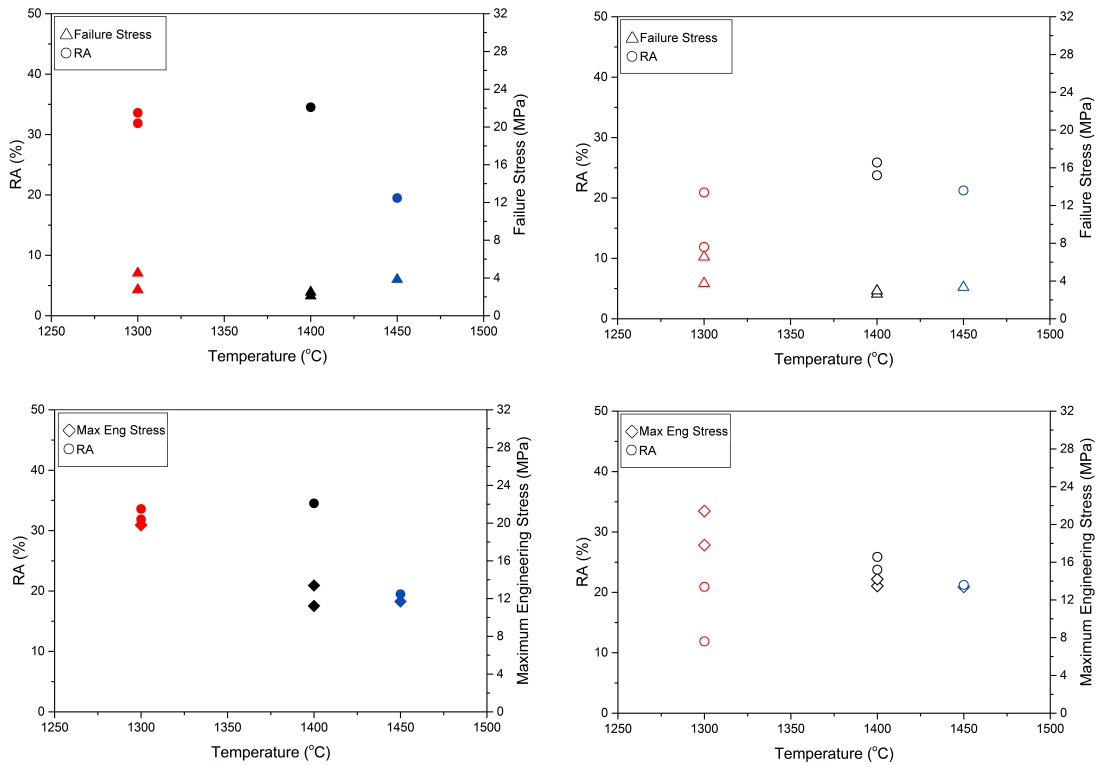
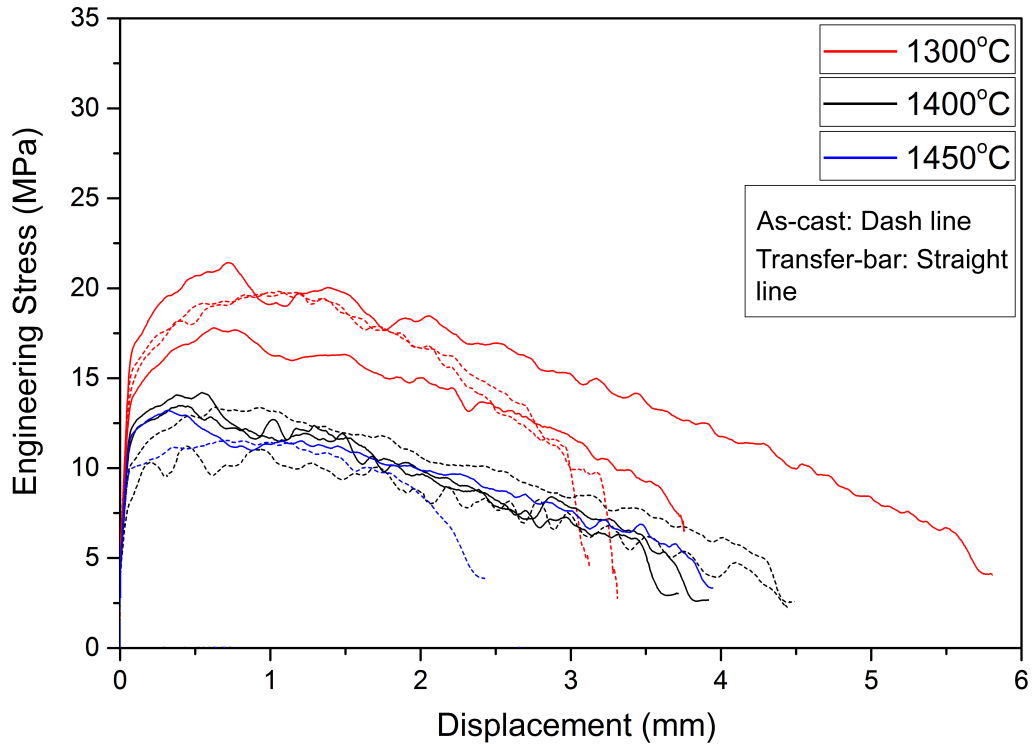


Figure 5.7: Stree-displacement curves and corresponding characteristics in (left column) as-cast, and (right column) transfer-bar NGL samples

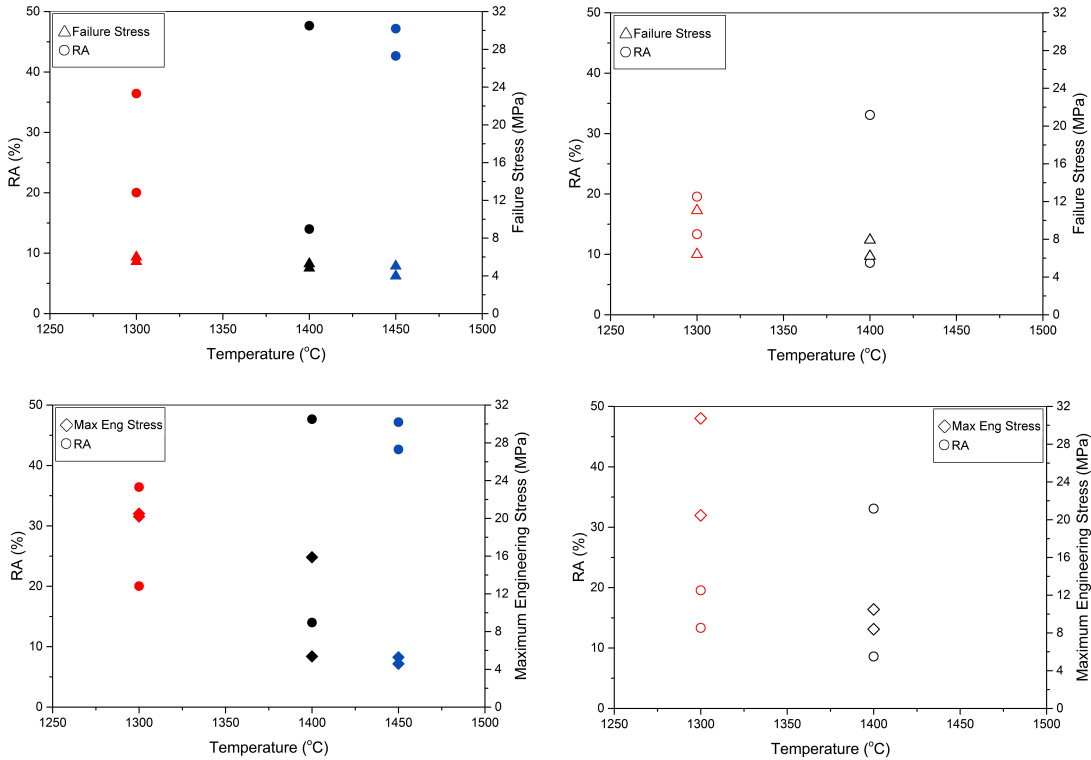
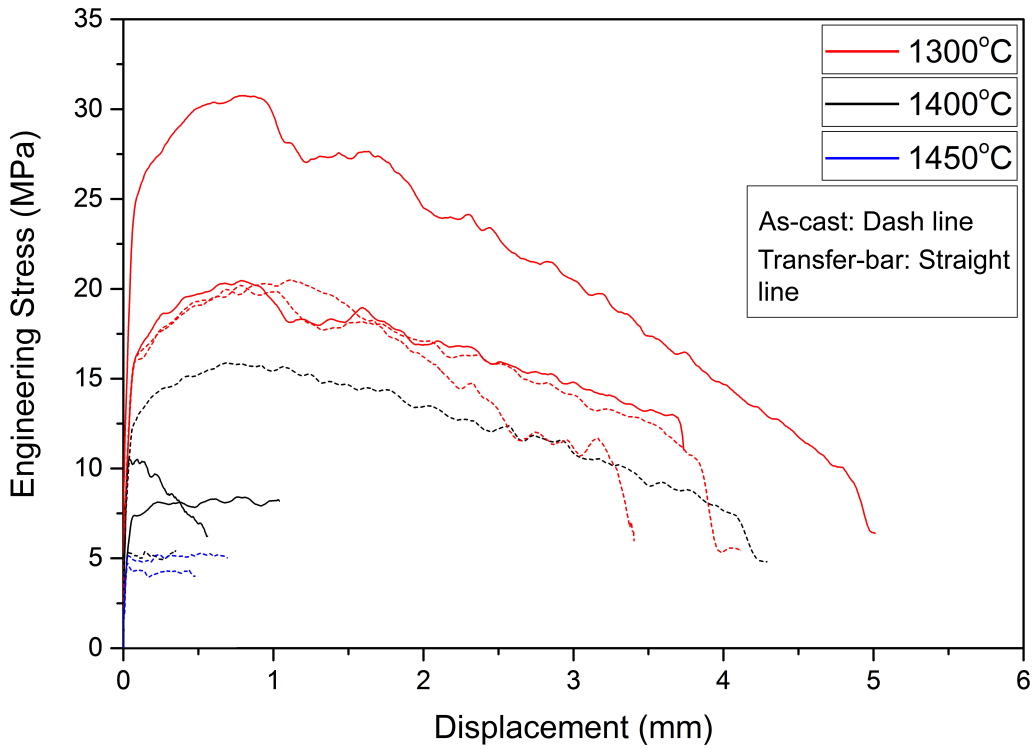


Figure 5.8: Stree-displacement curves and corresponding characteristics in (left column) as-cast, and (right column) transfer-bar NGL samples

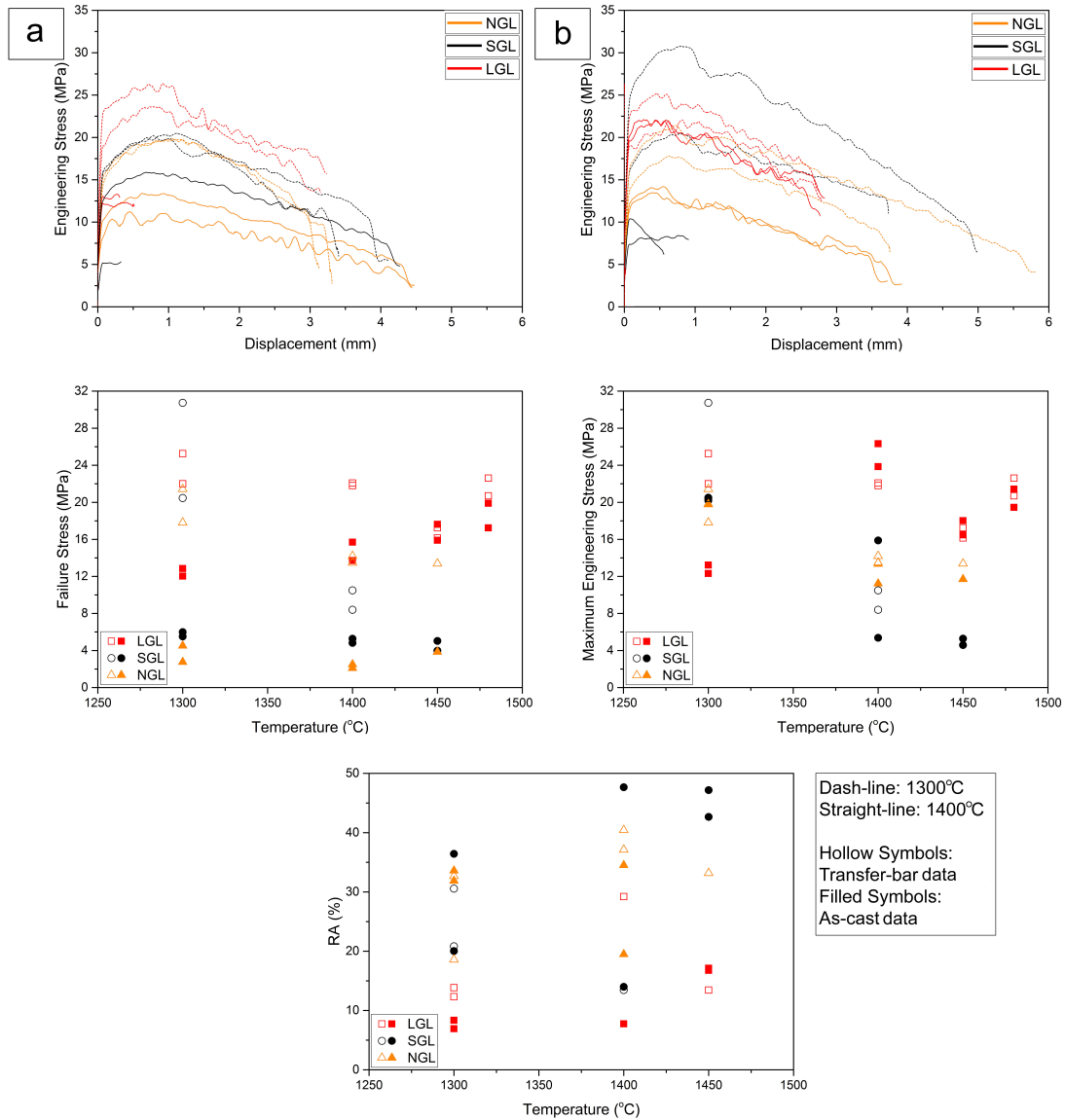


Figure 5.9: Comparing constitutive data between different geometries of (a) as-cast, and (b) transfer-bar samples

5.2.6 Temperature Gradient and Fracture Area

According to the Figure 5.10 plotted by the Gleeble data, the difference between temperatures recorded by two thermocouples is much greater in the LGL geometry. As the test keeps continuing, the heat input provided by the DC current is synchronized to the temperature recorded from the TC1. The thermocouple TC2, however, shows shallower heating rate as well as lower temperature at each recorded time. As long as the test sample will be exposed to thermal gradient along its gauge, the gap

between the temperatures is inevitable. After cooling the sample from intercritical temperature, 1400°C, the Gleeble test is started at isothermal condition. However, the temperature recorded by the TC2 gradually decreases during the test due to displacement of the sample caused by applied tensile and thermal loads.

In terms of reproducibility of data, a combination of low stress triaxiality and high thermal gradient provides a condition in which stress localization takes place right at the hot-spot zone that happens on the center of the gauge length. In this situation, sharp localized necking will be dominant. Otherwise, the diffuse necking associated with less data reproducibility will be the controlling mechanism.

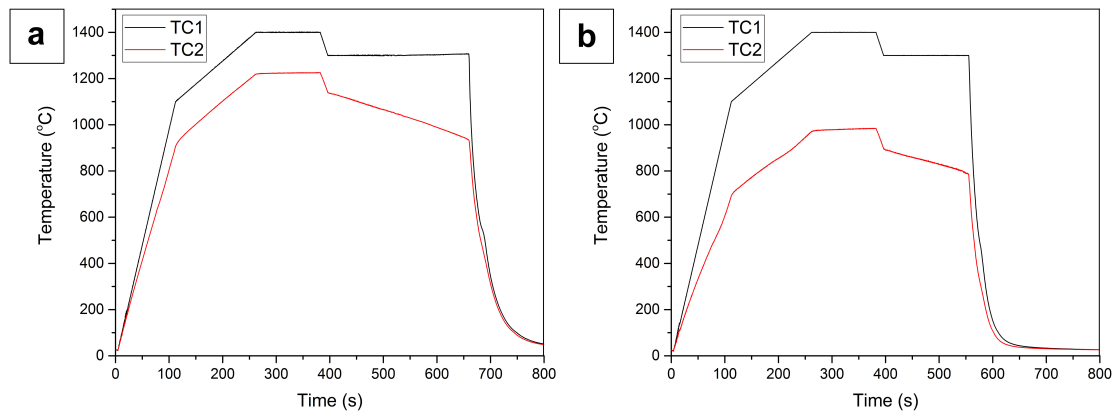


Figure 5.10: Temperatures recorded by TC1 (thermocouple on the center) and TC2 (on the shoulder) for (a) TB-SGL, and (b) TB-LGL samples tested at 1300°C

Figure 5.11 reveals the broken Gleeble samples and their fracture surface area. By comparing the optical micrographs of fracture surfaces with the RA data presented in 5.9, it can be concluded that the optical fractography is a suitable candidate to manipulate the image processing to both quantitatively and qualitatively show the ductility and RA values at each geometry. To put this simply, lower area of fracture surface means higher RA and more tendency to ductile fracture.

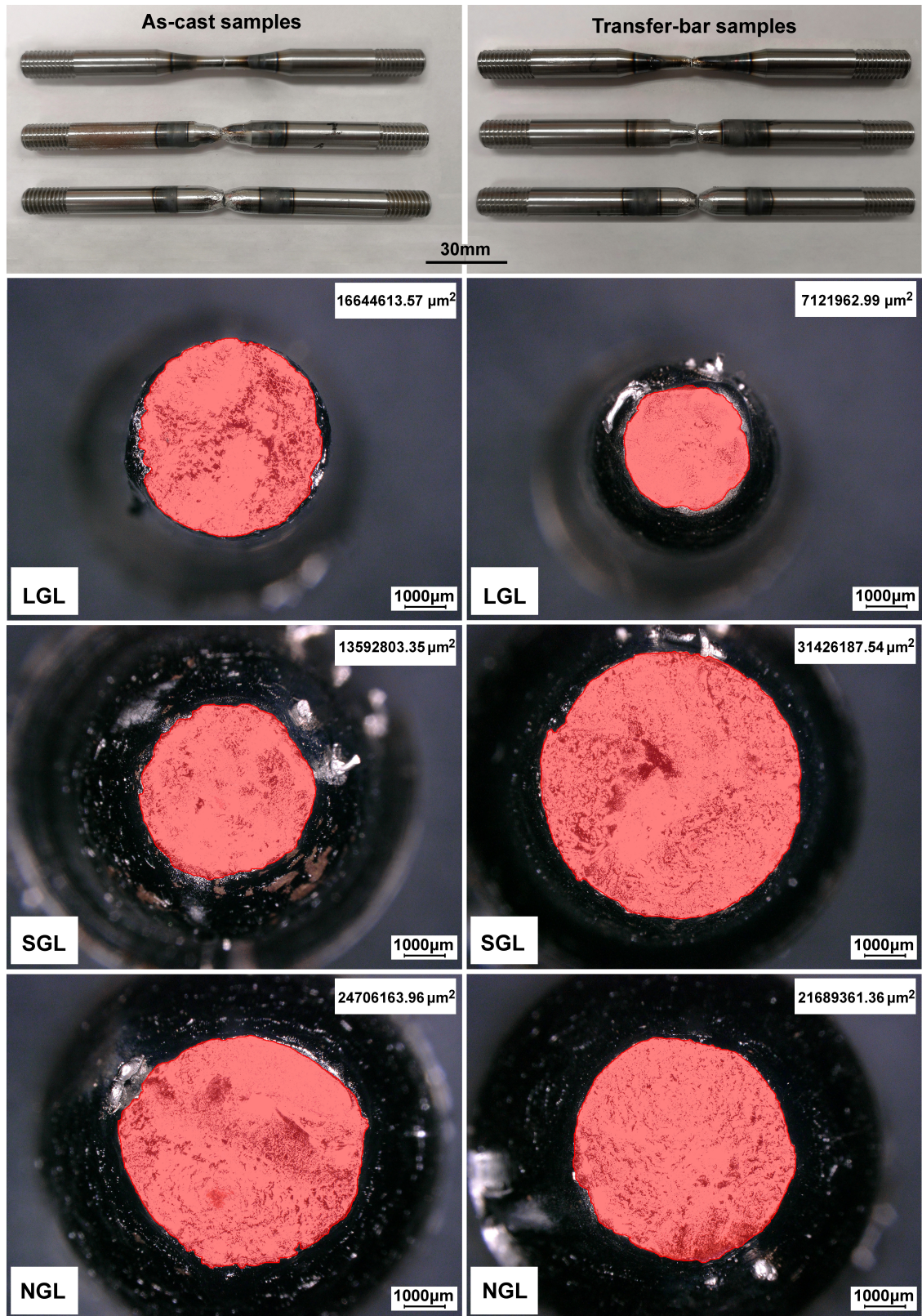


Figure 5.11: The Gleeble test samples and their fracture surface area at 1400°C, (left column) as-cast, and (right column) transfer-bar materials

5.3 SEM Analysis of Fracture Surfaces

In this section, the SEM fractography of the samples with different processing parameters is employed to better interpret the fracture mode at each condition. For this purpose, the effect of geometry, temperature, and initial microstructure on fracture behaviour is discussed.

5.3.1 Effect of Sample Geometry on Fracture Analysis

As seen in Figure 5.12, the fracture surfaces of the transfer-bar samples tested at 1300°C are shown at two different magnifications. By comparing different geometries in this figure, some thermomechanical and microstructural features such as fracture mode, controlling softening mechanisms, and melting susceptibility can be extracted. Toward this ends, the TB-NGL sample shows low susceptibility to melting, just on the tip of paraboloid-shape zones, while the decrease in gauge diameter to the TB-LGL sample increases partial melting intensity due to higher temperature localization. The reason behind the rosette-shape dendrite in TB-LGL sample is melting of interdendritic regions, which were solidified at lower temperatures during the continuous casting process. Rejected alloying elements to the solid/liquid interface during the solidification, leads to the formation of highly concentrated solid surrounding the primary dendrite arms. This area that is solidified at last stages of solidification has a lower melting temperature, which then melts during the reverse cycle, heating.

The fracture mode in the TB-NGL sample is ductile somewhere associated with healing effect in which the voids formed during plastic deformation can be fed by a very small portion of the molten material. Since the melting is not taken place over a wide surface area, void nucleation and growth act as another factor to conduct brittle fracture in some regions as well. The LGL sample shows brittle mode due to tearing apart of the melt that is formed with high volume fraction. Although voids in this sample can be fed by the melt, the maximum efficiency of the self-healing is achieved when the melt is pasty and can be preserved inside the voids during high-temperature deformation. The SGL sample presents an intermediate condition, combination of brittle and ductile modes, however, the presence of some detached zones is ascribed to the stress localizing due to its sharp-shoulder geometry.

As shown in TB-LGL sample fractography, although the interdendritic cavity can be filled up by the melt due to high penetrability of the liquid, the melt cannot withstand against the tensile load. As the super-heat in the LGL sample is higher than other geometries, the liquidified material loses its viscosity associated with melting of low-concentrated solid material. To put this simply, the liquid formed very close to the peritectic tie-line is very pasty, however, an increase in temperature provides more liquid fraction with less viscosity. In terms of the RA mean value, the NGL, SGL, and LGL transfer-bar samples show almost 25, 27, and 14% at 1300°C.

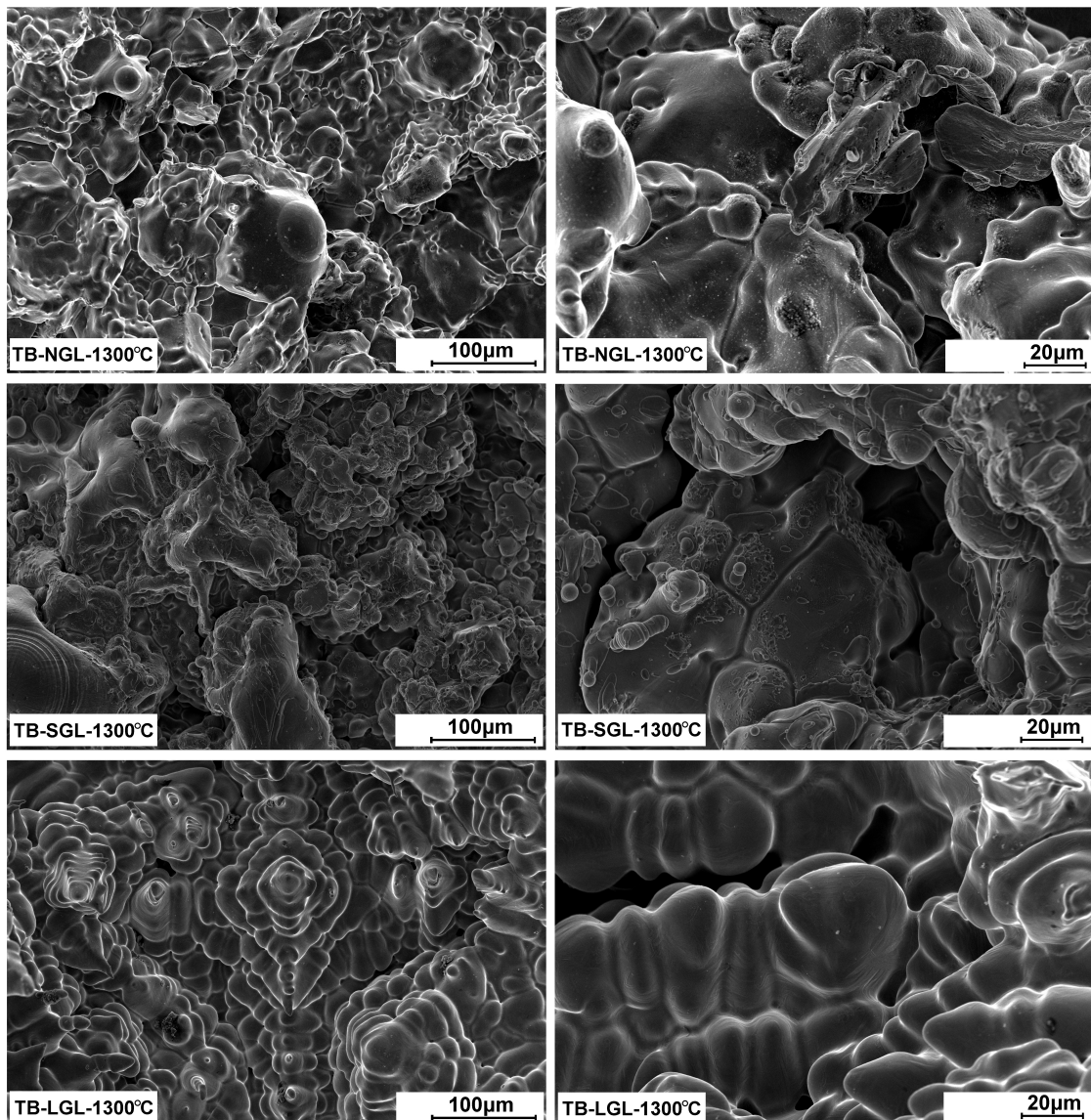


Figure 5.12: Fractographs of transfer-bar samples tested at 1300°C (Rows from top to bottom: NGL, SGL, LGL geometries at two magnifications)

5.3.2 Effect of Test Temperature on Fracture Analysis

Figure 5.13 shows the effect of temperature on fracture surfaces of the AC-NGL samples. As can be seen, three different magnifications at each temperature allow to understand the mode of fracture over a wide zone on the fractograph as well as deformation mechanism between neighboring grains. The first thing that is evident is coarsening of the structure at 1400°C. As mentioned in previous section, while the dominant mechanism at 1300°C is severe DRX, the sample tested at 1400°C shows higher intensity of DRV and grain growth. The less melting susceptibility of the AC material compared with TB samples can be confirmed in this figure by focusing on the highly magnified triple junction at 1400°C (bottom-right subfigure). As seen, the edge of each grain keeps its sharp morphology with no irregular deformation, which approves that no melting was taken place at triple junctions. The governing mechanism at 1400°C can be declared as grain sliding due to weakening of the grain boundaries at high DRV rate, while for the sample at 1300°C, void growth and coalescence can be presented (upper-left subfigure). Another reason behind the grain sliding at 1400°C can be also related to the role of disequilibrium vacancies at high temperatures. To avoid vacancy clustering, the grains move over each others to consume a portion of generating vacancies and contribute superplasticity, same as mechanism during power-law creep [100]. Both structures show ductile fracture accompanied by high RA (see Figure 5.9). In this case, the AC-NGL shows almost 33% mean RA, and 20MPa stress peak at 1300°C, while 27% mean RA and 13MPa stress peak are achieved at 1400°C.

5.3.3 Effect of As-received Structure on Fracture Analysis

In Figure 5.14, the fractographs of the AC and TB samples tested at 1300°C are given at three magnifications. Although both samples show partial melting, the naked paraboloid-shape zones, dendrite branches, adjacent to deep voids in the TB-NGL sample elucidate that the fraction and fluidity of the melt formed in TB sample are higher (middle-right subfigure). The AC sample, on the other side, shows a monolithic fracture surface that was fed by the sluggish liquid. In this case, the AC structure at high magnification, shows a trace of preexisted porosities in the central

zone that are enlarged due to thermal expansion and subsequently filled by the melt, self-healing effect (bottom-left subfigure). The presence of inclusions entrapped in grain boundaries and triple junctions of the AC-NGL sample acts the other factor on its high-temperature failure (middle-left subfigure). Finally, some polygonized grains shown in the AC-NGL sample confirms the high rate of DRV and DRX over this thermomechanical condition (same subfigure). In terms of high-temperature mechanical properties, the AC-NGL shows 33% mean RA and 20MPa stress peak. On the other side, the TB-NGL provides 25% mean RA and 20MPa stress peak.

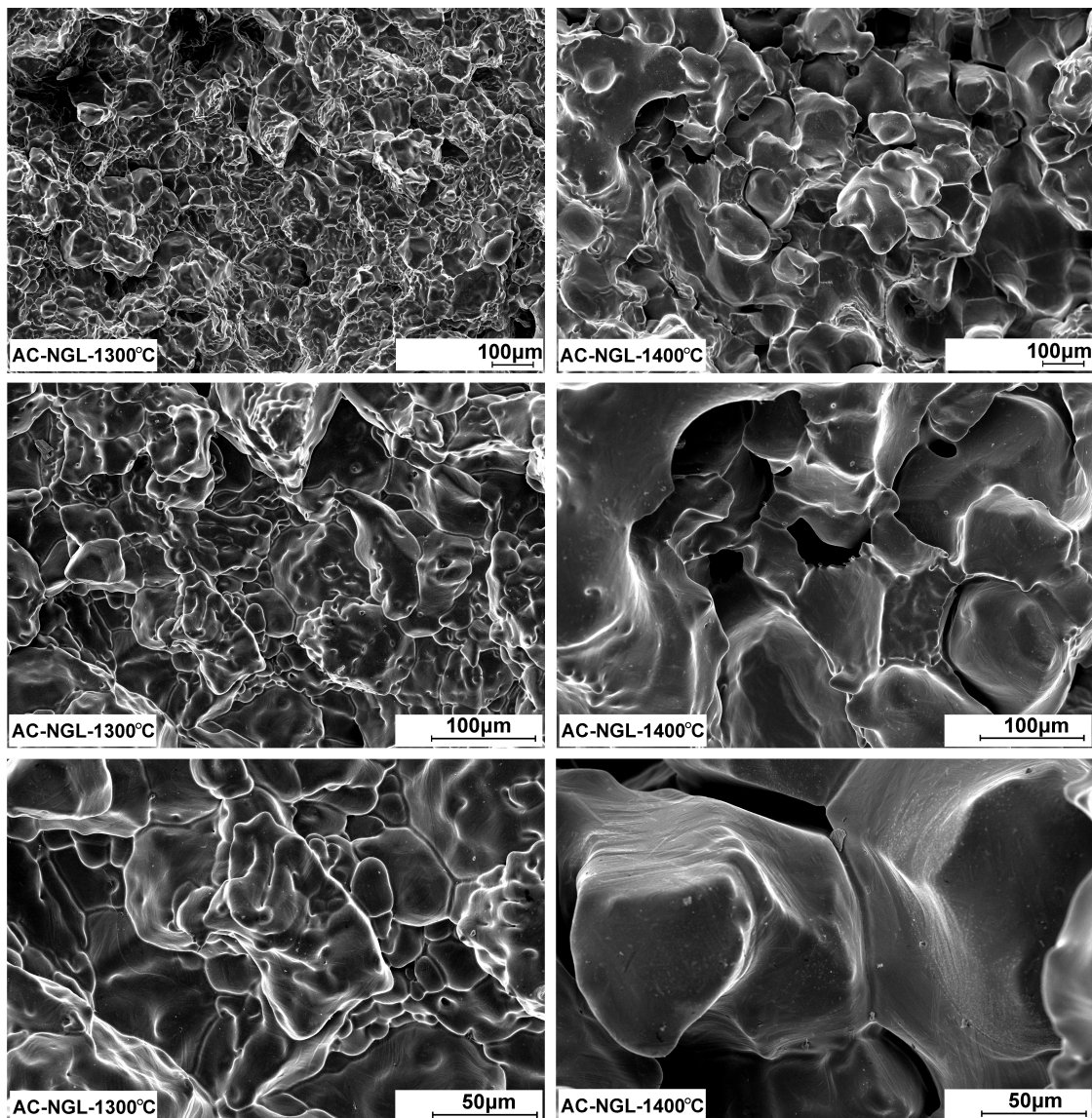


Figure 5.13: Fractographs of as-cast NGL samples at three magnifications (Left column: tested at 1300°C, and Right column: tested at 1400°C)

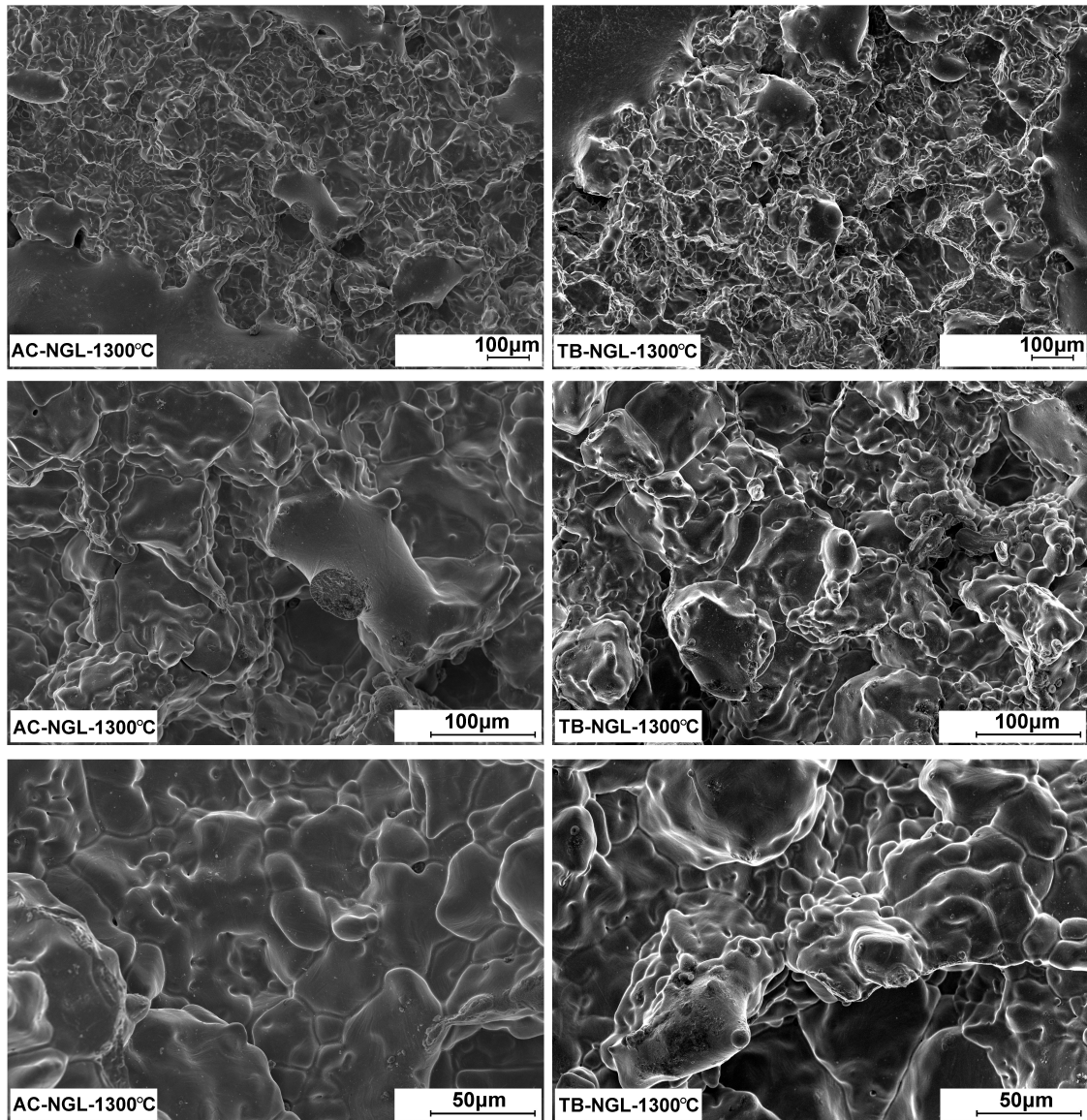


Figure 5.14: Different magnifications of fractographs in NGL samples tested at 1300°C (Left column: AC, and Right column: TB initial microstructures)

5.3.4 Fracture Mode of As-received Structures Tested at Near-peritectic Temperature

Figure 5.15 demonstrates the effect of an ultra-high temperature on the fracture surface of the AC-LGL and TB-LGL samples, which are presented in three different magnifications. As can be discussed, testing at 1450°C subjects both structures to highly localized melting, where the severity in TB sample is again higher (bottom-right subfigure). The healing effect accompanied by reverse transformation of γ to δ ,

which is associated with expansion in lattice volume leads to present the monolithic fractographs, where there is no trace of big detachment or void coalescence (bottom-left subfigure). The reasons behind low ductility of these samples can be assigned to an abnormal grain growth associated with tearing apart of the melt formed at 1450°C. Also, as the rate of the DRV in the δ phase is significantly higher than the γ phase, the less motivation on dislocation annihilation in ferritic regions could be taken into account as the other determining factor on their brittle fracture mode [88].

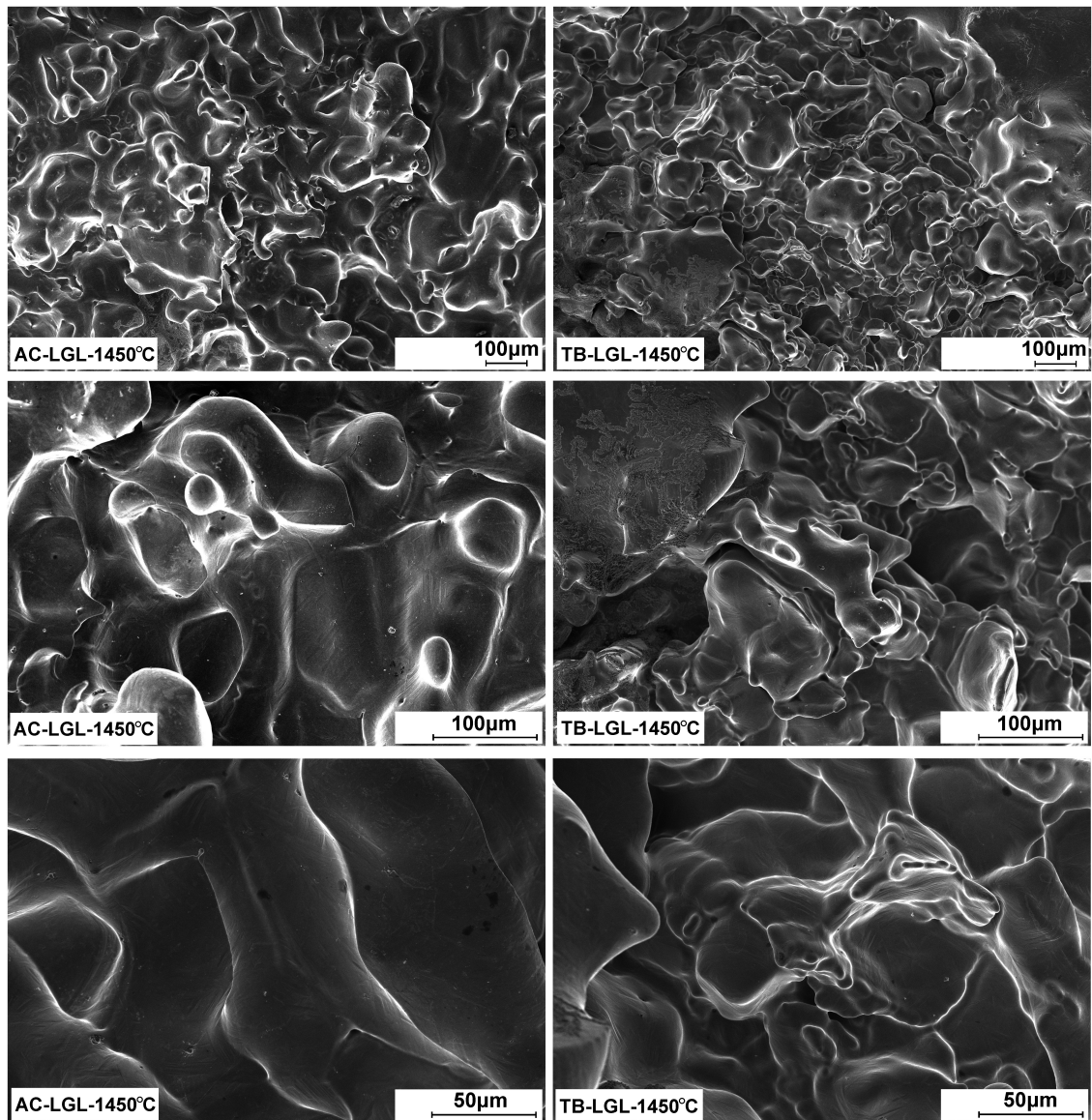


Figure 5.15: Different magnifications of fractographs in LGL samples tested at 1450°C (Left column: AC, and Right column: TB initial microstructures)

5.4 Effective Parameters on High-temperature Embrittlement of DP600 AHSS

To sum up the most important parameters that effectively played roles on the mode of fracture in as-received DP600 AHSS, a concise explanation is presented in this section, which is divided to: the effect of partial melting, low-melting temperature phases, and high-temperature inclusions.

Partial Melting due to Temperature Localization

As discussed in previous parts, based upon the test temperature, sample geometry, the as-received microstructure, the high-temperature tensile specimen can be exposed to temperature localizing through its necking zone, which brings partial or at higher severity, localized melting. The presence of liquid leads to early onset failure that intensifies tendency to hot embrittlement.

In semi-solid state, the viscosity of the melt decreases with an increase in temperature. This means that there is a critical process parameter in which the transition from ductile to brittle fracture will take place. In terms of ductility, low volume fraction of the melt associated with higher viscosity is suitable by filling the voids formed and coalesced during constitutive deformation, while higher volumes with increase in fluidity can be easily pulled apart during testing and caused brittle fracture. As seen in Figure 5.16, the interdendritic regions are more prone to melting due to their lower solidus temperature compared with the primary branches of dendrites. The reason comes back to the fact that during solidification, the last areas that solidify are the interdendritic zones, because the primary dendrites reject alloying elements to their front solid/liquid interface as well as their peripheral zones, called partitioning [101]. The retained melt at the end of solidification has a lower solidus temperature due to higher concentration of alloying elements.

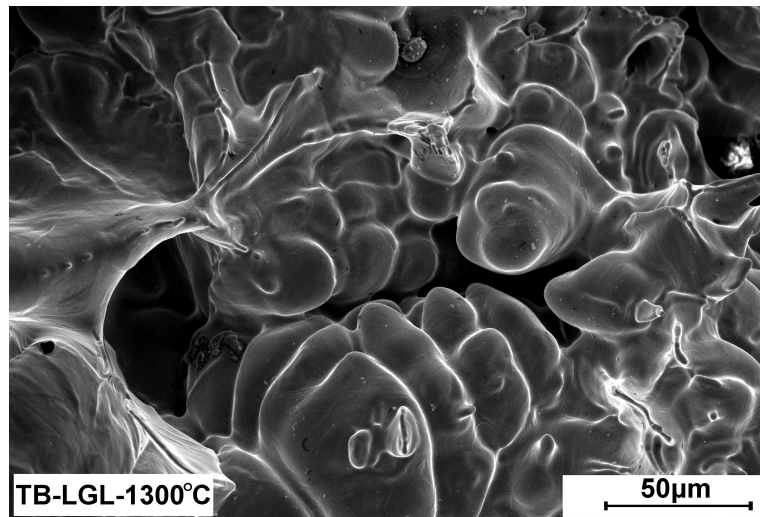


Figure 5.16: Partial melted zones in LGL sample tested at 1300°C

Presence of Low-melting Phases in the GBs

As the EDS profile of the point 2 in Figure 5.17 shows, there have been some S-rich precipitates embedded in the fracture surface of the TB-LGL sample. Although before the casting process of steels, Mn is deliberately added into the ladle to react with sulfur and form MnS precipitates that are less harmful, the formation of low-melting S-rich phase is sometimes inevitable. This phase, which is formed within a temperature interval so much lower than the solidus temperature, keeps its liquid state during the Gleeble testing. By spreading between austenite grains and wetting their GBs, this phase leads to weaken the shear strength of the material along the shear bands, *i.e.* narrow zones developing during deformation of ductile materials in which the shear stress is reached its maximum value [94]. The reason behind the presence of this phase in fractograph is due to its low partition coefficient during solidification that is used as a criterion to show the tendency of an alloying element to be rejected during solidification. Lower partition coefficient, K_0 , higher value of segregation and vice versa, as shown in Table 5.3 [101].

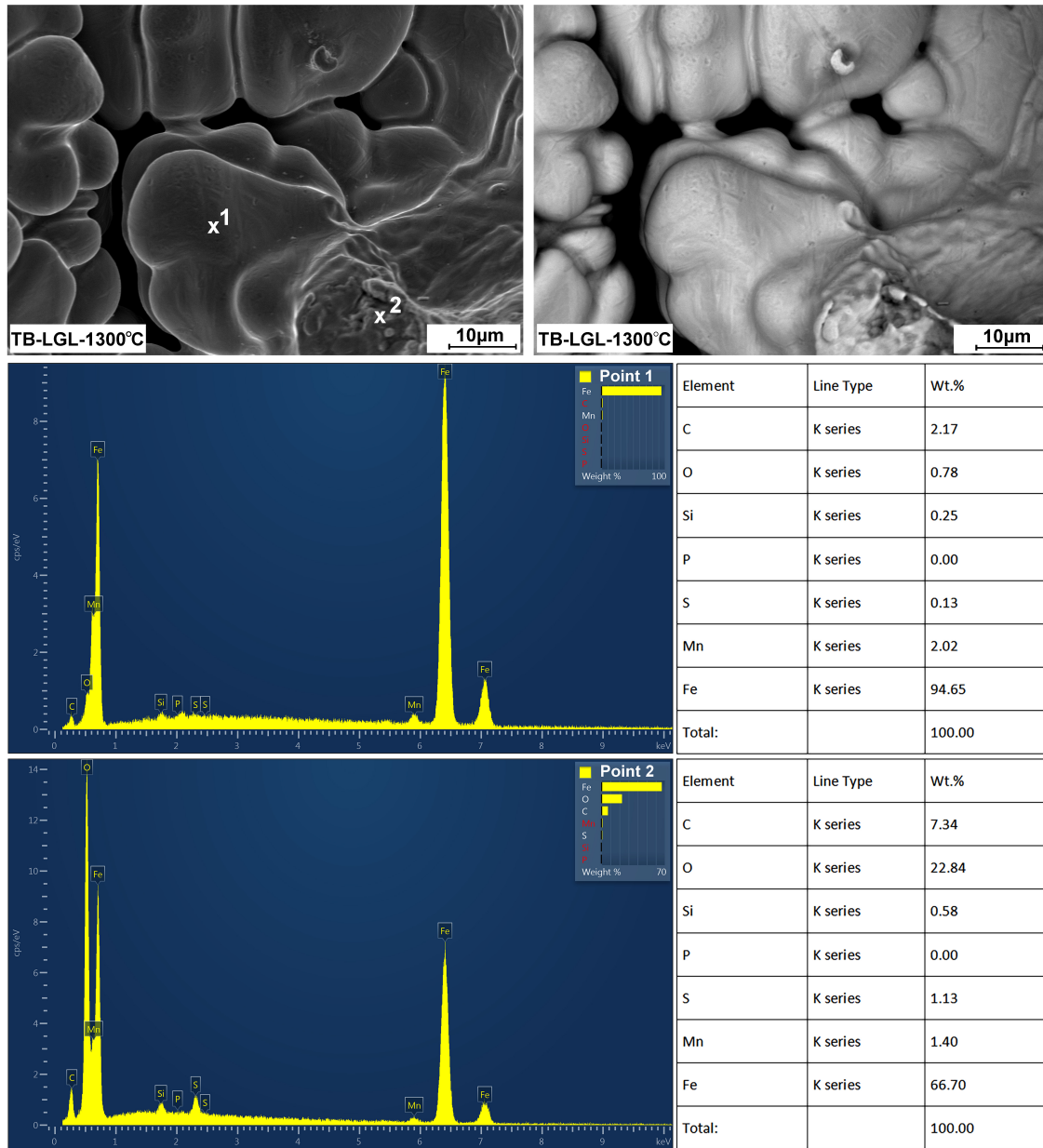


Figure 5.17: Sulfur-rich phase and the EDS profiles of the primary and low-melting phases

Table 5.3: Values of K_0 in δ and γ during solidification of binary iron alloys [101]

Element	Ti	C	Cr	Mn	Mo	Ni	N	P	Si	S
$\delta - BCC$	0.14	0.13	0.95	0.84	0.80	0.80	0.28	0.13	0.66	0.02
$\gamma - FCC$	0.07	0.36	0.85	0.95	0.60	0.95	0.54	0.06	0.50	0.02

Presence of High-temperature Inclusions in Triple Junctions

According to Figure 5.18, there has been a round-shape inclusion that is shown with both BSE and SE analyses, and precipitated in the triple junction. The Ca-peak with high intensity in the EDS profile confirms that this inclusion should not be as a reaction product between the alloying elements existed in the initial composition.

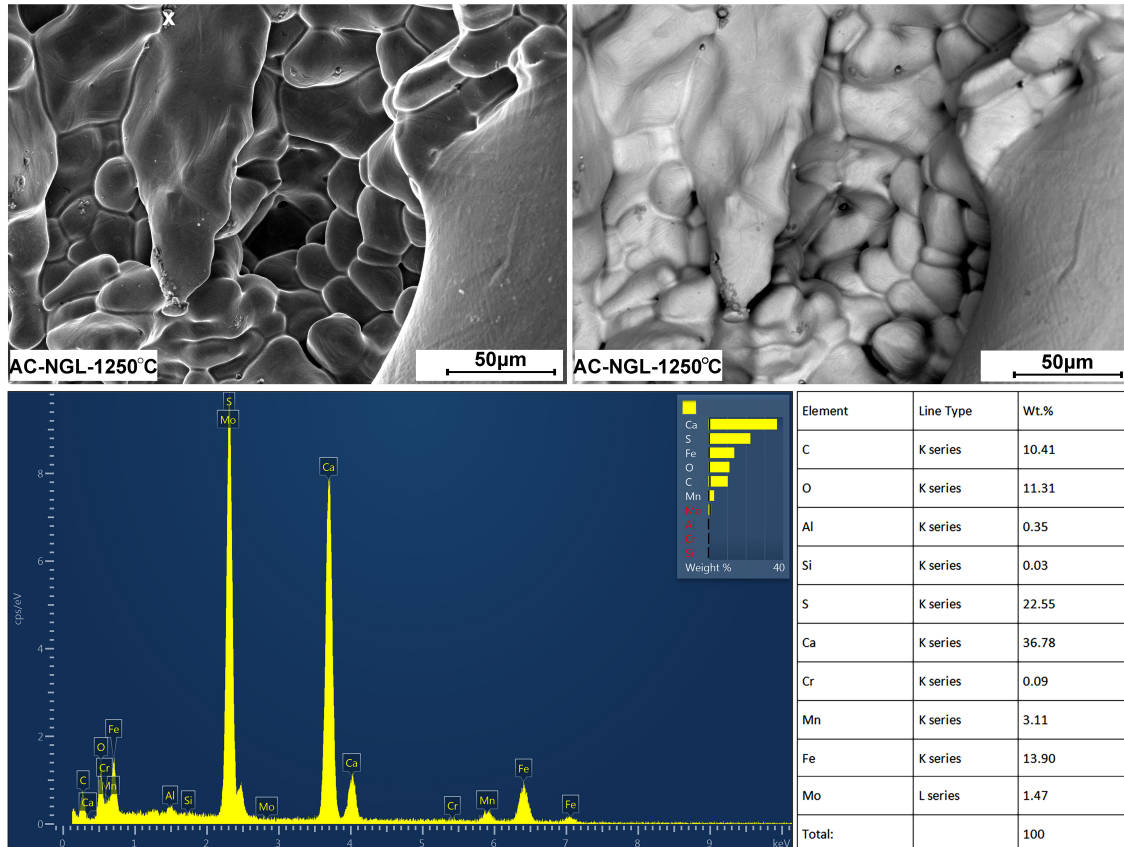


Figure 5.18: Entrapped inclusion and its EDS profile

During steel processing in the ladle, the Ca element is intentionally added to the melt to prevent nozzle clogging during the continuous casting, *i.e.* inclusion agglomeration of brittle MgAl_2O_4 or Al_2O_3 that causes clogging of nozzles and gates [102]. The product is formed as a $[\text{Al}_2\text{O}_3\text{-CaO}]/\text{CaS}$ core/shell inclusion that not only prevents nozzle clogging, but it also ameliorates the fracture and fatigue strength by reducing sulfur content [102]. Regardless of those inclusions *in-situ* formed into the matrix as a product of chemical reaction between alloying elements, if the *ex-situ* precipitates cannot be removed by floating through the slag, they will have deleterious effect on high-temperature mechanical properties due to many reasons. For instance, their non-metallic surface is not able to be wet by the melt during solidification and consequently

the disbonded interface causes air gap formation during shrinkage by solidification and phase transformation. This gap can act as a nucleation site for crack formation and propagation. Also, since these precipitates are stable even at ultra-high temperatures, they act as a barrier against dislocations mobility, causing dislocation piles up and stored stress.

5.5 Summary

To summarize all discussions given in this chapter, the followings could be considered:

(1) The coarse-grain as-cast structure mainly contains ferrite, retained austenite, and pearlite formed in two styles of fine and coarse degenerated, while the transfer-bar one shows fine ferrite and degenerated pearlite pockets. Although the thermally-activated phenomena at intercritical temperature, 1400°C, *i.e.* DRV, DRX, and grain growth retransform the structure in fully austenitic form and make the microstructure and texture almost similar, the presence of porosities in the as-cast samples that are no longer existed in the transfer-bar structure applies changes in the constitutive behaviour of the material.

(2) Regardless of the as-received microstructure, test temperature, and the geometry that are used during the Gleeble testing, all σ -displacement curves show a wavy-shape trend, which is due to the dDRX in the austenite. In other words, this manner is a resultant of competition between hardening and softening mechanisms taken place at high temperature and low strain rates.

(3) The LGL samples shows better reproducibility of the data due to the smooth stress localization along their gauge and the steep thermal gradient that exposes the middle of the gauge to the highest temperature, called hot-spot zone. The synergy between two mentioned factors conducts a condition in which the sample will neck sharply on its middle section followed by an uneven plastic deformation and ultimately failure. Generally, the transfer-bars show higher strength in this geometry, but the high melting vulnerability, particularly at 1450°C, leads to a significant drop in hot ductility.

(4) The SGL samples show the lowest convergence between the data achieved due to a highly triaxial stress localized beneath the sharp shoulder. The unpredictable

thermomechanical behaviour in this condition leads the samples showing a big variation between the high-temperature mechanical characteristics. The NGL geometry, on the other hand, presents very gentle stress localization due to the absence of the gauge, but the other factor comes in to play a role on constitutive behaviour, called the necking mode. Since the thermal gradient in the NGL samples is very shallow, the hot-spot zone cannot take place in a specific zone, and consequently the necking diffuses from one hot zone to another. The diffuse necking mode brings lower repeatability in the data compared with the LGL geometry. The results obtained by the NGL samples show better strength in TB samples, while the ductility in the AC samples gains higher values.

(5) On the effective parameters on high-, and ultra-high temperature mechanical behaviour, some phenomenological like the rate of and physically-based parameters should be taken into account. For instance, the rate of DRV and DRX directly affect the grain boundary sliding and stress relief in triple junctions, while the SFE shrinkage and increase in shear strength due to concentrated interstitial atoms intensifies the hardening rate by means of hindering the dislocations mobility and generating new dislocation sources. Besides from that, the presence of non-metallic inclusions and low melting phases facilitate hot embrittlement based upon void formation and tearing of wet γ grain boundaries at temperatures lower than solidus temperature.

Chapter 6

Conclusions and Future Works

In order to gain a better understanding of the likelihood of hot embrittlement in DP600 AHSSs, thermomechanical Gleeble test was performed on both initial as-cast and transfer-bar structures. The tensile samples were generally heated within a wide range between 1250°C and 1480°C. The results were evaluated via the optical and scanning electron microscopy. The most important findings of the current study are concluded as:

- 1- Identify the suitable geometry for high, and ultra-high temperature mechanical test in which a better reproducibility of constitutive data could be achieved.
- 2- Quantitatively determine the constitutive behaviour of the DP600 AHSSs within 1250 to 1480°C temperature range. This information can be used for process modeling over either solid-state or semi-solid zones.
- 3- Analysis of fractographs in combination of mechanical testing has also revealed the underlined microstructural phenomena such as phase transformation, DRV, DRX, and grain growth as well as microstructural features like grain size, porosity volume fraction, and presence of inclusions that lead to the constitutive behaviour that was observed.

Regarding the results presented in this study, the following suggestions are given to be pursuit in future works:

- 1- Manipulate different thermomechanical schedules in which the critical temperatures and time will vary is helpful to comprehend the effect of various processing parameters like heating and cooling rates, holding time, and strain rate, as well as the portion

of each thermophysically-based phenomena such as the static, metadynamic, and dynamic recrystallizations on the constitutive behaviour of the target alloy.

2- Couple the Gleeble thermomechanical simulation with *in-situ* observation of high-temperature microstructural changes *e.g.* DRV, DRX, subgrain and grain growth, grain boundary sliding, peritectic transformation, and melting via laser scanning confocal microscopy allows to understand the controlling mechanism on hot ductility behaviour at each step of thermomechanical regime.

3- Adopt the presented constitutive models in the literature with the data achieved by the Gleeble testing leads to measure phenomenological constants of the studying material and predicting its constitutive behaviour over a wide range of temperature, strain, and strain rate.

Appendix

How to calculate material constants in the Garofalo constitutive model

Generally, the Arrhenius-type phenomenological equation that shows the relationship between the strain rate, flow stress and temperature is written as [103]:

$$\dot{\epsilon} = AF(\sigma).Exp\left(\frac{-Q}{RT}\right)$$

$$\text{where } \begin{cases} F(\sigma) = \sigma^{n'}; & \text{where } \alpha\sigma < 0.8 \\ F(\sigma) = Exp(\beta\sigma); & \text{where } \alpha\sigma > 1.2 \\ F(\sigma) = [sinh(\alpha_\epsilon\sigma)]^{n_\epsilon}; & \text{for all } \sigma \end{cases} ,$$

where, Q and T are apparent activation energy of hot deformation and the absolute temperature. Deformation behaviour is affected by temperature and strain rate based upon the Zener-Hollmon parameter (Z) presented as:

$$Z = \dot{\epsilon}Exp\left(\frac{Q}{RT}\right) = A[sinh(\alpha\sigma)]^n; \quad \text{where } \alpha = \frac{\beta}{n'}$$

in which, A, α , β , and n' are material constants. Also, the correlation between the flow stress and the Z parameter as well as strain rate are formulated as:

$$\sigma = \frac{1}{\alpha} \ln \left[\left(\frac{Z}{A} \right)^{\frac{1}{n}} + \left[\left(\frac{Z}{A} \right)^{\frac{2}{n}} + 1 \right]^{0.5} \right]$$

$$\begin{cases} \dot{\epsilon} = B\sigma^{n'}; & \text{where } \alpha\sigma < 0.8 \quad (\text{for the low stress level}) \\ \dot{\epsilon} = B'Exp(\beta\sigma); & \text{where } \alpha\sigma > 1.2 \quad (\text{for the high stress level}) \\ \dot{\epsilon} = B''[sinh(\alpha_\epsilon\sigma)]^{n_\epsilon}.Exp\left(\frac{-Q_\epsilon}{RT}\right); & (\text{for all stress values}) \end{cases} ,$$

where, B , B' , and B'' are temperature-independent material constants. To cover both low and high stress levels, the strain rate vs. flow stress equations will intersect each others on a specific point in which:

$$\ln \sigma = -\ln \frac{B}{n'} + \ln \frac{\dot{\epsilon}}{n'} \quad \text{and} \quad \sigma = -\ln \frac{B'}{\beta} + \ln \frac{\dot{\epsilon}}{\beta}$$

Doing experiments on different temperatures and strain rates gives such a result schematically shown in figures below:

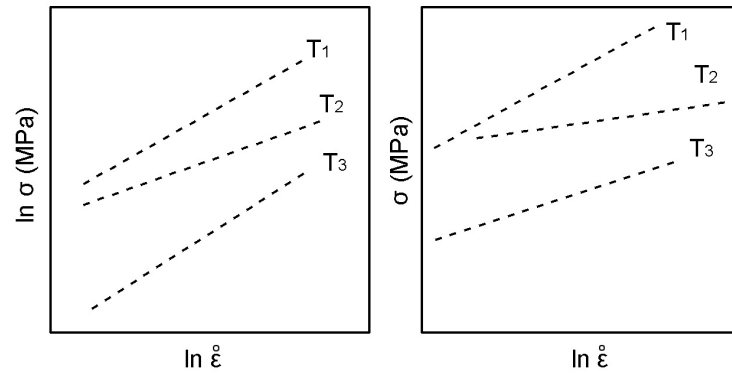


Figure 6.1: Correlation between flow stress and strain rate at various temperatures

Calculating the slope of $\ln \sigma - \ln \dot{\epsilon}$ and $\sigma - \ln \dot{\epsilon}$ gives n' and β values and subsequently, α can be measured. For all stress level, the strain rate equation is rewritten as:

$$Q = R \left[\frac{\partial \ln \dot{\epsilon}}{\partial \ln [\sinh(\alpha_\epsilon \sigma)]} \right]_T \cdot \left[\frac{\partial \ln [\sinh(\alpha_\epsilon \sigma)]}{\partial (\frac{1}{T})} \right]_{\dot{\epsilon}} \quad \text{or} \quad Q = R \cdot m' \cdot m''$$

where, m' and m'' are two terms given in brackets and can be calculated as shown below:

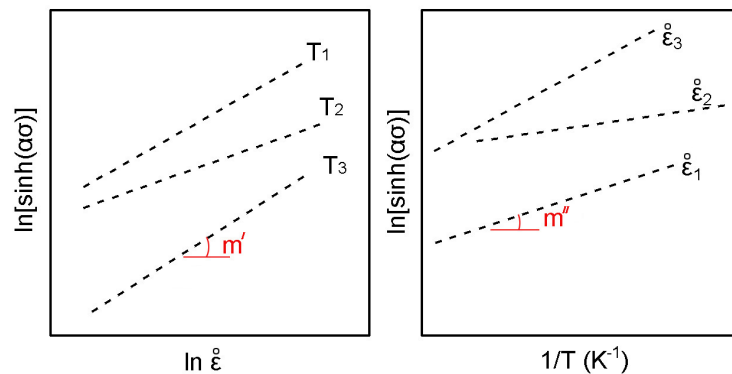


Figure 6.2: Correlation between $\ln[\sinh(\alpha_\epsilon \sigma)]$, $\ln \dot{\epsilon}$, and $\frac{1}{T}$

Therefore, Q can be measured via values obtained for m' and m'' . In next step, the measured Q is inserted into the Zener-Hollomon equation, so Z parameter will be calculated. By plotting the curve below, n and B'' constants are defined as the slope and the intersection of the curve and Y-axis.

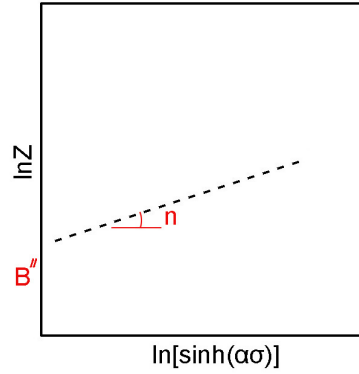


Figure 6.3: Correlation between $\ln[\sinh(\alpha\sigma)]$ and $\ln Z$

Ultimately, solving both equations given below allows to predict the flow stress as well as stress peak of the studying material.

$$\begin{cases} Z = \dot{\epsilon} \exp\left(\frac{Q}{RT}\right) \\ \sigma = \frac{1}{\alpha} \ln \left[\left(\frac{Z}{A}\right)^{\frac{1}{n}} + \left[\left(\frac{Z}{A}\right)^{\frac{2}{n}} + 1\right]^{0.5} \right] \end{cases}$$

Bibliography

- [1] N. Fonstein, *Advanced high strength sheet steels: Physical metallurgy, design, processing, and properties*. Springer International Publishing, Switzerland, 2015.
- [2] S. Chen, R. Rana, A. Haldar, R.K. Ray, *Current state of Fe-Mn-Al-C low density steels*. Progress in Materials Science, 89, 2017, 345-91.
- [3] M.Y. Demeri, *Advanced high strength steels: Science, technology, and applications*. ASM International, USA, 2013.
- [4] D.K. Matlock, J.G. Speer, E. De Moor, P.J. Gibbs, *Recent developments in advanced high strength sheet steels for automotive applications: An overview*. JESTECH, 15, 2012, 1-12.
- [5] R. Kuziak, R. Kawalla, S. Waengler, *Advanced high strength steels for automotive industry*. Archives of Civil and Mechanical Engineering, 8, 2008, 103-17.
- [6] J. Zhao, Z. Jiang, *Rolling of advanced high strength steels: Theory, simulation and practice*. Taylor & Francis Group, USA, 2017.
- [7] J.G. Speer, D.K. Matlock, B.C. De Cooman, J.G. Schroth, *Carbon partitioning into austenite after martensite transformation*. Acta Materialia, 51, 2003, 2611-22.
- [8] L. Schemmann, S. Zaefferer, D. Raabe, F. Friedel, D. Mattissen, *Alloying effects on microstructure formation of dual phase steels*. Acta Materialia, 95, 2015, 386-98.
- [9] O. Bouaziz, H. Zurob, M. Huang, *Driving force and logic of development of advanced high strength steels for automotive applications*. Steel Research International, 84, 2013, 937-47.

- [10] D.A. Korzekwa, D.K. Matlock, G. Krauss, *Dislocation substructure as a function of strain in a dual-phase steel*, Metallurgical and Materials Transactions A, 15, 1984, 1221-8.
- [11] M. Calcagnotto, D. Ponge, E. Demir, D. Raabe, *Orientation gradients and geometrically necessary dislocations in ultrafine grained dual-phase steels studied by 2D and 3D EBSD*. Materials Science and Engineering: A, 527, 2010, 2738-46.
- [12] A. Ramazani, K. Mukherjee, A. Schwedt, P. Goravanchi, U. Prahl, W. Bleck, *Quantification of the effect of transformation-induced geometrically necessary dislocations on the flow-curve modeling of dual-phase steels*. International Journal of Plasticity, 43, 2013, 128-52.
- [13] H. Ghassemi-Armaki, R. Maaß, S.P. Bhat, S. Sriram, J.R. Greer, K.S. Kumar, *Deformation response of ferrite and martensite in a dual-phase steel*. Acta Materialia, 62, 2014, 197-211.
- [14] R.G. Davies, *Influence of martensite composition and content on the properties of dual phase steels*. Metallurgical Transactions A, 9, 1978, 671-9.
- [15] H.P. Shen, T.C. Lei, J.Z. Liu, *Microscopic deformation behaviour of martensitic-ferritic dual-phase steels*. Materials Science and Technology, 2, 1986, 28-33.
- [16] A.M. Sarosiek, W.S. Owen, *The work hardening of dual-phase steels at small plastic strains*. Materials Science and Engineering, 66, 1984, 13-34.
- [17] Z. Jiang, J. Liu, J. Lian, *A new relationship between the flow stress and the microstructural parameters for dual phase steel*. Acta Metallurgica et Materialia, 40, 1992, 1587-97.
- [18] D. Das, P.P. Chattopadhyay, *Influence of martensite morphology on the work-hardening behavior of high strength ferrite-martensite dual-phase steel*. Journal of Materials Science, 44, 2009, 2957-65.
- [19] R.A. Kot, J.W. Morris, *Structure and properties of dual-phase steels*. TMS/AIME, USA, 1979.

- [20] R.A. Kot, B.L. Bramfitt, *Fundamentals of dual-phase steels*. TMS/AIME, USA, 1981.
- [21] J.S. Gau, G. Thomas, *Metallurgy of continuous-annealed sheet steels*. TMS/AIME, USA, 1982.
- [22] W.R. Irving, *Continuous casting of steel*. The Cambridge University Press, UK, 1993.
- [23] J. Jang, J. Guo, C. Chang, *The heat transfer analysis of an acting-type heat retention panel used in a hot rolling process*. Applied Sciences, 9, 2019, 189-206.
- [24] B.G. Thomas, *Modeling of the continuous casting of steel—past, present, and future*. Metallurgical and Materials Transactions B, 33, 2002, 795-812.
- [25] J.G. Lenard, *Primer on flat rolling*. Elsevier, UK, 2014.
- [26] B. Mintz, S. Yue, J.J. Jonas, *Hot ductility of steels and its relationship to the problem of transverse cracking during continuous casting*. International Materials Reviews, 36, 1991, 187-220.
- [27] G.A. Wilber, R. Batra, W.F. Savage, W.J. Childs, *The effects of thermal history and composition on the hot ductility of low carbon steels*. Metallurgical Transactions A, 6, 1975, 1727-35.
- [28] H.G. Suzuki, S. Nishimura, J. Imamura, Y. Nakamura, *Embrittlement of steels occurring in the temperature range from 1000 to 600C*. Transactions of the Iron and Steel Institute of Japan, 24, 1984, 169-77.
- [29] B. Mintz, A. Tuling, A. Delgado, *Influence of silicon, aluminium, phosphorus and boron on hot ductility of transformation Induced Plasticity assisted steels*. Materials Science and Technology, 19, 2003, 1721-6.
- [30] G.I.S.L. Cardoso, B. Mintz, S. Yue, *Hot ductility of aluminium and titanium containing steels with and without cyclic temperature oscillations*. Ironmaking and Steelmaking, 22, 1995, 365-77.

- [31] B. Mintz, D.N. Crowther, *Hot ductility of steels and its relationship to the problem of transverse cracking in continuous casting*. International Materials Reviews, 55, 2010, 168-96.
- [32] B. Mintz, *The influence of composition on the hot ductility of steels and to the problem of transverse cracking*. ISIJ International, 39, 1999, 833-55.
- [33] D.N. Crowther, Z. Mohamed, B. Mintz, *The relative influence of dynamic and static precipitation on the hot ductility of microalloyed steels*. Metallurgical Transactions A, 18, 1987, 1929-39.
- [34] S. Harada, S. Tanaka, H. Misumi, S. Mizoguchi, H. Horiguchi, *A formation mechanism of transverse cracks on CC slab surface*. ISIJ International, 30, 1990, 310-6.
- [35] B. Mintz, J.M. Arrowsmith, *Hot-ductility behaviour of C-Mn-Nb-Al Steels and its relationship to crack Propagation during the straightening of continuously cast strand*. Materials Technology, 6, 1979, 24-32.
- [36] H.G. Suzuki, S. Nishimura, Y. Nakamura, *Improvement of hot ductility of continuously cast carbon steels*. Trans ISIJ, 24, 1984, 54-9.
- [37] K.A. Bywater, T. Gladman, *Influence of composition and microstructure on hot workability of austenitic stainless steels*. Metals Technology, 3, 1976, 358-65.
- [38] H.E. Evans, *The mechanism of void growth and factors affecting the onset of intergranular failure during creep of a magnesium-0.8 percent aluminium alloy*. Metal Science Journal, 3, 1969, 33-8.
- [39] J.H. Reynold, T. Gladman, *Hot cracking of low-alloy steels*. Hot Working and Forming Processes Conference, UK, 1979, 171-5.
- [40] V. Kutumba Rao, D.M.R. Taplin, P. Rama Rao, *The grain size dependence of flow and fracture in a Cr-Mn-N austenitic steel from 300 to 1300K*. Metallurgical Transactions A, 6, 1975, 77-86.
- [41] R. Abushosha, S. Ayyad, B. Mintz, *Influence of cooling rate and MnS inclusions on hot ductility of steels*. Materials Science and Technology, 14, 1998, 227-35.

- [42] R. Abushosha, S. Ayyad, B. Mintz, *Influence of cooling rate on hot ductility of C-Mn-Al and C-Mn-Nb-Al steels*. Materials Science and Technology, 14, 1998, 346-51.
- [43] B.G. Thomas, J.K. Brimacombe, I.V. Samarasekera, *The Formation of panel cracks in steel ingots: A state-of-the-art review*. ISS transactions, 7, 1986, 7-20.
- [44] Y.C. Lin, X. Chen, *A critical review of experimental results and constitutive descriptions for metals and alloys in hot working*. Materials and Design, 32, 2011, 1733-59.
- [45] J.H. Sung, J.H. Kim, R.H. Wagoner, *A plastic constitutive equation incorporating strain, strain-rate, and temperature*. International Journal of Plasticity, 26, 2010, 1746-71.
- [46] G.R. Johnson, W.H. Cook, *A constitutive model and data for metals subjected to large strains, high strain rates and high temperatures*. Proceedings of the 7th International Symposium on Ballistics, Netherlands, 1983, 541-3.
- [47] A.S. Khan, S. Huang, *Experimental and theoretical study of mechanical behavior of 1100 aluminum in the strain rate range 10^5 - 10^4 s⁻¹*. International Journal of Plasticity, 8, 1992, 397-424.
- [48] C. Zener, H. Hollomon, *Effect of strain rate upon plastic flow of steel*. Journal of Applied physics, 15, 1944, 22-32.
- [49] J.J. Jonas, C.M. Sellars, W.J.M.G. Tegart, *Strength and structure under hot-working conditions*. Metallurgical Reviews, 14, 1969, 1-24.
- [50] Y.C. Lin, F. Nong, X. Chen, D. Chen, M. Chen, *Microstructural evolution and constitutive models to predict hot deformation behaviors of a nickel-based superalloy*. Vacuum, 137, 2017, 104-14.
- [51] H.J. Zhang, W.D. Wen, H.T. Cui, *Behaviors of IC10 alloy over a wide range of strain rates and temperatures: Experiments and modeling steel*. Materials Science and Engineering A, 504, 2009, 99-103.

- [52] M. Vural, J. Caro, *Experimental analysis and constitutive modeling for the newly developed 2139-T8 alloy*. Materials Science and Engineering A, 520, 2009, 56-65.
- [53] A.S. Khan, H.Y. Zhang, L. Takacs, *Mechanical response and modeling of fully compacted nanocrystalline iron and copper*. International Journal of Plasticity, 16, 2000, 1459-76.
- [54] A.S. Khan, R. Liang, *Behaviors of three BCC metal over a wide range of strain rates and temperatures: Experiments and modeling*. International Journal of Plasticity, 15, 1999, 1089-109.
- [55] A.S. Khan, Y.S. Suh, R. Kazmi, *Quasi-static and dynamic loading responses and constitutive modeling of titanium alloys*. International Journal of Plasticity, 20, 2004, 2233-48.
- [56] M. Naderi, L. Durrenberger, A. Molinari, W. Bleck, *Constitutive relationships for 22MnB5 boron steel deformed isothermally at high temperatures*. Materials Science and Engineering A, 478, 2008, 130-9.
- [57] E. Voce, *The relationship between stress and strain for homogeneous deformation*. Journal of the Institute Metals, 74, 1948, 537-62.
- [58] J.H. Hollomon, *Tensile deformation*. Transactions of AIME, 162, 1945, 268-90.
- [59] A. Rusinek, J.R. Klepaczko, *Shear testing of a sheet steel at wide range of strain rates and a constitutive relation with strain-rate and temperature dependence of the flow stress*. International Journal of Plasticity, 17, 2001, 87-115.
- [60] A. Seeger, *The mechanism of glide and work-hardening in face-centered cubic and hexagonal close-packed metal*. Dislocations and Mechanical Properties of Crystals, John Wiley and Sons, USA, 1957, 243-329.
- [61] J.R. Klepaczko, *Thermally activated flow and strain rate history effects for some polycrystalline FCC metals*. Materials Science and Engineering, 18, 1975, 121-35.
- [62] J.R. Klepaczko, *A general approach to rate sensitivity and constitutive modeling of FCC and BCC metals*. Impact: Effects of Fast Transient Loadings, Netherlands, 1998, 3-35.

- [63] J.R. Klepaczko, *A practical stress-strain-strain rate-temperature constitutive relation of the power form*. Journal of Mechanical Working Technology, 15, 1987, 143-65.
- [64] J.R. Klepaczko, J.A. Rodriguez-Martinez, *Thermo-viscoplastic constitutive relation for aluminium alloys, modeling of negative strain rate sensitivity and viscous drag effects*. Materials and Design, 30, 2009, 4377-90.
- [65] P.J. Zerilli, R.W. Armstrong, *Dislocation-mechanics-based constitutive relations for material dynamics calculations*. Journal of applied physics, 61, 1987, 1816-25.
- [66] G.Z. Voyiadjis, A.H. Almasri, *A physically based constitutive model for fcc metals with applications to dynamic hardness*. Mechanics of Materials, 40, 2008, 549-63.
- [67] H.J. Zhang, W.D. Wen, H.T. Cui, Y. Xu, *A modified Zerilli-Armstrong model for alloy IC10 over a wide range of temperatures and strain rates*. Materials Science and Engineering A, 526, 2009, 1-6.
- [68] H. Yu, Y. Guo, X. Lai, *Rate-dependent behavior and constitutive model of DP600 steel at strain rate from 10^4 to 10^3 s⁻¹*. Materials and Design, 30, 2009, 2501-5.
- [69] R.H. Wagoner, *A technique for measuring strain-rate sensitivity*. Metallurgical Transactions, 12, 1981, 71-5.
- [70] F. Garofalo, *Fundamentals of creep and creep-rupture in metals*. Macmillan, USA, 1965.
- [71] H.N. Han, Y. Lee, K.H. Oh, D.N. Lee, *Analysis of hot forging of porous metals*. Materials Science and Engineering A, 206, 1995, 81-9.
- [72] H.J. McQueen, N.D. Ryan, *Constitutive analysis in hot working*. Materials Science and Engineering A, 322, 2002, 43-63.
- [73] C. Erel, G. Po, N. Ghoniem, *Dependence of hardening and saturation stress in persistent slip bands on strain amplitude during cyclic fatigue loading*. Philosophical Magazine, 97, 2017, 2947-70.

- [74] C. Capdevila, F.G. Caballero, C. Garcia de Andres, *Modeling of kinetics of austenite-to-allotriomorphic ferrite transformation in 0.37C-1.45Mn-0.11V microalloyed steel*. Metallurgical and Materials Transactions A, 32, 2001, 661-9.
- [75] M. Thompson, M. Ferry, P.A. Manohar, *Simulation of hot-band microstructure of C-Mn steels during high speed cooling*. ISIJ International, 41, 2001, 891-9.
- [76] S. Shanmugam, N.K. Ramiseti, R.D.K. Misra, T. Mannering, D. Panda, S. Jansto, *Effect of cooling rate on the microstructure and mechanical properties of Nb-microalloyed steels*. Materials Science and Engineering A, 460-461, 2007, 335-43.
- [77] A. Iza-Mendia, I. Gutierrez, *Generalization of the existing relations between microstructure and yield stress from ferrite-pearlite to high strength steels*. Materials Science and Engineering A, 561, 2013, 40-51.
- [78] K.I. Sugimoto, N. Usui, M. Kobayashi, S.I. Hashimoto, *Effect of volume fraction and stability of retained austenite on ductility of TRIP-aided dual-phase steels*. ISIJ International, 32, 1992, 1311-8.
- [79] I.B. Timokhina, P.D. Hodgson, E.V. Pereloma, *Effect of microstructure on the stability of retained austenite in transformation-induced-plasticity steels*. Metallurgical and Materials Transactions A, 35, 2004, 2331-41.
- [80] A.M. Elwazri, E. Essadiqi, S. Yue, *Kinetics of metadynamic recrystallization in microalloyed hypereutectoid steels*. ISIJ International, 44, 2004, 744-52.
- [81] W.P. Sun, E.B. Hawbolt, *Comparison between static and metadynamic recrystallization - An application to the hot rolling of steels*. ISIJ International, 37, 1997, 1000-9.
- [82] M. Sarwar, E. Ahmad, K.A. Qureshi, T. Manzoor, *Influence of epitaxial ferrite on tensile properties of dual phase steel*. Materials and Design, 28, 2007, 335-40.
- [83] X. Guo, D. M. Stefanescu, *Partitioning of alloying elements during the eutectoid transformation of ductile iron*. International Journal of Cast Metals Research, 11, 1999, 437-41.

- [84] S.E. Offerman, N.H. van Dijk, J. Sietsma, E.M. Lauridsen, L. Margulies, S. Grigull, H.F. Poulsen, S. van der Zwaag, *Solid-state phase transformations involving solute partitioning: Modeling and measuring on the level of individual grains*. Acta Materialia, 52, 2004, 4757-66.
- [85] G. Krauss, *Steels: Processing, structure, and performance*. ASM International, USA, 2005.
- [86] T. Sakai, A. Belyakov, R. Kaibyshev, H. Miura, J.J. Jonas, *Dynamic and post-dynamic recrystallization under hot, cold and severe plastic deformation conditions*. Progress in Materials Science, 60, 2014, 130-207.
- [87] T. Sakai, J.J. Jonas, *Dynamic recrystallization: Mechanical and microstructural considerations*. Acta Metallurgica et Materialia, 32, 1984, 189-209.
- [88] H.J. McQueen, J.J. Jonas, *Recovery and recrystallization during high temperature deformation*. Treatise on Materials Science and Technology, 6, 1975, 393-493.
- [89] K. Huang, R.E. Logé, *A review of dynamic recrystallization phenomena in metallic materials*. Materials and Design, 111, 2016, 548-74.
- [90] F. Fujie, S. Harada, H. Koizumi, K. Murayama, K. Hanada, M. Tagawa, T. Uji-hara, *Direct observation of stacking fault shrinkage in 4H-SiC at high temperatures by in-situ X-ray topography using monochromatic synchrotron radiation*. Applied Physics Letters, 113, 2018, 012101-4.
- [91] J. Fernández, S. Illescas, J.M. Guilemany, *Effect of microalloying elements on the austenitic grain growth in a low carbon HSLA steel*. Materials Letters, 61, 2007, 2389-92.
- [92] A.I. Fernández, P. Uranga, B. López, J.M. Rodríguez-Ibabe, *Dynamic recrystallization behavior covering a wide austenite grain size range in Nb and Nb-Ti microalloyed steels*. Materials Science and Engineering A, 361, 2003, 367-76.
- [93] A.A. Benzerga, J.B. Leblond, *Advances in Applied Mechanics: Ductile fracture by void growth to coalescence*. Elsevier, Netherlands, 2010, 169-305.

- [94] A. Pineau, A.A. Benzerga, T. Pardoen, *Failure of metals I: Brittle and ductile fracture*. Acta Materialia, 107, 2016, 424-83.
- [95] A. Melander, K.O. Husby, *Influence of the strain rate sensitivity on diffuse necking in tensile tests*. Materials Science and Engineering, 46, 1980, 103-12.
- [96] T.M. Jeng, S.C. Tzeng, *Numerical study of confined slot jet impinging on porous metallic foam heat sink*. International Journal of Heat and Mass Transfer, 48, 2005, 4685-94.
- [97] J. Martínez Lucci, R.S. Amano, P.K. Rohatgi, *Heat transfer and fluid flow analysis of self-healing in metallic materials*. Heat Mass Transfer, 53, 2017, 825-48.
- [98] R.J. Dippenaar, D.J. Phelan, *Delta-ferrite recovery structures in low-carbon steels*. Metallurgical and Materials Transactions B, 34, 2003, 495-501.
- [99] D. Lassance, F. Scheyvaerts, T. Pardoen, *Growth and coalescence of penny-shaped voids in metallic alloys*. Engineering Fracture Mechanics, 73, 2006, 1009-34.
- [100] M.E. Kassner, *Fundamentals of creep in metals and alloys*. Butterworth-Heinemann, USA, 2015.
- [101] A. Ghosh, *Segregation in cast products*. Sadhana, 26, 2001, 5-24.
- [102] Y. Wang, M. Valdez, S. Sridhar, *Formation of CaS on Al₂O₃-CaO inclusions during solidification of steels*. Metallurgical and Materials Transactions B, 33, 2002, 625-32.
- [103] M. Zhou, Y.C. Lin, J. Deng, Y.Q. Jiang, *Hot tensile deformation behaviors and constitutive model of an Al-Zn-Mg-Cu alloy*. Materials and Design, 59, 2014, 141-50.